UC Berkeley
UC Berkeley Electronic Theses and Dissertations

Title
Design, Fabrication, and Testing of the INSTAR [INertial STorage And Recovery] System: A Flywheel-based, High Power Energy Storage System for Improved Hybrid Vehicle Fuel Efficiency

Permalink
https://escholarship.org/uc/item/328239cw

Author
Talancon, Daniel Raul

Publication Date
2015

Supplemental Material
https://escholarship.org/uc/item/328239cw#supplemental

Peer reviewed|Thesis/dissertation

eScholarship.org Powered by the California Digital Library
University of California

Design, Fabrication, and Testing of the INSTAR [INertial STorage And Recovery] System

A Flywheel-Based, High Power Energy Storage System

for Improved Hybrid Vehicle Fuel Efficiency

By

Daniel Raul Talancon

A dissertation submitted in partial satisfaction of the

requirements for the degree of

Doctor of Philosophy

in

Engineering – Mechanical Engineering

in the

Graduate Division

of the

University of California, Berkeley

Committee in charge:

Professor Dennis K. Lieu, Chair

Professor Benson H. Tongue

Professor Seth R. Sanders

Spring 2015

Design, Fabrication, and Testing of the INSTAR [INertial STorage And Recovery] System

A Flywheel-Based, High Power Energy Storage System

for Improved Hybrid Vehicle Fuel Efficiency

Copyright 2015

by

Daniel Raul Talancon

Abstract

Design, Fabrication, and Testing of the INSTAR [INertial STorage And Recovery] System

A Flywheel-Based, High Power Energy Storage System

for Improved Hybrid Vehicle Fuel Efficiency

by

Daniel Raul Talancon

Doctor of Philosophy in Mechanical Engineering

University of California, Berkeley

Professor Dennis K. Lieu, Chair

This thesis describes the development of the INSTAR system: a high-power, cost-effective energy storage system designed to improve HEV regenerative braking capabilities by combining chemical batteries with an electromechanical flywheel. This combination allows the regenerative braking system in hybrid vehicles to recapture more available braking energy at a lower battery pack charging current, increasing vehicle energy efficiency while also potentially increasing battery life.

A prototype flywheel energy storage system and electric vehicle test platform were built to test the design. A novel open loop controller was developed to manage the power flow between the traction motors, battery pack, and flywheel energy storage system. The flywheel was designed to hold 30 Wh at 25,000 RPM, but can easily scale to larger vehicles. Experiments were conducted for speeds up to 11,000 RPM and power levels up to 2.5 kW. Round trip efficiency of 70% for the flywheel energy storage system alone were achieved and battery charging current was successfully limited during regenerative braking by absorbing energy with the flywheel energy system. The flywheel energy storage system successfully returned the stored energy, minus parasitic losses, back to the battery pack at controlled rates.

For my parents for all their love and support

and to the very many who have supported my entire academic journey.

Let this merely be the beginning of my career giving back.

Contents

List of Figures

List of Tables

Chapter I. Introduction

This thesis describes the design, prototyping, and testing of the INSTAR [Inertial Storage and Recovery] System, a hybrid chemical battery and electromechanical flywheel energy storage system for improved hybrid vehicle energy efficiency. It is the result of work started in 2009 in the mechanical engineering department at the University of California, Berkeley in Berkeley, California. The Berkeley Energy and Climate Institute provided financial support.

Section 1.01 Background

Advances in energy storage technologies have historically driven some of the major shifts in the automobile industry. Indeed, innovative energy storage technologies can be thought of as *the* critical factor in the success and evolution of personal transportation. Early steam-powered vehicles, which stored their energy in the form of coal or wood, were proven to be a viable technology as early as the 18th century. However, this early version of the automobile was hampered by both its extreme weight and unreliability due to the need to keep a fire burning to boil steam in a metallic boiler. It was not until the invention of the internal combustion engine, with its ability to make use of the much more energy dense liquid petroleum-based fuels. These fuels, which were becoming more available and more affordable due to advances in oil drilling technology, allowed the automobile to become the pillar of modern society that it is today.

The popularity of the automobile, however, has come with a cost. A 2011 report on reducing greenhouse gas emissions from U.S. transportation states it bluntly in its executive summary [1] with data supported by the US Environmental Protection Agency [2]:

> *This report examines the prospects for substantially reducing the greenhouse gas (GHG) emissions from the U.S. transportation sector, which accounts for 27 percent of the GHG emissions of the entire U.S. economy and 30 percent of the world's transportation GHG emissions. Without shifts in existing policies, the U.S. transportation sector's GHG emissions are expected to grow by about 10 percent by 2035, and will still account for a quarter of global transportation emissions at that time. If there is to be any hope that damages from climate change can be held to moderate levels, these trends must change.*

In the past two decades hybrid vehicles have grown in popularity, driven by the growing concern over vehicular carbon emissions, the finite nature of fossil fuels, and the increasing cost savings from these more fuel-efficient vehicles. However, the adoption of these fuel efficient and lower emission vehicles has been hampered by the higher upfront costs associated with their dual-drive train system architectures. As the International Energy Agency puts it in their 2012 report on CO_2 emissions [3]:

> *Although hybrid electric drive trains have made a strong early showing in the Japanese and US markets, their ultimate degree of market penetration will depend strongly on further cost reductions.*

The INSTAR system is designed specifically to further increase hybrid vehicle fuel efficiency, in a cost-effective manner, in hopes that more drivers will shift to this form of lower emission transportation.

Section 1.02 Thesis Overview

The remainder of this work focuses on the design, manufacturing, and testing of the INSTAR system. This proof of concept design is intended to demonstrate the potential for a hybrid energy storage system that combines lithium-ion battery packs with an electromechanical flywheel to improve overall hybrid vehicle system efficiency by improving on existing regenerative braking methods. This is accomplished by using the high power flywheel energy storage portion of the system to absorb a fraction of the energy during regenerative braking and limiting the charge current to the battery pack. Despite lower charging currents, which are better for long term battery health, more energy can be recaptured during braking. The energy stored in the flywheel can be released gradually either to recharge the battery pack at a lower, controlled rate, or released quickly to re-accelerate the vehicle through the traction motors. This power management scheme significantly alters the mechanical design goals of the flywheel system, allowing for the use of conventional materials and components that reduce the cost of implementation. These cost-effective materials, combined with the inherently small weight and volume of the flywheel energy storage system for this scale of energy storage, provides an attractive overall system that has the potential for implementation on road vehicles.

Chapter 2 discusses some of the findings on lithium-ion batteries and the limitations on their use that motivate this design along with other relevant work designing high power energy storage systems for vehicles.

Chapter 3 focuses on the design of the INSTAR prototype, along with the electric test vehicle that was designed and built in order to test the INSTAR system both in and outside of the laboratory.

Chapter 4 discusses the testing of the flywheel energy storage system portion of the INSTAR system. This includes parasitic drag losses and round trip efficiency testing.

Chapter 5 covers the testing of the full INSTAR system, with emphasis on the power flow controller that is at the heart of the system. This controller drives many of the mechanical design aspects and provides many of the innovative contributions of this work.

Chapter II. Literature Review

Section 2.01 Vehicular Energy Storage Systems

The modern hybrid vehicle is a combination of an internal combustion engine (ICE) and a chemical battery pack, either NiMH or Li-Ion. The battery pack is used primarily for two reasons:

1. More efficient engine operation through electric motor assist
2. Regenerative braking through the electric motor to recapture braking energy

While the first point has led to a vast improvement in overall fuel efficiency for many passenger cars, the second point has not yet been taking full advantage of due to the inability of the battery pack to absorb current at charge rates the vehicle is capable of generating during these braking events [4].

Battery capacity, the amount of useful energy the pack can store and deliver, degrades over time. There are many factors that influence how quickly the capacity fades, but one of the largest is the charge rate [5] [6] (see Figure II-1) and the other is the cell temperature [7], which is often driven by high charge rates [8].

Figure II-1 Charge Rate vs Capacity for a Lithium-Ion 18650 Cell from [5]

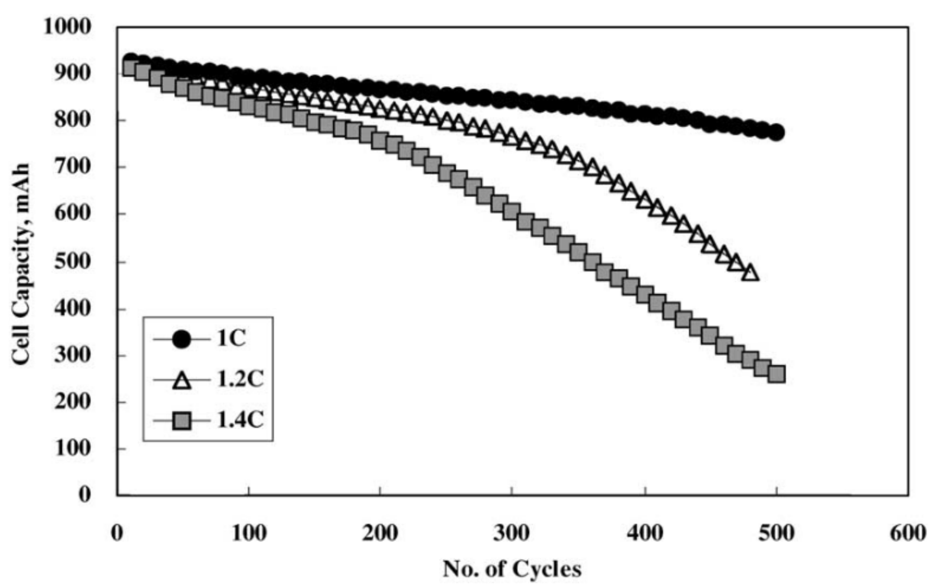

During regenerative braking, hybrid vehicles can generate enough current to charge the batteries at 10C and many vehicles are hardwired to limit the regenerative braking in order to keep the charging level below 4.5C (28A on a 6.5 Ah battery pack) [8]. This is both for thermal reasons and for charge rate-based capacity fade, but the point remains that there is a trade-off between the life of the battery and the charge rate of the battery. Much has been said about the energy density [Wh/kg] of modern chemical batteries, but just as important is the *power* density [W/kg] of these batteries, especially when it comes to regenerative braking.

Figure II-2 Current Hybrid Vehicle Battery Use from [8]

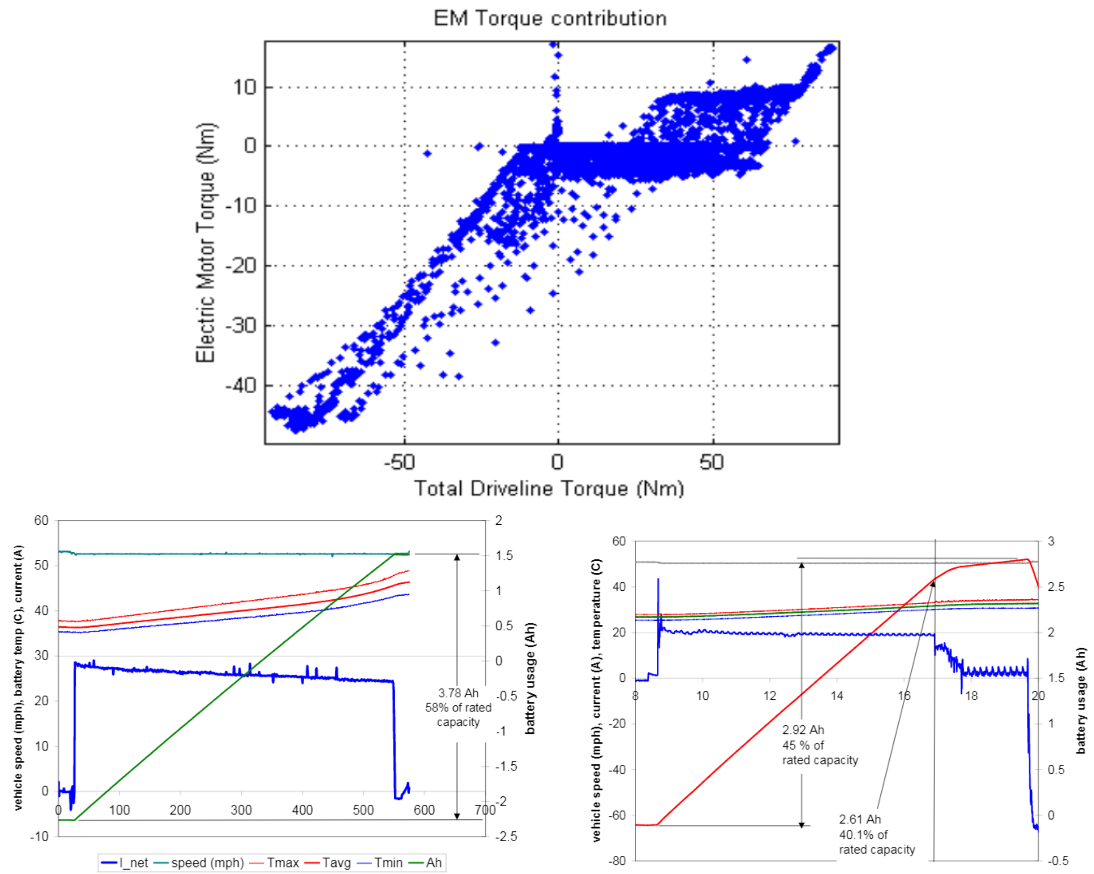

Many higher power energy storage systems do exist and many have been tested for use in vehicles. Figure II-3 compares a wide range of possible energy storage technologies [9]. The two most promising technologies include flywheels and supercapacitors, although hydraulic systems have also been successfully implemented. These will each be discussed below.

The results of the design of the INSTAR prototype are also included for comparison. The rationale for its lower position on both energy density and power density can be potentially attributed to its status as a proof-of-concept design tailored specifically for maintenance and analysis, but also its intentional design as a low cost system. This will be the subject of the rest of this dissertation.

Figure II-3 Comparison of Energy Storage Technologies from [9]

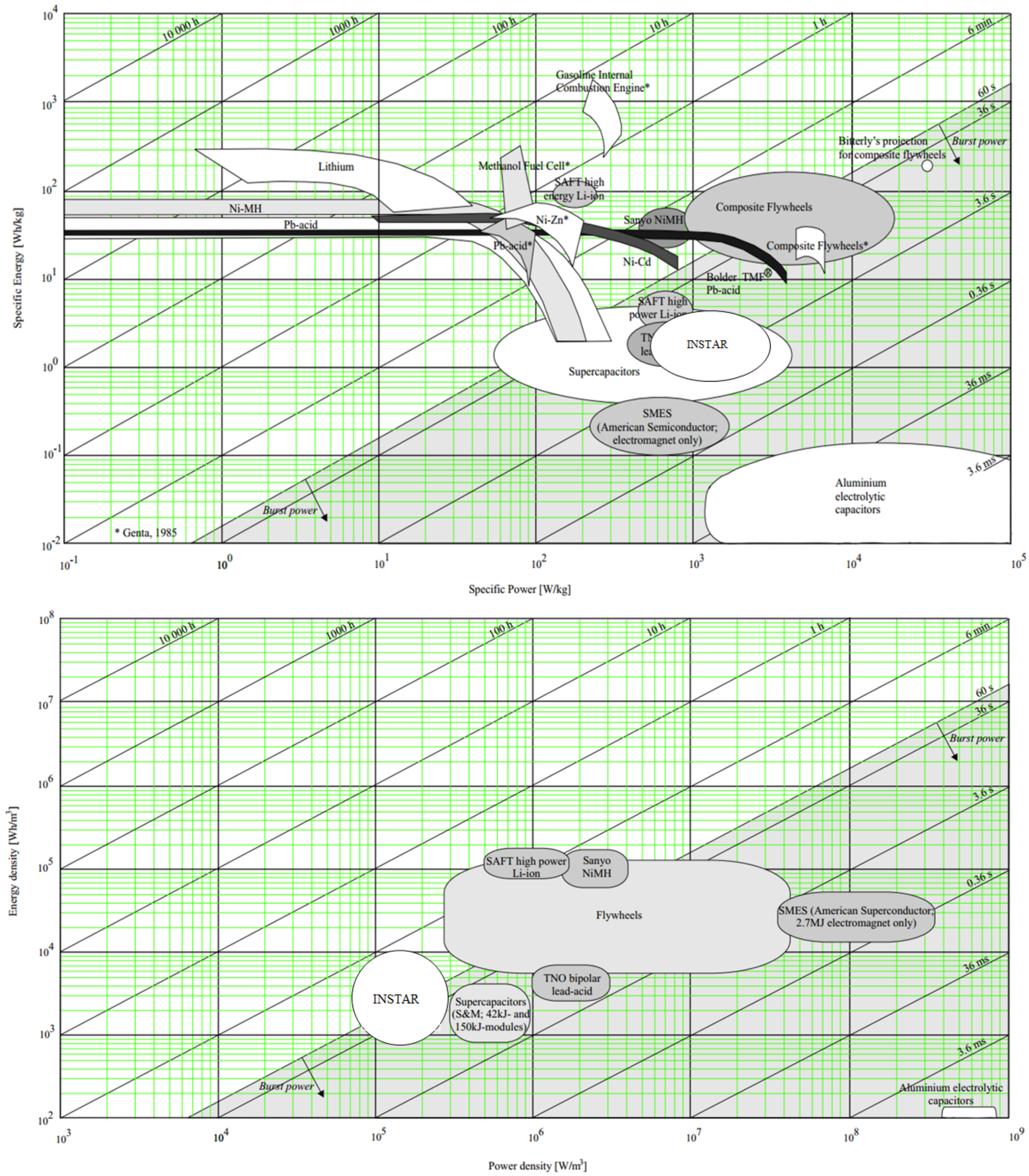

Section 2.02 Vehicular Flywheel Energy Storage Systems

Flywheels have been used in machine designs for centuries - ranging from medieval potters wheels to Watt's famous steam engine. Flywheel use for vehicular applications, while a more modern application of this timeless machine component, has also been under investigation since the 1970s.

The earliest implementations of vehicular flywheels were all mechanical in nature [10]. In the 1970's "Gyrobus" concept the ICE is only used to spin up the mechanical flywheel through a continuously variable transmission (CVT) below 35 mph [15 m/s], operating at peak efficiency speed until the flywheel reaches its maximum operating speed. The flywheel is then used to propel the vehicle and recapture braking energy. According to Kok [11], the regenerative braking capability was only marginally beneficial and most of the 35% fuel efficiency improvements are provided by the higher efficiency operation of the ICE.

Figure II-4 Early Vehicular Flywheel Energy Storage in a Transit Bus

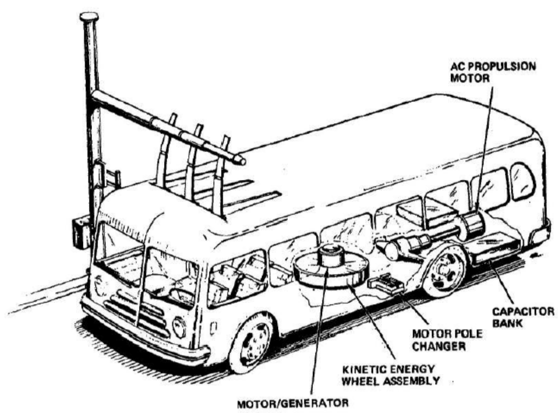

This type of mechanical flywheel hybrid vehicle concept has since been vastly improved upon by a UK-based company developing the "Flybrid" system. This performance-minded mechanical flywheel also uses a CVT, but now is capable of rotating at speeds over 60,000 RPM using a carbon fiber rim to withstand the extreme hoop stress this system subjects itself to. The Flybrid system has successfully been used in Formula 1, serving as a Kinetic Energy Recovery System (KERS) to provide surge acceleration power with the stored braking energy it captures [12]. It is also being tested in a production vehicle in cooperation with Jaguar [12].

Figure II-5 Flybrid Flywheel

Other researchers have also continued to focus on improving the fuel efficiency of buses. These large vehicles with high braking frequency continue to be an attractive application of flywheel energy storage systems as the power required to stop a bus is quite high, far higher than a battery is capable of handling [12]. These systems can either be purely mechanical in nature like the Ricardo Flybus [12], or electromechanical as in the UT Austin flywheel bus [13]. They can use ball bearings [13], magnetic bearings the case in the L-3 Communications Magnet Motor flywheel system installed in a dozen Swiss buses [12], or even magnetic couplings as in the Ricardo Flybus.

Figure II-6 Examples of Modern Transit Bus Flywheel Energy Storage Systems

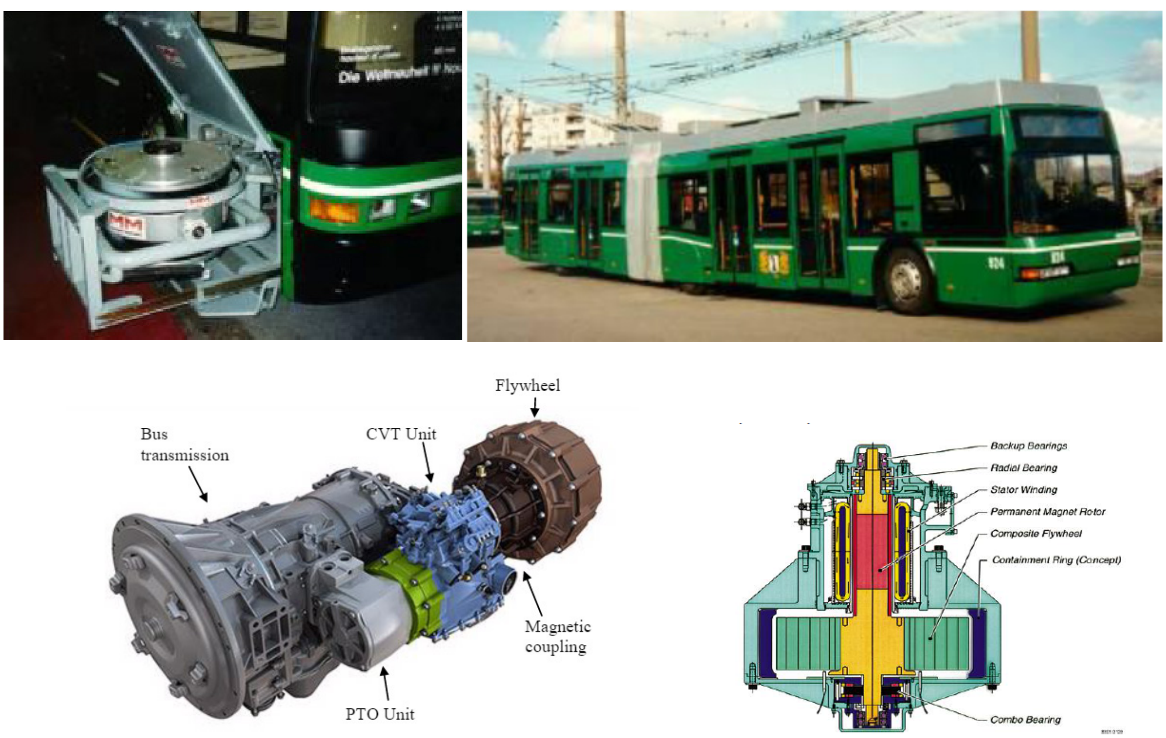

What separates the INSTAR system from these earlier vehicular flywheel energy storage systems is how the INSTAR system does not try to rely solely on the flywheel for regenerative braking energy storage, but incorporates both a chemical battery and a flywheel together. A more comparable system might not use a flywheel at all, but instead a different form of high power energy storage that can work in tandem with a battery.

Section 2.03 Vehicular Supercapacitor Energy Storage Systems

Supercapacitor energy storage systems are the most closely related technology that can fill the same role as the INSTAR flywheel energy storage system. Providing high power, but only in short bursts, capacitors are commonly used to store energy electrostatically to smooth out current flow in circuits. Indeed, while many refer to flywheels as mechanical batteries, the INSTAR flywheel is implemented in a manner much closer to a mechanical capacitor. Researchers in Chile have demonstrated 6-8% energy savings by constructing a chemical battery and supercapacitor hybrid vehicle [14]. While there are many attractive benefits of using supercapacitors, especially their inherent lack of moving parts, they have relatively low energy density and are still prohibitively expensive [15].

Section 2.04 Vehicular Hydraulic/Pneumatic Energy Storage Systems

Hydraulic and pneumatic systems are another form of mechanical energy storage. Rather than storing energy as rotational kinetic energy like a flywheel, it is stored in the internal energy of a pressurized fluid. This energy can quickly be released (i.e. through a turbine generator) in order to convert it back into electricity. While this system has been shown to be able to improve vehicular energy efficiency through its ability to provide regenerative braking [16], it can also suffer from low energy density, especially volumetric energy density [Wh/m^3] as the accumulator for a large vehicle can be quite large.

Figure II-7 Hydraulic Regenerative Braking Test Vehicle

(Courtesy of Center for Compact and Efficient Fluid Power)

Chapter III. INSTAR System Design

The INSTAR system is a constraint-driven design that must balance multiple factors at once: high performance, low weight, low volume, high reliability, and low cost.

High performance, measured here by both roundtrip flywheel energy storage efficiency and overall system efficiency, is of course the main goal of the system. Round trip efficiency in flywheel systems can be thought of as a minimization of the losses associated with absorbing, storing, and reusing the energy put into the system. These losses are covered in greater detail in Chapter IV. The complete minimization of these losses, however, is not the goal of the INSTAR system. Instead it must be weighed against the other critical design constraints as it is unlikely for a system of this nature to be implemented in future production vehicles if the other constraints are over-sacrificed.

Cost and reliability are two constraints given less importance by previous implementations, but are of critical importance in any successful, large-scale design implementation. High performance, professional racing vehicles have successfully demonstrated the energy capture and reuse strategy of a flywheel-based energy storage system. However, these competitions have no requirements on the re-use of components between races, effectively encouraging complete overhauls and component replacement between uses in order to maximize performance. The trade-off is a prohibitively high system operation costs and manufacturing costs that relegate these system designs to only the cutting edge racing circuits. The INSTAR system shows that the majority of the benefits can still be gained without neglecting cost and reliability constraints by the use of commodity components and intentionally minimizing flywheel storage time through its software power management scheme.

The requirement for low weight and volume are of particular importance in vehicular applications where additional weight and volume require the use of extra fuel to power the vehicle due to higher frictional and aerodynamic losses. This additional fuel use is directly counter to the performance goal of the system and must always be accounted for in any design decision, whether it be geometric sizing, component selection, or material selection.

Each one of these must be taken into consideration while never losing sight of the ultimate goal: an overall increase in system efficiency.

Section 3.01 Electric Go-Kart Test Platform

An electric vehicle was designed and built to serve as a test platform for the INSTAR system (see Figure III-1). This allows for the system design decisions and system performance testing to be motivated by more realistic conditions. The eventual goal is to test the system while implemented on to a gasoline and chemical battery hybrid vehicle, but a custom-built electric go-kart based on a gasoline-powered go-kart chassis provided a flexible testing platform while larger funding sources are sought out. A major benefit of the go-kart testing platform is that the small size allowed for the INSTAR team to easily test the performance of the system both inside (with suspended drive wheels) and outside the laboratory. The open architecture of the go-kart chassis also allowed for faster development time and made it possible for over fifteen undergraduate volunteer researchers to contribute to the construction of the kart, many of whom had little to no design experience before joining. Their contributions made this dissertation possible as both the entirety of the flywheel energy storage system and the test platform were built over the past 5 years.

Figure III-1 INSTAR Electric Vehicle Test Platform

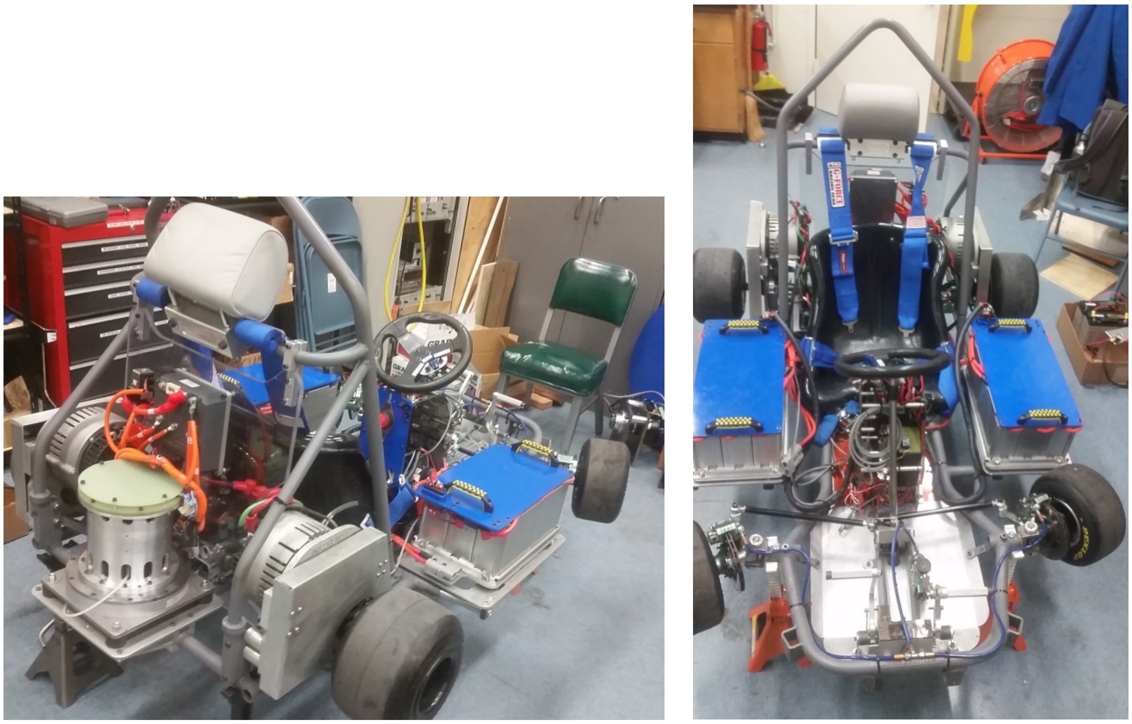

(a) Traction Motors

The go-kart test platform was originally powered by a two-stroke gasoline engine driving a solid rear axle. This propulsion system was replaced by two 12 kW Mars Motors DC brushless, axial flux motors. The rear axle was split into two independent sides, with one motor powering each side through a single speed 2:1 ratio chain and sprocket drive. With a maximum rated speed of 5,000 RPM, the motors are capable of propelling the go-kart to well over 60 mph with its Ø11.5” (Ø29 cm) wheels and can each provide 53 Nm of torque at the motor shaft. They are each rated to a peak current consumption of 300 amps for one minute and a continuous current of 80 amps. The motors are capable of 53 Nm of regenerative braking. Based on the 0.1830 Nm/Amp torque constant (0.0180 Volts/RPM motor constant), this can provide as much as 290 amps. The motors are each controlled by a Sevcon Gen4 motor controller that sends and receives commands via a CANOpen CAN communication bus.

(b) Battery Pack

The go-kart is powered by two 20Ah, 80V $LiFePO_4$ battery packs connected in parallel, providing the equivalent of an 80V 40Ah battery pack. Each pack has 24 nominal 3.3V cells in series, packaged in six enclosures containing four cells each and purchased off-the-shelf (see Figure III-3). 4 gauge wire carries the power from the battery packs, to the motor controllers, and on to the motors. Both packs are monitored by an Elithion battery management system providing instantaneous measurement of each cell voltage and charging and/or discharging each cell in order to maintain balance among the individual cells. While fully capable of charging or discharging at upwards of 100 amps for a brief amount of time, the packs are regularly charged from the INSTAR lab's DC power supply at 2.5 amps (C/16) between testing sessions. Each pack has a 150 amp fuse and is mounted to the go-kart chassis through vibration-isolating rubber mounts. The battery packs were designed and built by INSTAR lab member Toby Ricco.

Figure III-2 INSTAR Test Vehicle Wiring Diagram

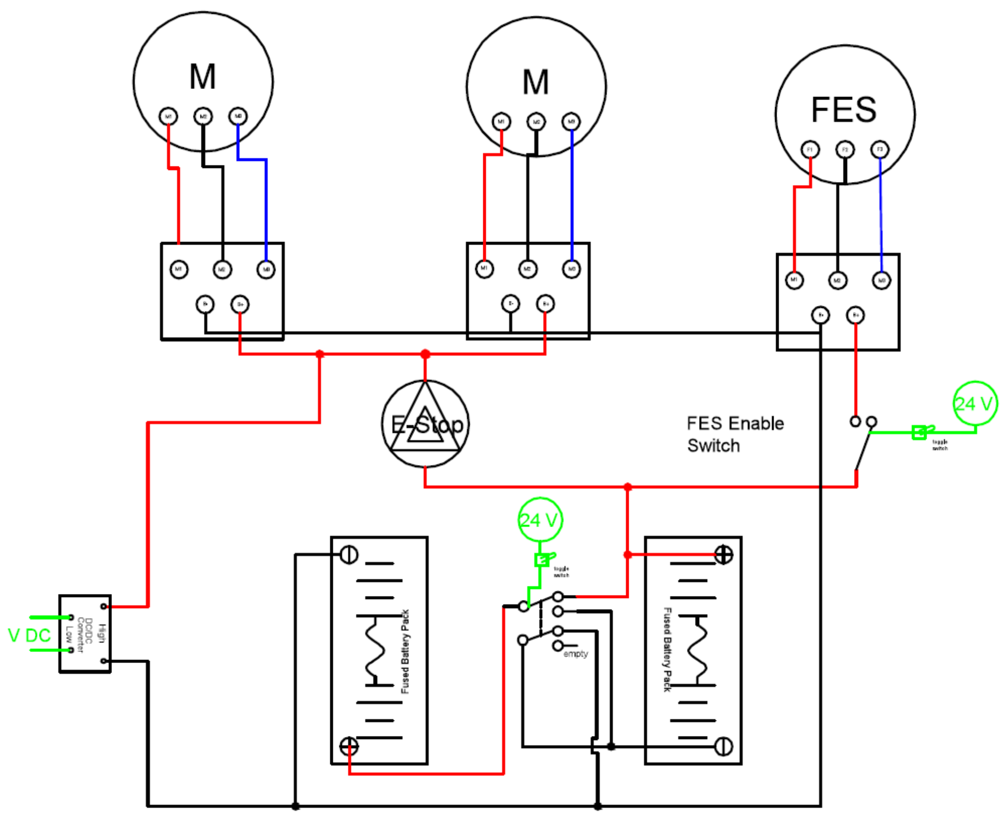

Figure III-3 INSTAR Test Vehicle Battery Packs

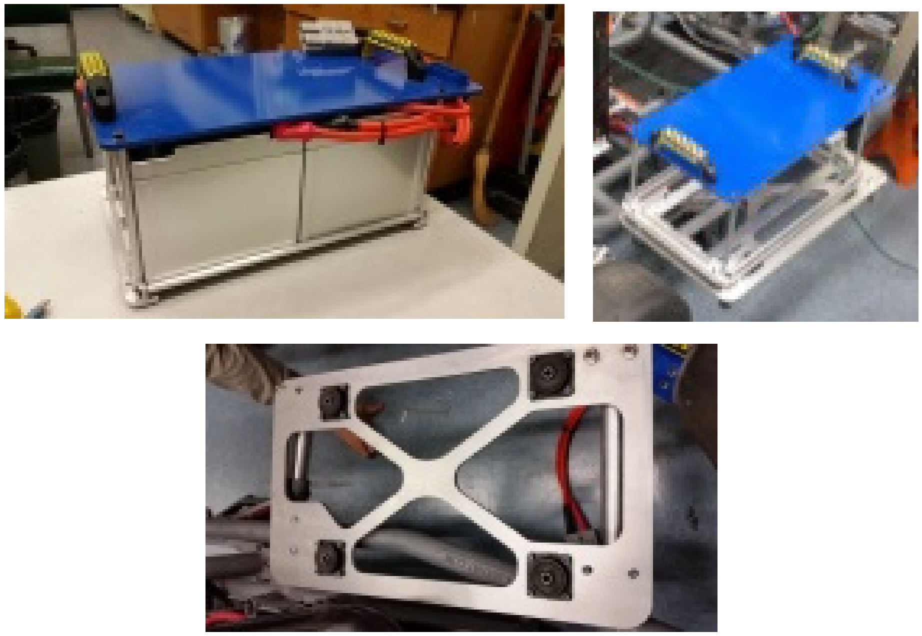

(c) Instrumentation

The go-kart has an array of sensors installed to provide both control and feedback to the LabView system controller, discussed below. This array includes:

- Absolute rotary digital encoders on both the brake pedal and accelerator pedal outputting a pulse width modulation signal with duty cycle proportional to the angular position
- Non-invasive, Temura Hall-Effect current sensors monitoring the battery pack current rated to 200A
- Voltage sensor monitoring the pack voltage
- Motor controller current sensors reporting individual motor controller current flow
- Motor speed and direction as reported by the motor controller
- Absolute rotary digital encoder measuring the steering angle for use in a custom-designed software rear-wheel differential (not used during INSTAR testing)

These sensors are powered by the 80V battery pack, routed through an 80V-12V DC-DC converter and a 12V-5V DC-DC converter (if needed).

The go-kart also has hardware brake blending that provides for a prioritization of regenerative braking before engagement of the mechanical disk brakes installed on the front (unpowered) wheels. This system has a compression spring in the brake pedal assembly that allows for brake pedal travel, rotating the digital encoder and signaling a braking request, without pulling on the master brake cylinder. Only after 30° of brake pedal rotation does the spring fully compress and the master cylinder engages. This system was designed and built by INSTAR lab member Matt Dethlefsen.

(d) LabView

The INSTAR controls are all performed by a National Instruments cRIO-9076. This system has a 400 MHz real-time processor and a Spartan-6 LX45 FPGA. It contains both analog and digital input/output modules to read all of the sensor signals and output CAN messages to the traction motor controllers and the flywheel motor controller. All aspects of the INSTAR controller are performed on the FPGA for faster speed: signal input, command output, and power flow logic. The real-time processor is used for in-laboratory testing where the throttle and brake commands can be controlled, via direct Ethernet connection, by a desktop computer running LabView. All system conditions: current, voltage, wheel speed, flywheel speed, etc can be viewed on the desktop while connected to the kart in the laboratory. The data is logged for post-processing at 200 hz. This data collection provides the necessary information for the full-system testing that will be discussed in Chapter V.

The code is also compiled into an .exe file that can run on go-kart startup to allow for the vehicle to drive around untethered (see Figure III-4). This also allows for on-vehicle data collection. Figure III-5 contains current and voltage data from a four minute testing session while driving the kart on the UC Berkeley campus.

A peak discharge current of 300 amps (7.5C) was measured during hard acceleration and a peak charging current of 100 amps (2.5C) was measured during hard regenerative braking. These large currents heavily tax the battery pack, as the battery pack voltage momentarily drops to 55 Volts during high discharge events. This data was measured by the Temura Hall-Effect Sensor through the cRIO FPGA.

Figure III-4 Electric Vehicle Test Platform In Operation

Figure III-5 Test Data Collected During Kart Operation without the INSTAR System

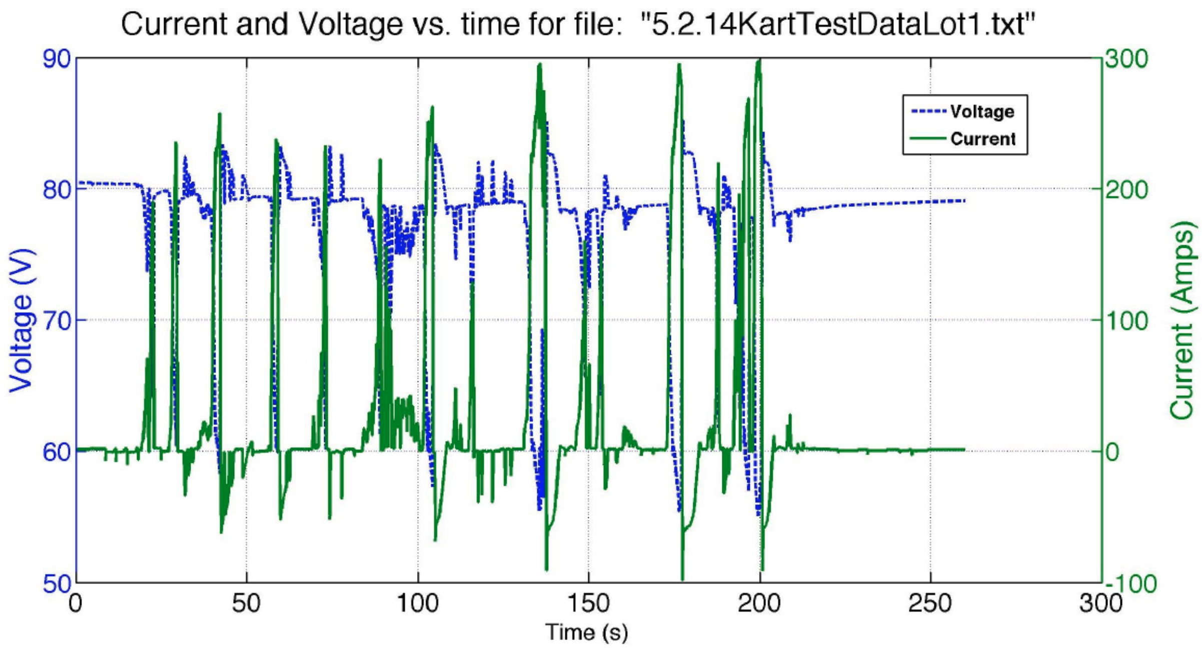

Section 3.02 Flywheel Energy Storage System

(a) Flywheel Spindle

The heart of the INSTAR system's energy storage system is the flywheel. What actually allows the flywheel to store energy at all is the spindle - allowing the flywheel disk to smoothly rotate (as close to effortlessly as is practical) and collect rotational kinetic energy through the motor. Keeping the overall system design goals of high efficiency and low cost in mind, the design of the spindle entails some of the most critical design decisions that will lead to the success, or failure, of this new type of energy storage system. The main components that will be discussed in detail are, in order: the bearings that allow rotation, the flywheel disk to store rotational kinetic energy, the vacuum system to reduce the air resistance drag on the disk, and the rotating shaft and non-rotating structural housing that supports each of the previously discussed components.

(i) Spindle Bearings

The largest decision driving down the cost and complexity of the flywheel energy storage system is the use of ball bearings. Energy density is of critical importance in vehicular applications, and as will be discussed in more detail in (ii), higher flywheel speed provides higher levels of energy storage, regardless of mass. A faster rotation rate can allow for higher energy density, as seen with composite flywheels capable of speeds in excess of 50,000 RPM [12]. These speeds, however, are generally impractical, or impossible, to reach with ball bearings. This search for higher energy density through higher rotation rates has motivated the development of magnetic levitation bearing systems.

The INSTAR system, however, leverages a power management scheme that only requires energy to be stored in the flywheel for a few minutes maximum, very commonly for less than 15 seconds. Despite the higher frictional losses of ball bearings, this short storage time reduces the impact of parasitic losses on the overall system performance, and commodity ball bearings can be successfully employed. High-speed, precision ball bearings have been around for many decades and the engineering behind them is as time-tested as almost any technology in existence. This not only lends itself to high system reliability, but also lower costs as there are multiple experienced vendors competing for the business of many different industries and driving down costs.

The most important selection factors for the INSTAR flywheel spindle are low friction, long lifetime, and low cost. Both the friction and lifetime are driven by the rotation rate and load supported by the bearing. Cost is mainly driven by material selection, bearing design, and required bearing quantity. While these factors all appear to be mutually exclusive, and they generally are, the INSTAR system is capable of achieving sufficiently low friction, long life, and low cost due, again, to the INSTAR system's power management scheme. Because the INSTAR system uses both the battery pack and the flywheel to store braking energy, only a fraction of the available regenerative braking energy needs to be absorbed by the flywheel. As described earlier, the energy only needs to be stored for a maximum of a few minutes. This small energy requirement and short storage time results in flywheel masses under 100 kg, even for the largest of vehicles. This type of load is *well* below the load ratings of modern ball bearings, which are capable of supporting more than 10,000 N in dynamic radial loading. The selection choices for bearings are also quite limited above 25,000 RPM, and this was chosen as the practical limit for the INSTAR system in order to allow for continued ball bearing use.

To prove the feasibility of using ball bearings, the INSTAR system uses two FAG 6205-C deep groove radial ball bearings, rated to 21,600 RPM and 15,000 N dynamic radial load. As will be discussed in (ii), the bearings will need to support the 8.5kg mass of the disk, shaft, and motor rotor. Based on previous simulations [17], the average speed of the disk over a typical urban driving profile (provided by the EPA LA92 Unified Driving Schedule) is ~12,000 RPM. The expected lifetime of the bearings uses the well-established L_{10} life equation that provides an estimate of the life that 90% of apparently identical ball bearings will complete or exceed before a 6mm^2 fatigue spall develops.

Equation III-1

$$L_{10} = \left(\frac{C_r}{P_r}\right)^3 (1x10^6)\ revolutions$$

$$or$$

$$L_{10} = \left(\frac{C_r}{P_r}\right)^3 \left(\frac{1x10^6}{60 \cdot n}\right)\ hours$$

From this estimate the bearings should last over 35,000 hours at 12,000 RPM with a larger, 20 kg flywheel mass. With each stop averaging one minute of flywheel rotation before the stored energy is put back into the drive motors or the battery pack this is over 2.2 million stops. At 10 stops per mile over the life of a delivery truck, this is over 200,000 miles of driving. While this needs to be experimentally validated, the results prove to be very promising from a lifetime perspective.

The friction of the bearings, which manifests as a torque on the rotating shaft and is dissipated as heat, can be estimated using [18]:

Equation III-2

$$T_{bearings} = 2Ff_m\left(\frac{D_m}{2}\right) + D_m^3(\eta\omega)^3\rho^{\frac{2}{3}}$$

This not only takes into the rolling friction from both bearings, but also friction from the viscous churning of the lubrication that increases with speed. For the INSTAR proof of concept prototype (see Table III-1) this results in a torque of 0.4 Nm at 25,000 RPM and hence a power loss of 70 Watts. At the more common 12,000 RPM speed this loss is 25 Watts. This calculation will also be experimentally investigated in Chapter IV, as the bearing selection is one of the most important design decisions for the INSTAR overall performance.

Table III-1 INSTAR Bearing Loss Specifications

Single Row Oil- Lubricated Ball Bearings
$f_m = 0.0015$
F = $M_{flywheel} \cdot g = 82\ N$
$\eta = 2.6\ \frac{mm^2}{s}$
$\rho = 0.85\ \frac{g}{cm^3}$
$D_m = 25mm$

Figure III-6 INSTAR Ball Bearing and Wave Spring

While the bottom bearing is preloaded by the weight of the flywheel, the top bearing is pre-loaded with wave-springs (see right side of Figure III-6, courtesy of Smalley) to provide compliance for thermal expansion, reduce vibration, and minimize run-out.

The top bearing is a floating bearing that only provides radial support. The bottom bearing bears the weight of the shaft, flywheel disk, motor rotor, any magnetic axial force, and the top bearing pre-load as an axial load. This total weight of 8.25 kg, is 1.25% of the 7800 N rated static axial load.

(ii) Flywheel Disk

The flywheel disk design affects not only the other major component design decisions, but also drives many of the flywheel's key performance measures (i.e. energy density). The weight of the disk accounts for over 25% of the total system weight of the prototype design, but more importantly, can account for over 60% of a flywheel system for a larger vehicle. The design complexity and material choice also significantly affects the total system manufacturing cost. For the purposes of this proof of concept INSTAR system a simple disk shape will suffice. This basic shape allows for simple manufacturing processes to provide a well-balanced, highly reliable, and low cost shape made of commonly available materials. It also allows for accurate energy and stress modeling as constant thickness solid disks have well-established analytical equations describing their behavior.

Sizing the flywheel disks is one of the most important design decisions for this type of system. Too large and the energy density suffers, with excessive weight leading to low vehicular system efficiency. Too small and not enough energy is recaptured during braking to justify the added weight and complexity of the system. While the sizing is best done in terms of energy storage, it eventually needs to be translated into a flywheel disk shape. This is accomplished by examining how much energy is stored in the disk as it rotates, as is shown in Equation III-3:

Equation III-3

$$Energy_{flywheel} = \frac{1}{2}\, I\ \omega^2$$

There are two components to this calculation, the moment of inertia (I) and the rotation rate (ω). The moment of inertia is driven by the material choice and the design geometry, as described by Equation III-4 for a solid disk of constant thickness (t), material density (ρ), and outer radius (r).

Equation III-4

$$Moment\ of\ Inertia = I = \frac{1}{2}\, m\ r^2$$

$$mass = m = \pi \rho r^2 t$$

$$\therefore\ Moment\ of\ Inertia = I = \frac{1}{2}\, \pi \rho r^4 t$$

For the given maximum practical ball bearing speed of 25,000 RPM (2618 rad/s), this allows for a minimum moment of inertia (MoI) to be determined by the amount of energy storage deemed necessary by the specific application. The amount of energy storage in the go-kart was first calculated by looking at the vehicle's kinetic energy before braking (see Equation III-5) and then validating it through the simulation performed in [17].

Equation III-5

$$Kinetic\ Energy_{vehicle} = \frac{1}{2}\, m\, v^2$$

For the 500 lb [225 kg] kart traveling at 40 mph [18 m/s], this is 36 kJ. The flywheel also has an energy storage buffer to account for potential energy gains (eg descending a Berkeley hill) that are not vehicle speed-based. 100 kJ of energy storage was chosen to provide for two full braking events in addition to a 40 foot descent to be absorbed by the flywheel. While this amount does not take air resistance, tire friction, or motor efficiency into account, it must be emphasized that this proof of concept INSTAR has been designed to have an excess of storage capability to ensure the testing is not limited by the storage capacity. While this results in lower system energy density, this prototype was not designed for optimal energy density to begin with. Other design considerations (e.g. ease of testing and ease of maintenance) take precedence for this specific prototype design. Full system testing in real world driving scenarios can better inform this requirement.

This energy requirement results in a minimum necessary MoI of 2.92×10^{-2} kg·m^2 . Equation III-4 allows for a wide range of flywheel disk radii and thickness combinations to be chosen from. While larger radii provide a more efficient use of mass, resulting in higher energy density [kJ/kg], they also necessitate larger housings, with its added weight, to enclose them. The larger disk diameters also result in higher hoop stress values for the disk.

While the flywheel can be modeled as a solid disk for energy storage calculation purposes, the INSTAR prototype flywheel (and most likely any implementation of an INSTAR system on a larger vehicle) does not actually use a solid disk shape. Instead, a disk with a hole at the center will be manufactured as a solid piece, or stack of solid pieces, and then attached to the spindle shaft. The end shape can be described as a solid disk for energy storage calculation purposes as the shaft material fills in the center hole, but this simplified modeled is insufficient for stress analysis calculations. The disk must be modeled as it, a solid disk with a hole at the center with stress distribution described by Equation III-6.

Equation III-6

$$\sigma_{Hoop} = \left(\frac{\rho\omega^2}{8}\right)\left[(3+\nu)\left(R_i^2 + R_o^2 + \frac{R_i^2 \cdot R_o^2}{r^2}\right) - (1+3\nu)r^2\right]$$

$$\sigma_{Radial} = (3+\nu)\ \left(\frac{\rho\omega^2}{8}\right)\ \left[R_i^2 + R_o^2 + \frac{R_i^2 \cdot R_o^2}{r^2} - r^2\right]$$

$$\sigma_{Hoop,max} = \sigma_{Hoop,\,r=R_i} = \frac{\rho\omega^2}{4}\ [(1-\nu)R_i^2 + (3+\nu)R_o^2]$$

$$\sigma_{Radial,max} = \sigma_{Radial,\ \ r=\sqrt{R_i \cdot R_o}} = (3+\nu)\ \left(\frac{\rho\omega^2}{8}\right)\ (R_o - R_i)^2$$

$$where \quad \begin{array}{l} R_i = inner\ radius \\ R_o = outer\ radius \end{array} \quad \begin{array}{l} \upsilon = Poisson's\ Ratio \\ \omega = angular\ velocity \\ \rho = material\ density \end{array}$$

The hoop stress is highest towards the center of the disk, with the mass at the outside of the disk essentially "pulling" on the inner material as it rotates at high tangential velocity. The radial stress peaks more towards the middle of the disk. The INSTAR flywheel disk factor of safety calculations use the Von Mises effective stress of these two orthogonal stress components. The form of these stress equations also provides insight into why more complex flywheels have a thick hub, spokes, and outer rim. This places more material near the center to handle the high hoops stress, high tensile strength spokes to handle the peak radial stress in the middle, and more material at the outer radius where it is more efficiently used with regards to energy density [kJ/kg]. It also explains the attempts to create hybrid flywheels using steel hubs and composite rims, which can handle extremely high loads in the fiber direction. These types of flywheel, however, are much more complex and expensive to manufacture.

The relatively slow speed of the INSTAR flywheel (limited by the use of ball bearings) also means a relatively large MoI is needed. In order to avoid large volumes, in excess of 1 m^3, a large material density is needed in order to provide enough mass in smaller volumes. The prototype flywheel was also to be mounted in a 1 cubic foot space on the electric vehicle test platform and this volume was set as the design constraint. This relatively small space is still a challenge to package in a modern commuter vehicle, but should be acceptable for delivery trucks. Steel is an excellent flywheel material option based on its density, strength, and status as a commodity material. Manufacturers are very experienced working with it and stock many different varieties. This aids in keeping the INSTAR system's costs low.

17-4 PH (precipitation hardened) stainless steel with H900 heat treatment was chosen for its high strength and low cost. Many local contract manufacturing shops have worked with the material and offered competitive quotes for the prototype flywheel disk. With a yield strength of 1380 MPa, this high strength material provided the confidence to require a factor of safety of two for the flywheel spinning at max speed (25,000) RPM without worry of over-complicating the design. This design constraint is collected with the previous constraints into Table III-2.

Table III-2 INSTAR Flywheel Design Requirements

Flywheel Design Requirements		
Energy Storage	>	100 kJ
ω	<	25,000 RPM
Factor of Safety	>	2 @ 25,000 RPM
Volume	<	1 ft^3

A range of disk radii, thickness, and intended angular velocity were considered for the flywheel disk shape – from a 4” diameter and15” thick rod spinning at 25,000 RPM, to a 12” diameter and 0.4” thick pancake shaped-disk spinning at 17,000 RPM, to a 16” diameter and 1” thick plate (see Appendix A). An 8” diameter, 1” thick disk spinning at 25,000 RPM was chosen for its moderate weight (6.4 kg), ease of manufacturing, and necessary housing volume (see Table III-3). As it will be discussed later in Chapter IV), the tangential velocity at the outer radius plays an important role in the windage drag losses, but this loss was found to be comparable to the seal losses required to maintain the vacuum in the first place. This does, however, provide some encouragement to keep the diameter small to reduce those losses. It must be emphasized that the benefit of lower windage drag losses due to smaller flywheel diameters pales in comparison to the most important factor: energy storage. Multiple sizes could have been selected and the MoI allows for a comparison quantity between the design options for a given speed, but this of course is again dependent on the real driving force behind the key sizing component –necessary energy storage.

Table III-3 INSTAR Prototype Flywheel Specifications

Prototype Flywheel Dimensions and Measurements		
Diameter Ø	8 [20.3]	Inches [cm]
Thickness	1 [2.54]	Inches [cm]
Energy Storage	112.9 [31.4]	kJ [Wh]
ω	25,000 [2,618]	RPM [rad/s]
Factor of Safety	2.3	
MoI	3.29×10^{-2}	$kg \cdot m^2$
Mass	14.1 [6.4]	Lb [kg]

The disk will be mated to the spindle shaft by a temperature-induced expansion fit. The disk is heated to expand the inner radius, while the mating shaft is cooled for temperature-induced contraction to shrink its out diameter. The cool shaft is then inserted into the heated disk and the two parts are brought back to room temperature. The disk inner radius and mating shaft outer diameter are dimensioned to result in a 0.001" interference fit on the diameter once assembled. This also necessitates a 0.001" cylindricity tolerance on the center disk hole to ensure that the assembled flywheel mass and shaft run true. Flatness and perpendicularity tolerances are also added to reduce imbalance, although the assembled shaft, disk, and rotor were sent out for independent balancing as well. A finite element analysis of the assembled disk and shaft was performed to validate the analytical results and was in good agreement. This should not be surprising for such a simple shape.

Figure III-7 Flywheel Mass Drawing

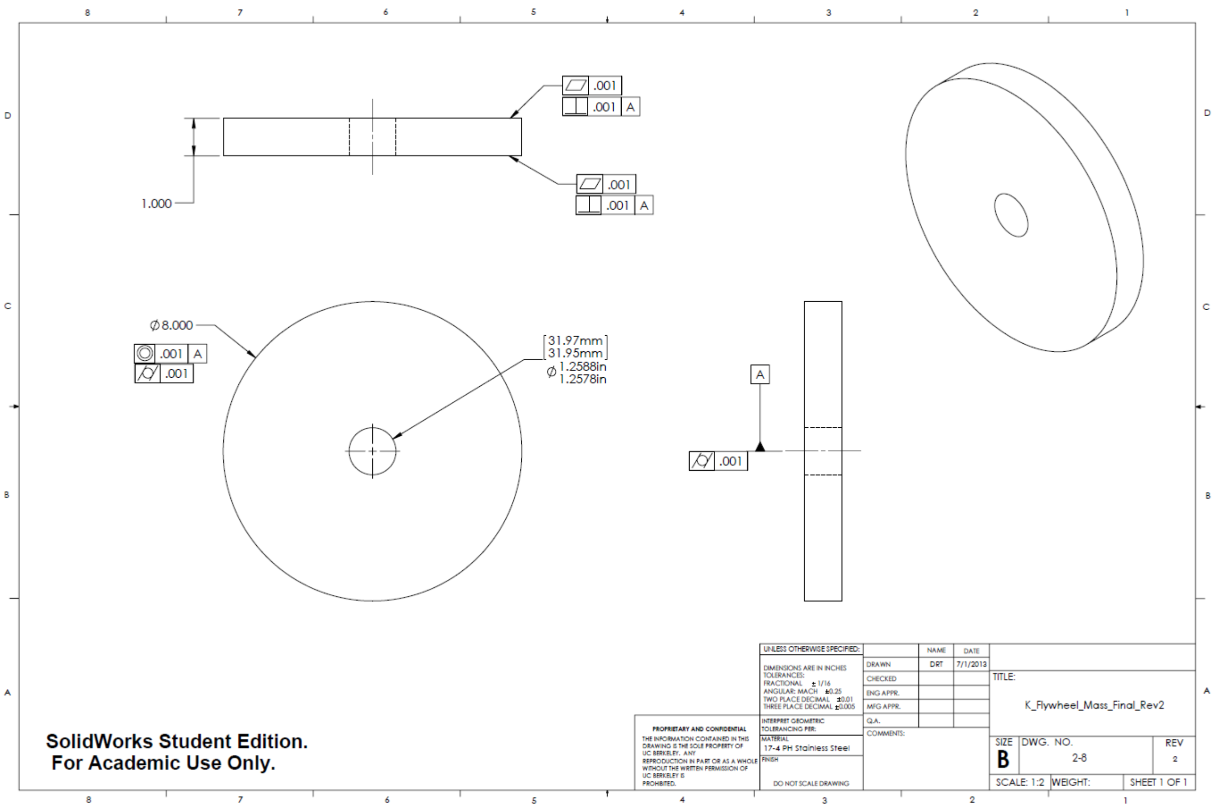

Figure III-8 Flywheel Mass and Shaft FEA Results

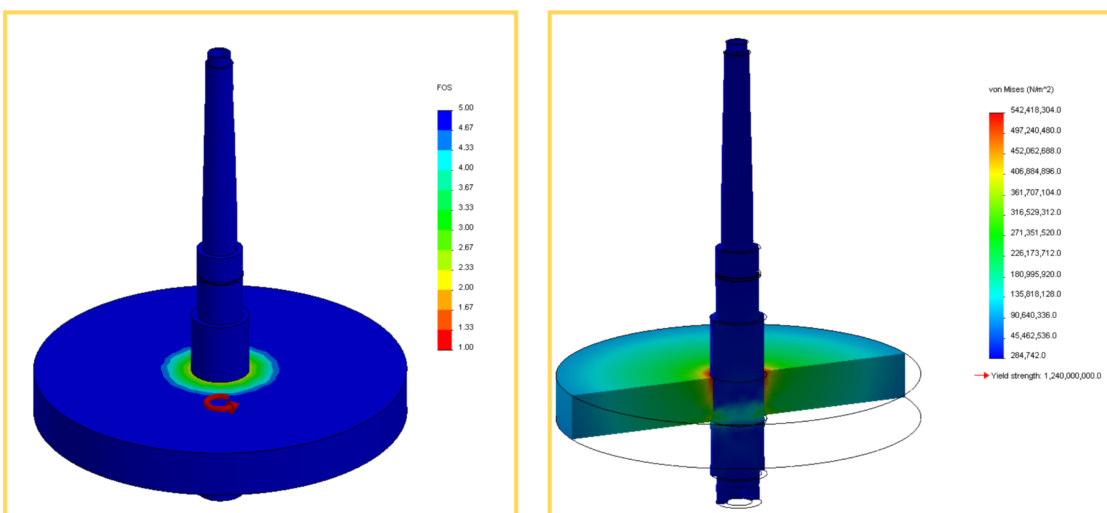

Figure III-9 Machined INSTAR Prototype Flywheel

(iii) Flywheel Vacuum System

The INSTAR flywheel energy storage prototype was designed to test the feasibility and benefit of running a vacuum system to reduce the wind resistance on the spinning disk, known as windage losses or air drag losses. This drag loss increases primarily with: the flywheel rotational speed and the gap between the flywheel disk and the enclosure surrounding it. This gap size affects the amount of turbulence in the air inside the vacuum chamber, described by the Reynold's number. The drag loss is reduced with lower fluid density, which drops with the reduced pressure from the vacuum. The benefit of the vacuum system would be a reduction in storage loss of the flywheel, allowing it to retain its rotational kinetic energy more effectively over time. It can be though thought of as a parasitic power loss. This avoided power loss is first compared to the power required to run the vacuum pump that will be required to maintain the vacuum in the flywheel.

The amount of expected power loss is plotted at three different absolute pressure levels: atmospheric pressure for comparison, 7 PSI absolute (a reduction of approximately 7 PSI compared to atmospheric), and 3 PSI absolute (a reduction of 11 PSI compared to atmospheric) using windage calculations derived from Couette-Taylor flow between a rotating inner and fixed outer cylinder [19]. This is not a significant vacuum level, especially when compared to the 10-3 torr (0.19 PSI – 0.06 PSI) vacuums tested for high speed flywheels in the past [20] and should not be hard to maintain with a standard 12V automotive vacuum pump using 5 watts, especially given the small pumped volume of only 3 cm^3.

Figure III-10 Flywheel Windage Drag Calculation Plot

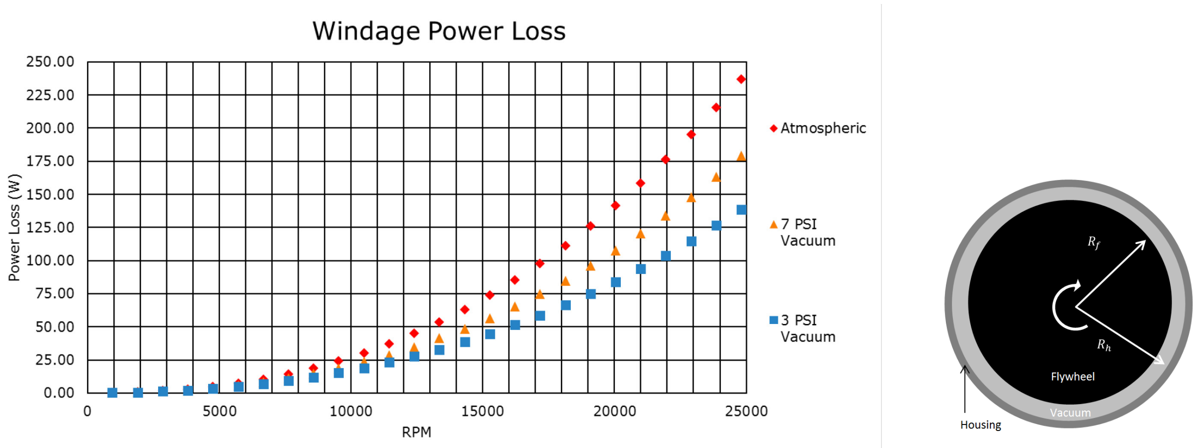

Equation III-7 Flywheel Windage Drag Calculation

$$Power\ Loss = \omega \cdot Torque = \omega \rho v^2 H \frac{\eta^{\frac{3}{2}}}{(1-\eta)^{\frac{7}{4}}} Re^{\frac{3}{2}}$$

$$Re = \frac{\omega R_f (R_h - R_f)}{\nu} \qquad \eta = \frac{R_f}{R_h} \qquad where \quad \begin{array}{l} R_f = flywhee;\ outer\ radius \\ R_i = housing\ inner\ radius \end{array} \quad \begin{array}{c} \upsilon = kinematic\ viscosity \\ \omega = angular\ velocity \\ \rho = air\ density \end{array}$$

From this calculation there is an expected benefit, especially at high speeds, as much as 100 watts at max speed for the 3 PSI case. While promising, this calculation does not factor in the drag torque from the shaft seals required to seal the enclosure and allow the pump to maintain the vacuum. The number of seals depends on the design and can conceivably range from one for a cantilevered design (see Figure III-11) to three for a split spindle as is used for the INSTAR prototype flywheel system.

Figure III-11 Potential Flywheel Spindle Design with Single Seal Vacuum System

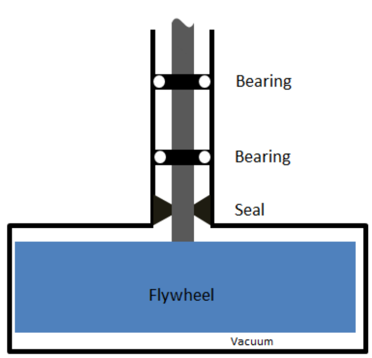

Teflon (PTFE) lip seals were chosen to see if a single seal would be capable of maintaining this level of vacuum at the rated speed of 25,000 RPM. The Trelleborg Turcon Varilip PTFE lip seal is capable of maintaining a 73 PSI difference across the single sealing surface and resisting temperatures upwards of 200 C. This single contact point reduces the parasitic torque from the friction of the seal against the rotating shaft (see Figure III-12).

Figure III-12 Trelleborg Sealing Solutions Varilip PDR PTFE Lip Seal

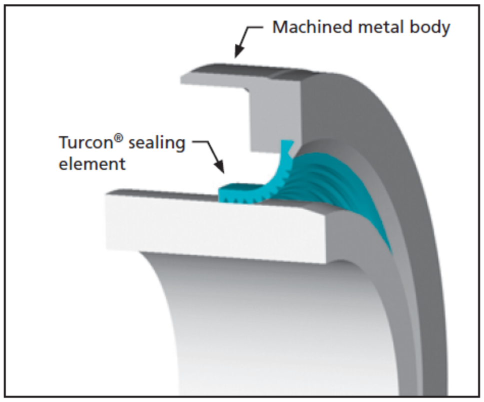

Custom lip seals were ordered from Trelleborg Sealing Solutions, with a cost of $38.33 USD each at an order size of 25. Prices drop to $15.76 for an order size of 5,000 and $14.30 for an order size of 10,000 as quoted by Trelleborg. This custom shape was only necessary to add a nitrile O-ring at the exterior of the seal housing (see Figure III-13). This was requested as the prototype flywheel was designed to be taken apart numerous times during testing and the O-ring allows for the seal to function properly while also being able to be removed easily. The O-Ring does not affect the functionality of the seal.

Figure III-13 INSTAR Lip Seal Drawing

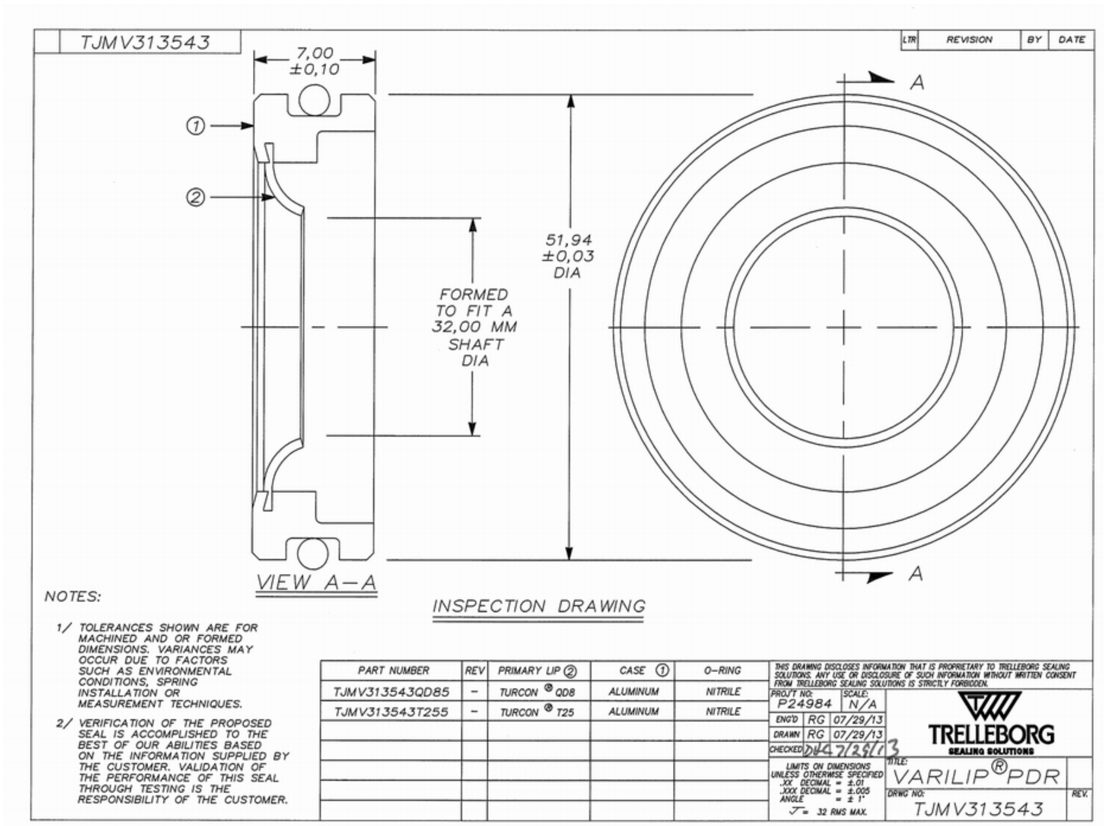

Experimental testing of this seal is further discussed in Chapter IV.

(iv) Shaft

The flywheel spindle is oriented vertically in order to minimize the gyroscopic effects of the rotating disk on vehicle handling. This orientation isolates the flywheel from vehicle yaw changes (i.e. turning). While this is often the first question that arises from people learning about the INSTAR system, it is also one of the questions answered most thoroughly by past researchers. Previous experiments with vehicular flywheel energy storage systems is that while the gyroscopic effects do affect the bearing load [21], they are not large enough to affect the vehicle [22]. In a rigidly mounted flywheel system, as is the INSTAR prototype, any change in the vehicle orientation in the pitch or roll axes also changes the flywheel spin axis orientation. Due to its angular momentum, the flywheel axis resists this motion and presses against the bearings as they are the last link that connects the vehicle to the flywheel shaft and force the axis to move. This bearing torque can be calculated using Equation III-8 from [22].

Equation III-8

$$Torque = I \cdot \omega \cdot \dot{\theta}$$

where

$I = flywheel\ moment\ of\ inertia$

$\omega = flywheel\ rotation\ rate$

$\dot{\theta} = turning\ rate\ of\ flywheel\ spin\ axis$

From [21]:

> *Exiting a steep driveway can produce a pitch rate in a transit bus of 0.24 rad/s. Hitting a speed bump at high speed or going over a [pothole] can induce bus pitch of 0.23 and 0.18 rad/s. Even worse, a hard turn by the driver can cause bus roll rates up to 1.4 rad/s.*

At 25,000 RPM and with a vehicle roll rate of 1.4 rad/s, the INSTAR flywheel presses against its bearings with a 120 Nm torque. With the 10 cm lever arm for the INSTAR spindle design, this is only 1,200 N (the bearings are rated to 15,000 N radial dynamic load). While larger flywheel system employ gimbal systems that allow the flywheel to more freely rotate and protect the high speed magnetic bearings from this type of radial load [21], that type of complexity is unnecessary for the INSTAR system due to its small size and low speed.

With the vertical orientation, the bottom bearing is designed to support the weight of the disk, shaft, and attached motor rotor. The top bearing is allowed to float to compensate for thermal expansion. The flywheel disk is placed between the two bearings for increased stiffness against disk imbalance and also to provide easier access to the bearings during assembly and disassembly. Each 32mm ID bearing sits against a shoulder on the shaft. The bottom bearing ID is captured by a shaft shoulder from above and the OD by the housing cap from below. The top bearing is captured on the ID by a shaft shoulder from below and on the OD by the wave springs and seals from above (see Figure III-14). The bearings are designed with a 0.0002" [0.005 mm] precision slip fit on to the shaft so they can be replaced if needed.

Bearing lubricants vaporize and convective heat transfer coefficients suffer in low pressure environments therefore the vacuum chamber was limited only the volume immediately surrounding the flywheel disk. The lip seals create a tight seal around the flywheel to isolate the vacuum to only that portion of the housing. As the bearings are separated by the vacuum chamber, each requires its own separate lubrication loop. This necessitates another seal above the top bearing to retain the lubrication (see Figure III-14). While this prototype used another PTFE lip seal, this is not required as it is only retaining fluid rather than both fluid and a vacuum like the other two PTFE lip seals. Each of these seals requires a 0.4 μm surface finish in order to maintain the vacuum seal. These surfaces are specifically called out on the drawing (see Figure III-15).

Figure III-14 INSTAR Spindle Layout

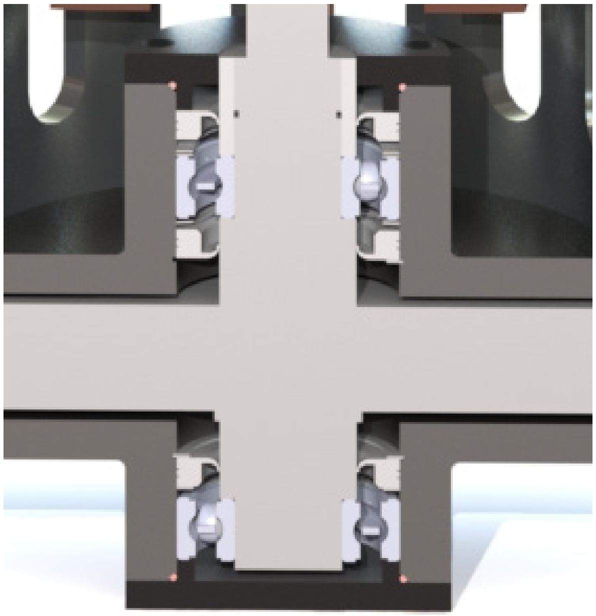

PTFE Lip Seal
Wave Spring
Bearing
Wave Spring
PTFE Lip Seal
Retaining Ring
Flywheel
Retaining Ring
PTFE Lip Seal
Wave Spring
Bearing

Figure III-15 Flywheel Shaft Drawing

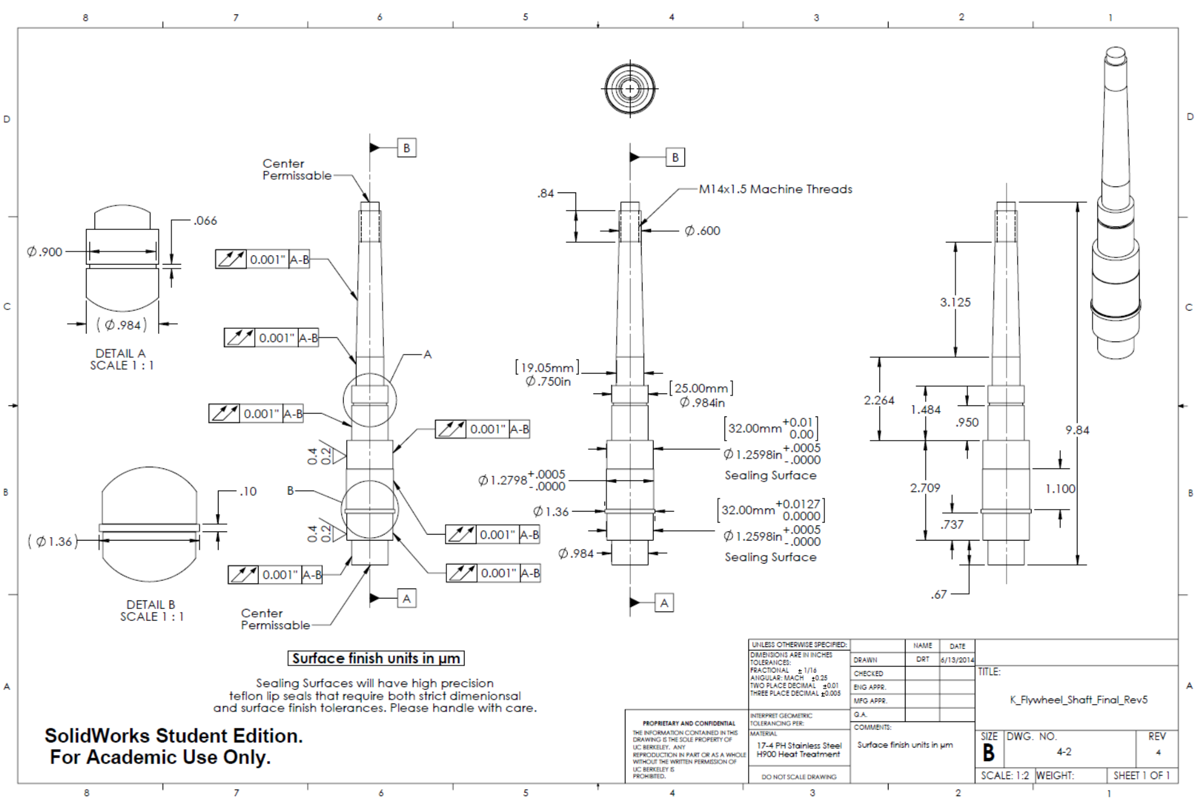

The largest diameter section of the shaft mates with the flywheel. As described earlier in (ii), a temperature-induced expansion fit provided a 0.001” [0.025 mm] interference fit between the disk ID and shaft OD. As this is a permanent and time-sensitive assembly operation, the portion of the shaft where the flywheel sits called for special attention. A small shoulder was designed so that when the heated flywheel is slipped on to the shaft during assembly the flywheel disk has a hard stop it can be quickly placed against to ensure it rests at the correct location. This section of the shaft and the flywheel ID are also 0.010” [0.25 mm] (Ø1.2798” in Figure III-15) larger on the radius to allow for more clearance between the flywheel ID and the precision-machined shaft bearing surfaces during assembly to avoid scratching the surface during this time-sensitive operation.

A Morse taper on the upper part of the shaft mates with the tapered motor hub and transfers the torque from the magnets on the rotor to the disk. An M14 nut presses, and keeps, the motor hub on to the taper. This taper showed no signs of slipping at even the highest levels of torque for the flywheel. The axial alignment of the hub inside the stator is also critical to ensure there are no unecssary motor vibrations. This axial dimension was specifically called out (see Figure III-16) and the motor hub was carefully reamed in order to meet this specification.

Figure III-16 Spindle Assembly Drawing

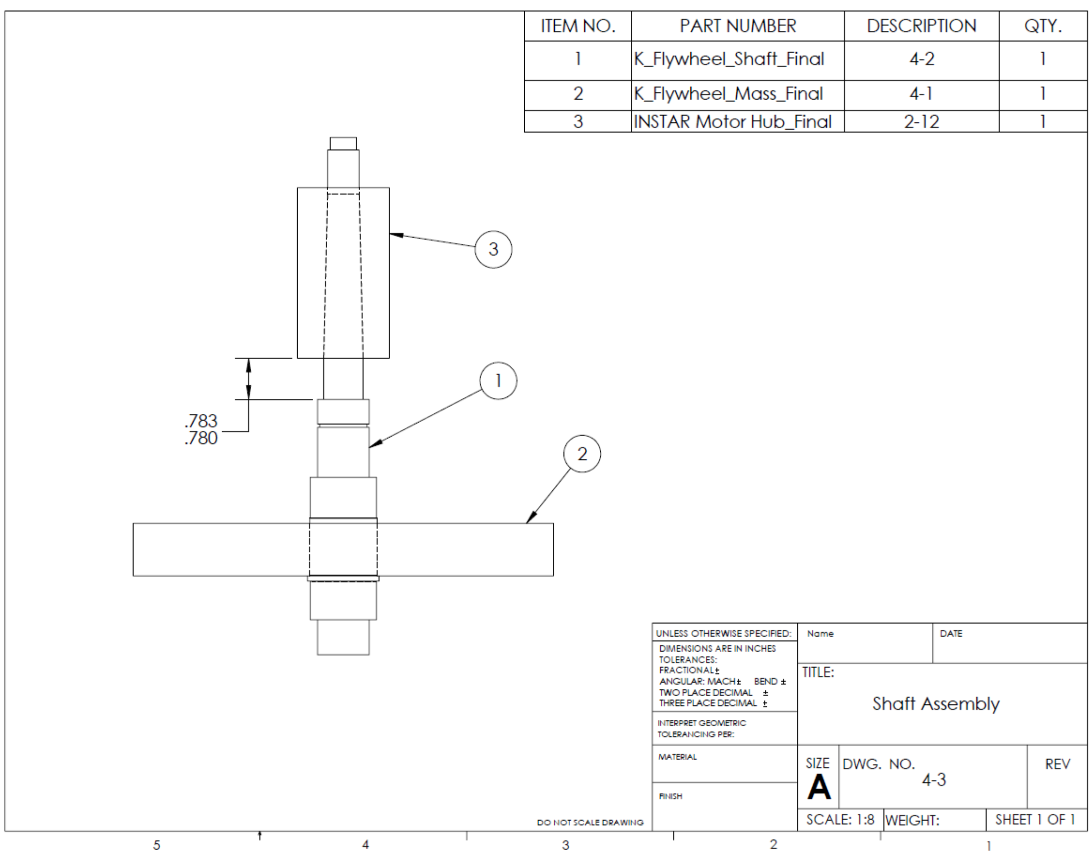

Figure III-17 Assembled and Balanced Flywheel Spindle

A total indicated runout specification was included as one of the first machined shafts tested had a non-coaxial tapered shaft section (see Figure III-18) measured as a significant runout. This resulted in a non-concentric shaft and hence a non-concentric motor. This offset mass was most likely cause of 18,000 RPM touchdown event due to centrifugal force-caused deflection.

Figure III-18 Measured Shaft Runout on First Machined Shaft

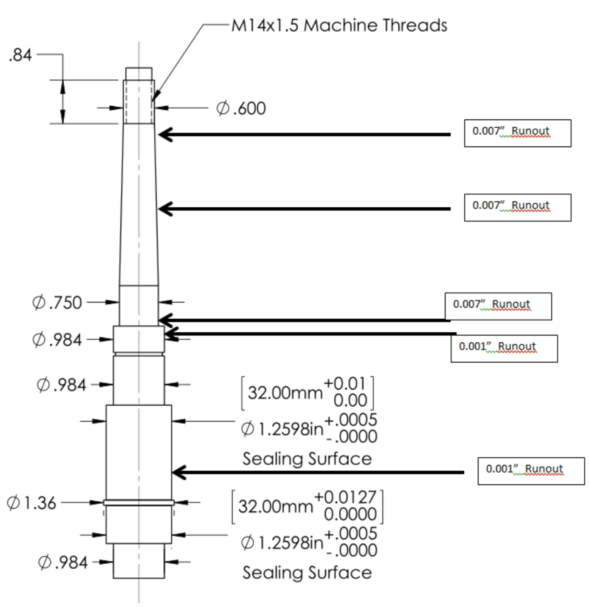

(b) Enclosure

A structural housing was designed to support and locate each of the previously discussed elements. As a result, this housing serves three main purposes:

i. Spindle alignment
ii. Vacuum sealing
iii. Burst containment

Figure III-19 INSTAR Housing CAD Drawings

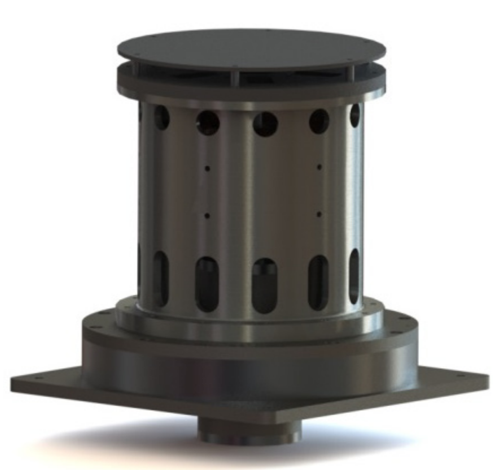

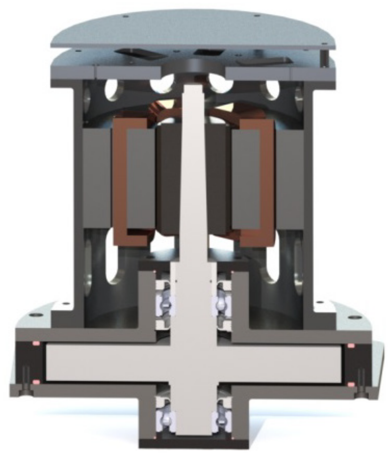

Figure III-20 INSTAR Mass Distribution and Machined Housing

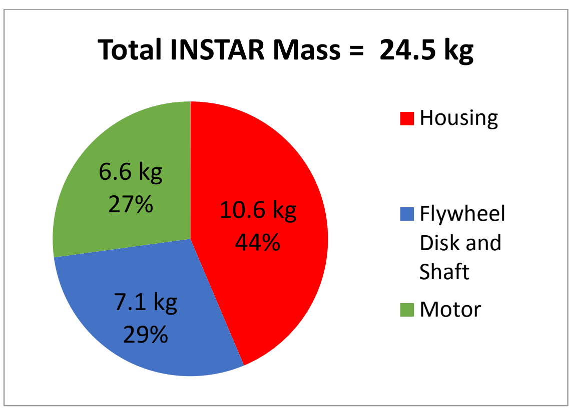

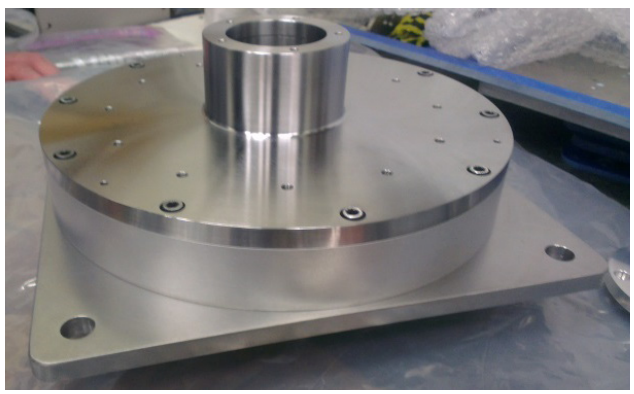

For the purposes of component analysis, modification, and replacement the housing was designed to maximize accessibility and ease of maintenance for this proof of concept flywheel system. This includes designing the housing to provide slip fits for the spindle bearings and shaft seals which will be replaced many times over the life of this prototype system while their lifetime and performance is determined. The seals are intended to be press-fit into the housing bore, but that was avoided by installing custom O-rings to provide a slip-fit for easier removal.

As described earlier in (a)(i), the bearings have the potential to last for the entire life of the vehicle and hence this type access may not be as important in a future version if this proves true. Indeed, this type of prototype-specific design requirement should be somewhat relaxed for a production version in order to minimize cost once the application-specific design has been finalized. The housing was also designed specifically to be machined with low volume machining operations – mostly performed by CNC mills and lathes. A production version would ideally be cast and only post-machined where necessary. This would alter the housing design drastically and the INSTAR team is currently investigating the full design impact of the shift to higher volume manufacturing processes and how they affect the overall flywheel design.

Material selection is driven by the three main design requirements, plus weight and volume considerations in order to maintain a high energy density [kJ/kg and kJ/m^3], machinability, and cost. This will be specifically discussed for each major component.

The entire housing is mounted to the vehicle through vibration-isolating rubber mounts. This decouples the flywheel energy storage system's natural frequency from the vehicle chassis, but is unlikely to serve as a permanent solution during vehicle operation. The INSTAR lab is currently investigating the loading due to road conditions and the vibrations encountered during driving.

Figure III-21 INSTAR Flywheel Installed on Test Vehicle

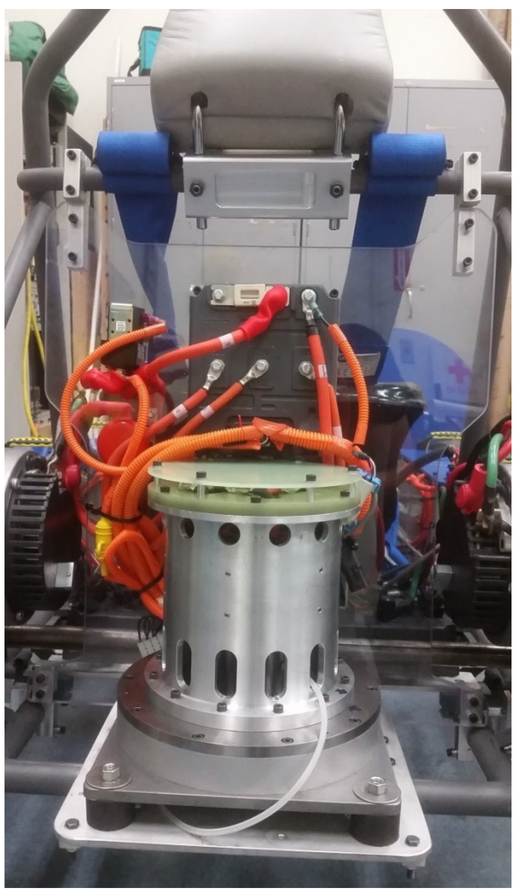

(i) Spindle Alignment

The bearings are seated against 4340 steel housings as aluminum does not have the necessary hardness to resist the forces the bearings will feel during operation and also to match the coefficient of thermal expansion of the bearing races. Ideally the bearings sit in the same bore to ensure proper alignment, but this is not possible with the bearings sitting on opposite sides of the disk. Therefore, the two housing pieces supporting the bearings must have their inner diameters bored together while assembled with the housing enclosure surrounding the flywheel that sits between the two bearing support pieces. This side piece is originally machined to its final dimensions, minus alignment pins (see Figure III-22), while each of the bearing support pieces were first machined to their final dimensions, minus the inner bore and alignment pins (see Figure III-23 and Figure III-24). These three pieces also have 3 steel alignment pins per side drilled and placed while assembled together to ensure this alignment is repeatable even after multiple disassembly and reassembly operations (see Figure III-25). The pins are designed to be asymmetrical to ensure that the pieces can only fit in a single orientation (poka-yoke).

Figure III-22 Housing Side Enclosure Pre-Final Machining Drawing

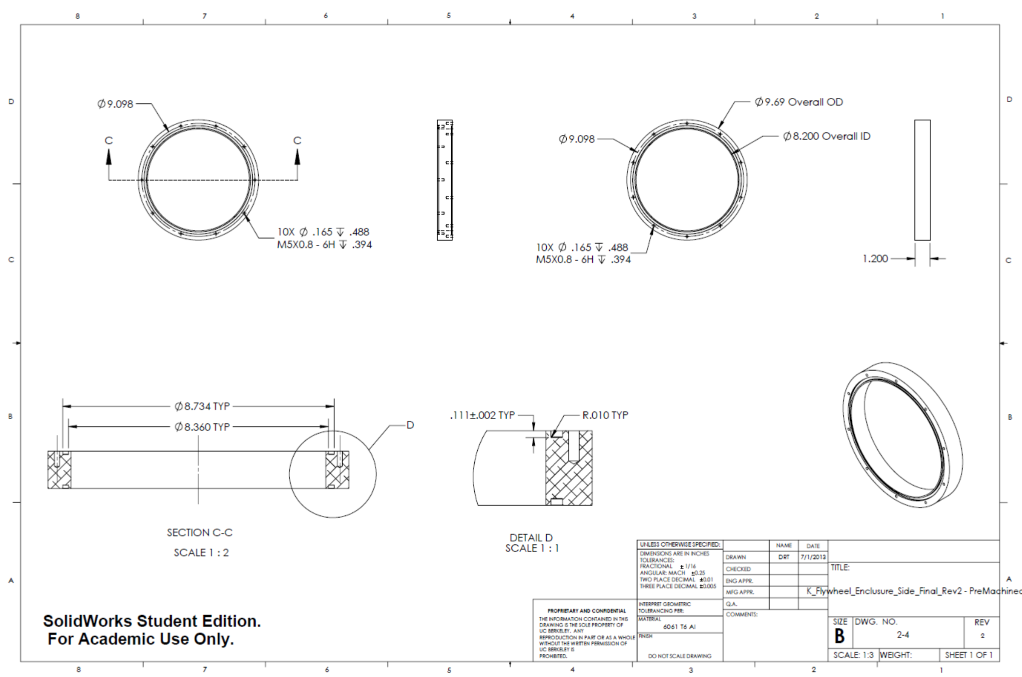

Figure III-23 Housing Bottom Enclosure Pre-Final Machining Drawing

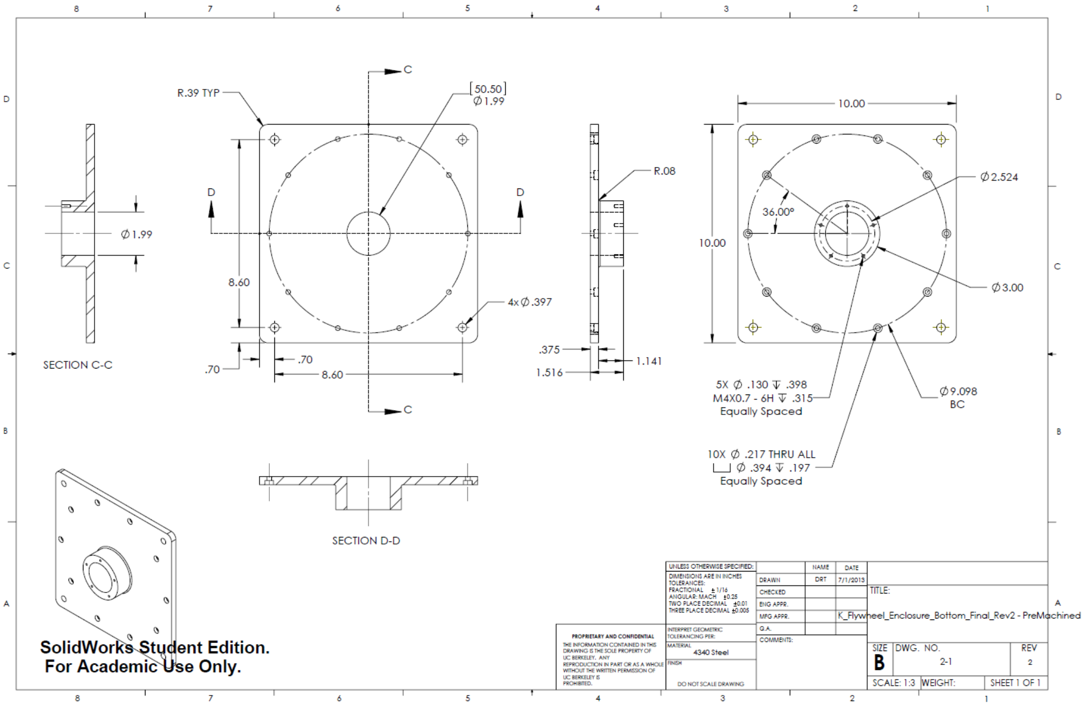

Figure III-24 Housing Top Enclosure Pre-Final Machining Drawing

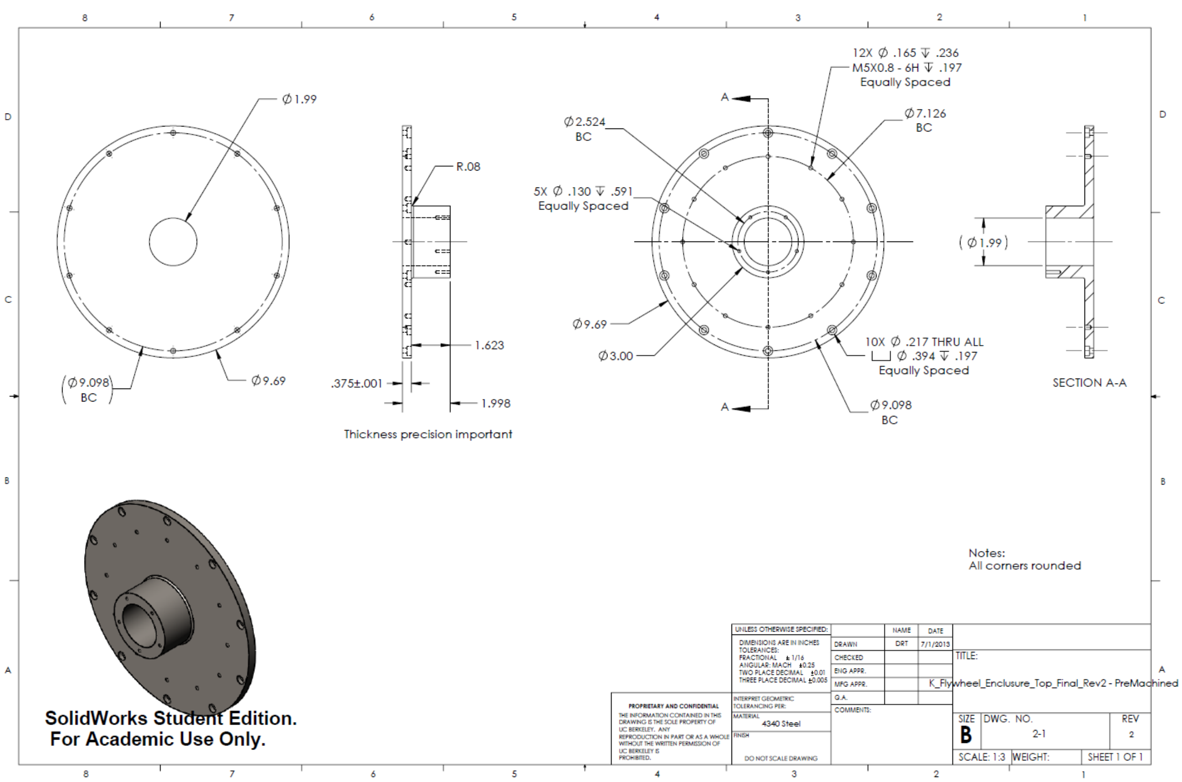

Figure III-25 Housing Assembled for Final Machining Drawing

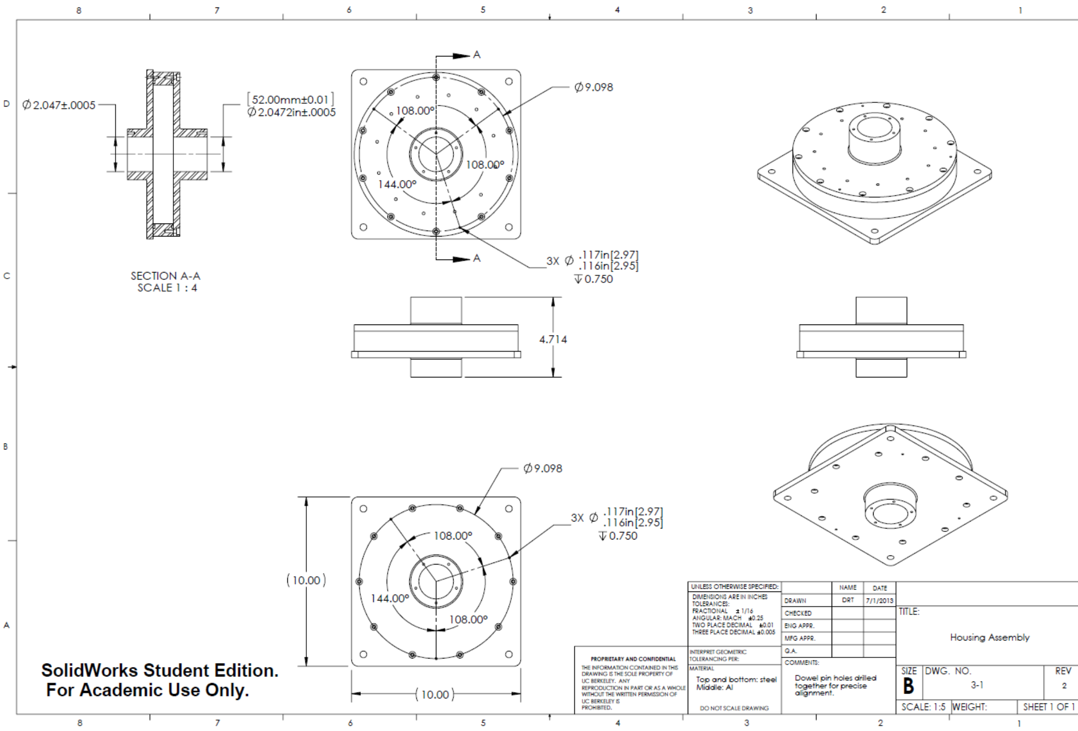

Figure III-26 Housing Bottom Enclosure Post-Final Machining Drawing

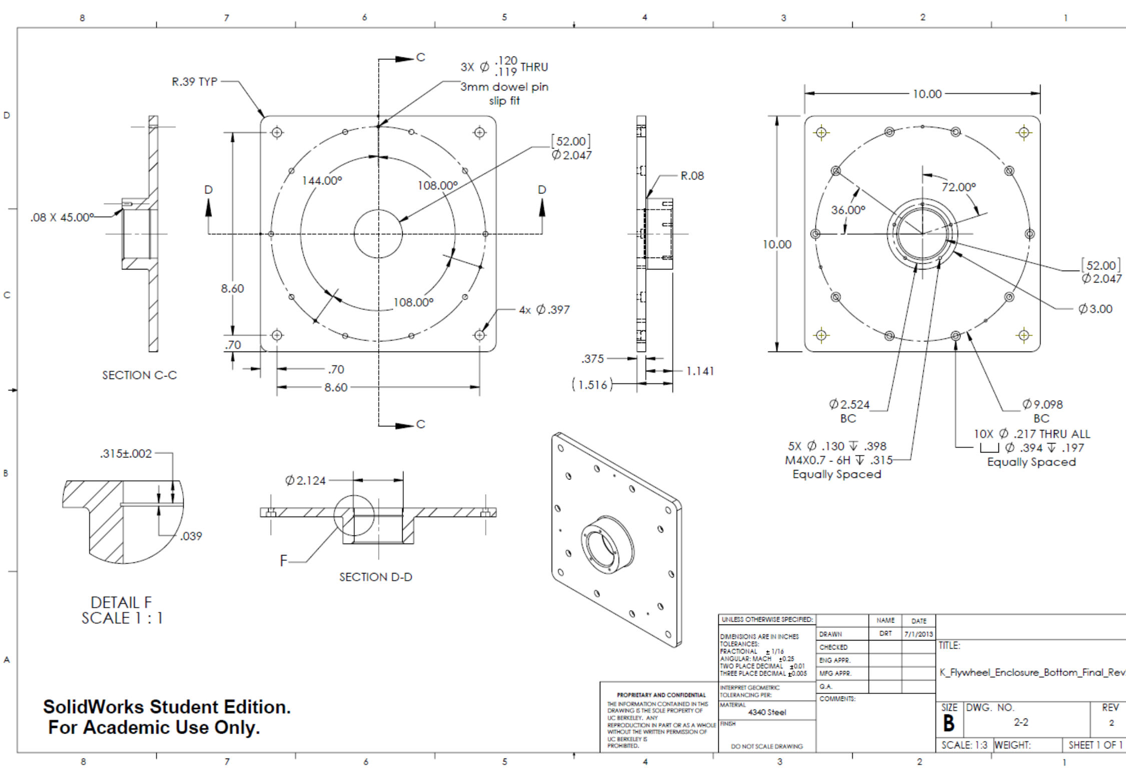

Figure III-27 Housing Side Enclosure Post-Final Machining Drawing

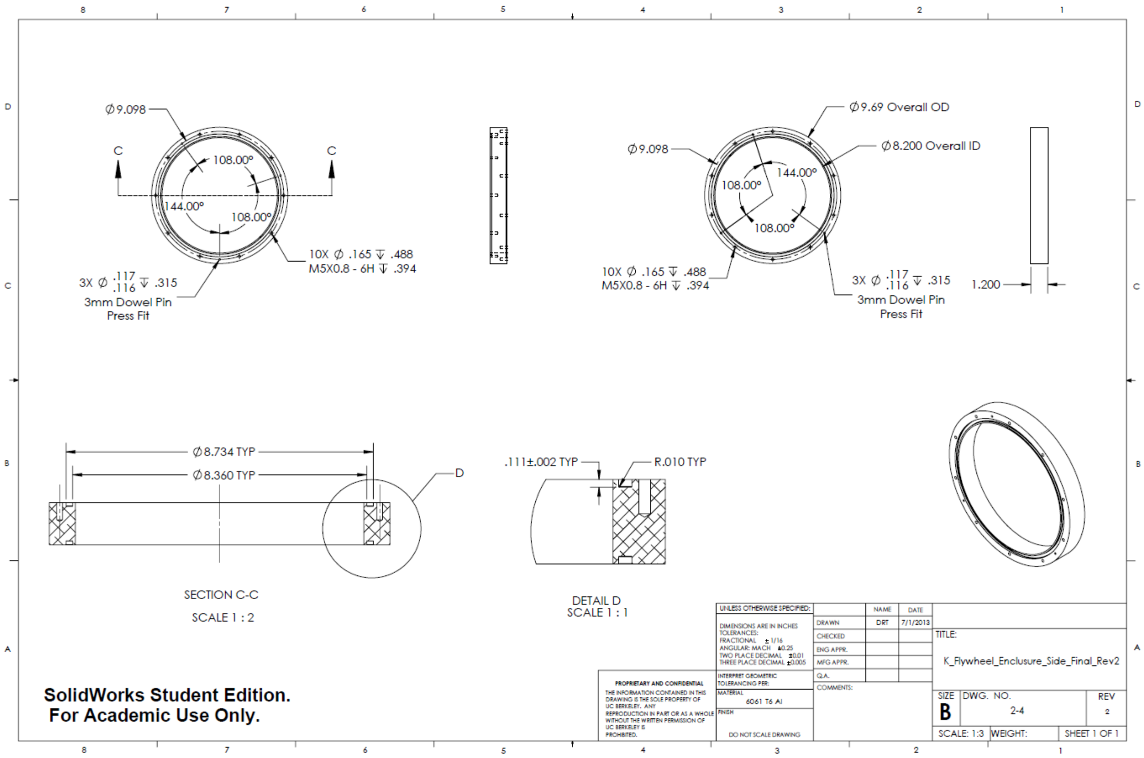

Figure III-28 Housing Top Enclosure Post-Final Machining Drawing

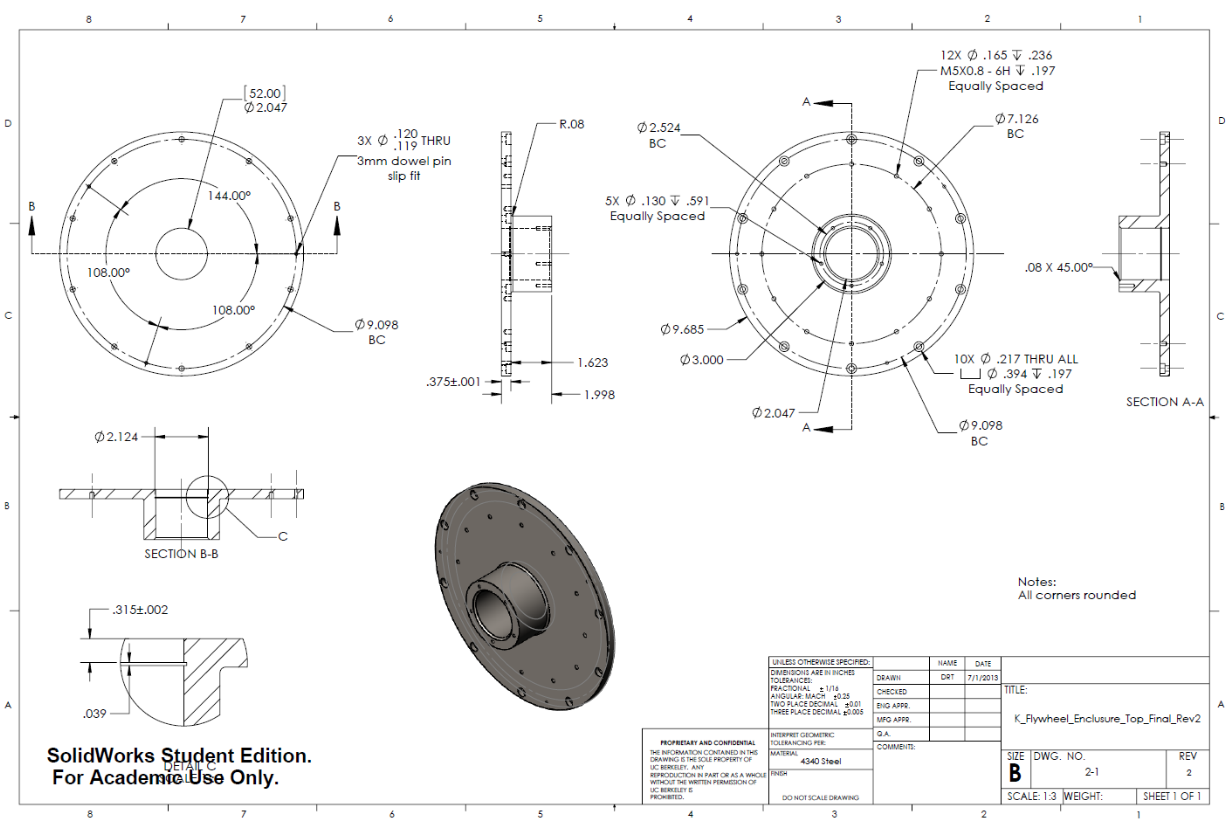

The bottom housing cap bolts on to the bottom bearing housing support piece (see Figure III-29). This cap supports the bottom bearing, and hence the total weight of the spindle. Future iterations on the cap will change the material to steel in order to provide a harder support that will resist deformation under axial thrust loading that will be encountered while the vehicle is driving. This bottom cap also serves as a recirculating oil collection surface and is outfitted with a hose fitting for the oil return. The top cap (see Figure III-30) is bolted on to the top bearing support piece and provides the downward preload, through the wave spring, to the top bearing OD. This piece has a hole in the center for the spindle shaft that protrudes from the housing and into the motor stator.

Figure III-29 Housing Bottom Cap Drawing

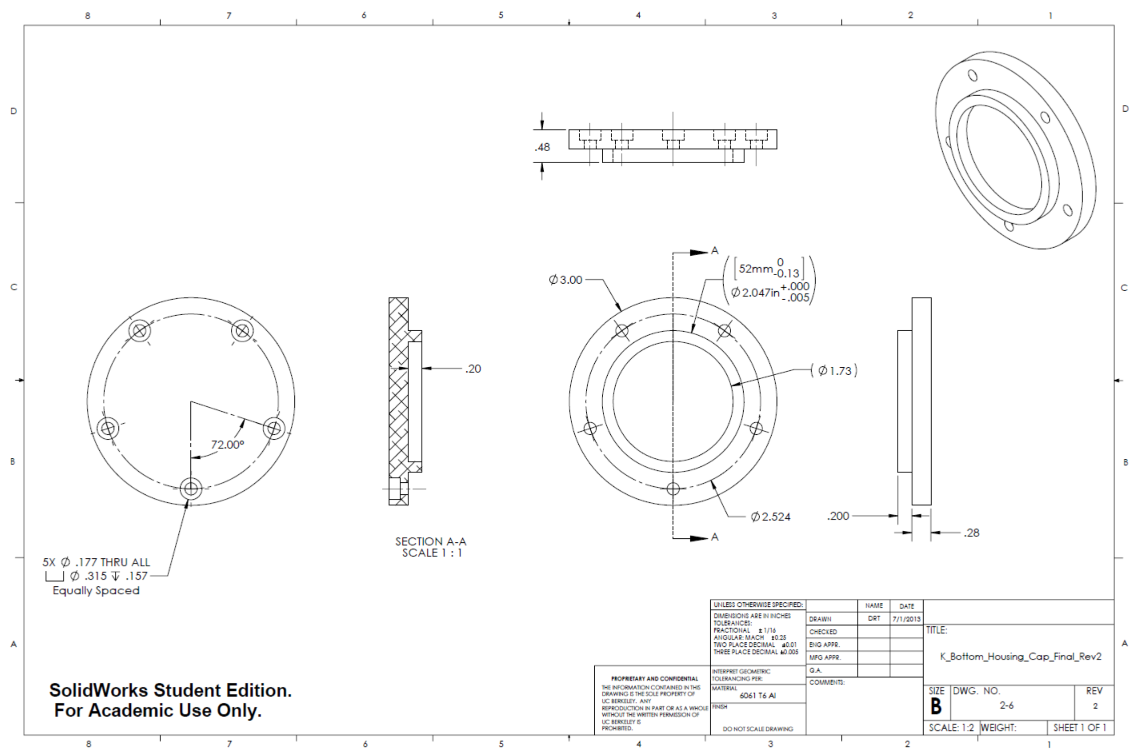

Figure III-30 Housing Top Cap Drawing

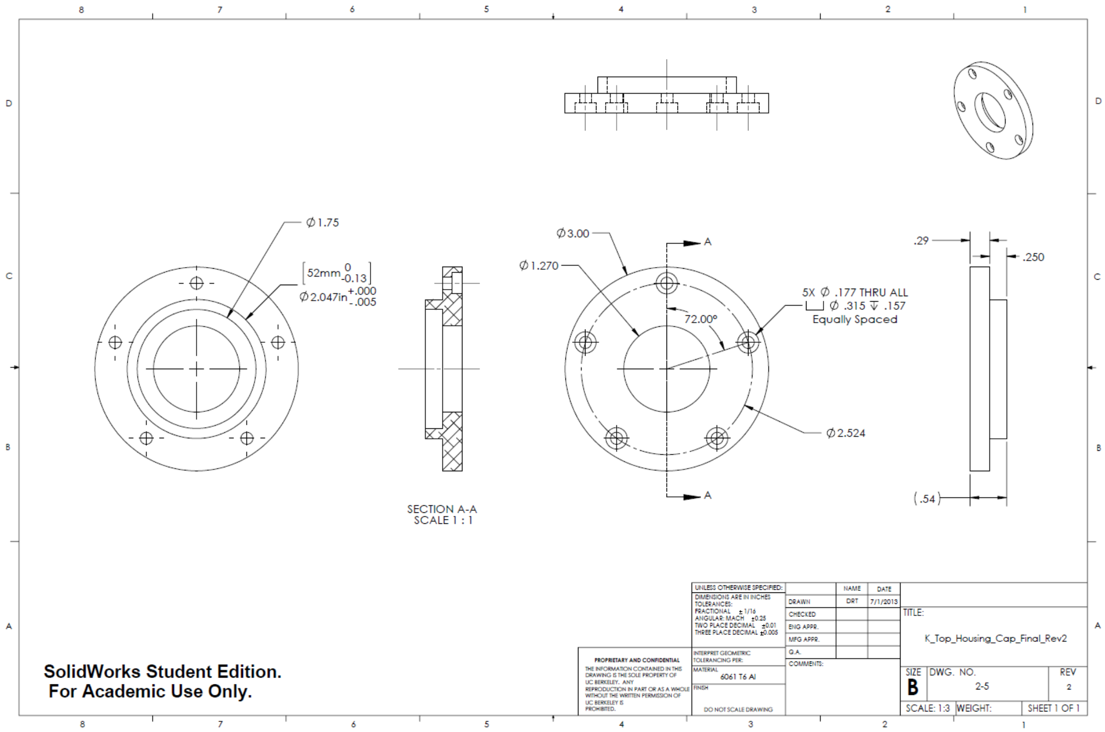

(ii) Vacuum Sealing

The housing retains the vacuum around the flywheel through static O-ring face seals. Grooves are machined into both sides of the housing side piece that immediately surrounds the flywheel disk (see Figure III-27). The O-rings are compressed by the two bearing support pieces during assembly. The shaft vacuum sealing is performed by PTFE lip seals, with the design discussed in detail in Section 3.02(a)(iii), and the testing of the seals discussed in Chapter IV.

(iii) Burst Containment

The INSTAR flywheel housing must also serve as a safety enclosure in addition to all previously mentioned design goals. Indeed, safety is of paramount importance in any design in any field, but especially so in vehicular applications due to the sheer number of potential system implementations and the close proximity to passengers and bystanders. It would be unethical to advocate for the use of this type of energy storage system without demonstrable proof that the inherent safety risks can be overcome. It must be noted, however, that internal combustion engines already make use of solid metal flywheels to smooth out engine operation. These flywheels have a demonstrated safety record and many systems serve as precedent to highlight the potential for safe implementations, even in vehicles. Other researchers working specifically on flywheel energy storage systems for vehicles have also successfully engineered safe designs. According to a 2011 Oak Ridge National Laboratory assessment of the use of flywheel energy storage in vehicles [12]:

A Flybrid flywheel, designed for a race car, was tested at >20g deceleration in a Formula One crash test facility while spinning at full speed (64,500 rpm). The flywheel was undamaged and still spinning after the test.

With that said, the safety concerns surrounding flywheel energy storage use in vehicles are completely valid and cannot be underestimated. It is because many of the researchers in this field accept the responsibility of designing safe systems that multiple resources exist on the safety of flywheel energy storages and how to design such systems to minimize the risks associated with their use.

While some have attempted to fully contain the flywheel in the event of a catastrophic burst and provide design resources to guide this strategy [18] [21] [23], there are also advocates for another approach. A Partnership for a New Generation of Vehicles (PNGV) hearing report [24] contains the following quotes discussing flywheel energy storage safety:

• "With respect to safety, it is not clear that a satisfactory solution has been found to the problem of burst containment. It may be that avoidance of catastrophic burst – rather than burst containment – is necessary for industry and public acceptance." (p. 235)

• "From both a customer acceptance and a product liability standpoint, it may be necessary for vehicle manufacturers to make flywheels "fracture proof," that is, to eliminate the possibility they could come apart in a catastrophic fashion." (p. 273)

A 2011 Oak Ridge National Laboratory [12] report provides the following guidelines to aid designers of flywheel energy storage systems:

- Intentionally avoid the ultimate stress with a significant safety margin
- Design a rotor that fails incrementally and design the containment for the smaller burst event
- Instrument the rotor to predict failure before it occurs
- Design flywheel-specific containment as in the UT Austin design [23] employing a rotatable liner to prolong the burst event time and dissipate the energy at a resulting lower power

The report elaborates specifically on the first point, pointing to an ANSI/AIAA flywheel rotor safety standard developed by NASA and the Air Force [25] that requires rotor assemblies for space systems to include a sufficient safety margin that does not necessitate a containment system. This is verified by running a test with the flywheel operating at 1.225 times the maximum expected operating speed for a minimum of five minutes without catastrophic failure. Every rotor that will go into field operation must also pass a series of tests, including a "proof spin test" at 1.1 times the maximum expected operating speed for ten minutes. By calculating the hoop stress described in Equation III-6, 1.225 times the maximum speed is 1.5 times the maximum expected hoop stress and 1.1 times the maximum operating speed is 1.21 times the maximum expected operating hoop stress.

The PNGV report [26] recommends a 4:1 ratio of ultimate strength-to-maximum operating stress ratio to avoid the possibility of catastrophic rotor failure entirely. The Ø8” diameter INSTAR flywheel, operating at its maximum possible testing speed of 18,000 RPM has a factor of safety of 5.3 when compared the yield strength. This is more than sufficient to meet this 4:1 requirement. It is also surrounded by a 0.75” thick aluminum safety ring. The INSTAR lab is currently investigating the design of a composite ring surrounding this aluminum ring for added protection with minimal added weight.

(c) Flywheel Motor

The INSTAR DC brushless motor has been designed to operate at the same voltage as the battery pack at maximum speed (nominally 80v) to eliminate the need for a DC-DC converter and the efficiency loss associated with it. The motor must also be able to handle, at a minimum, the peak current generated by the kart during braking and possibly peak current pulled from the battery during acceleration. This allows for future testing of INSTAR implementations that use the flywheel not just to absorb surge current during braking, but also to deliver surge current during acceleration. From our vehicle testing (see Figure III-31), the kart is able to generate 100 amps during hard braking and pull over 300 amps during hard acceleration. At 80V, this is 8 kW and 24 kW, respectively. A 24kW motor can also be used during braking for much larger vehicles that will be tested in the future.

Figure III-31 Data collected from Go-Kart for Motor Sizing

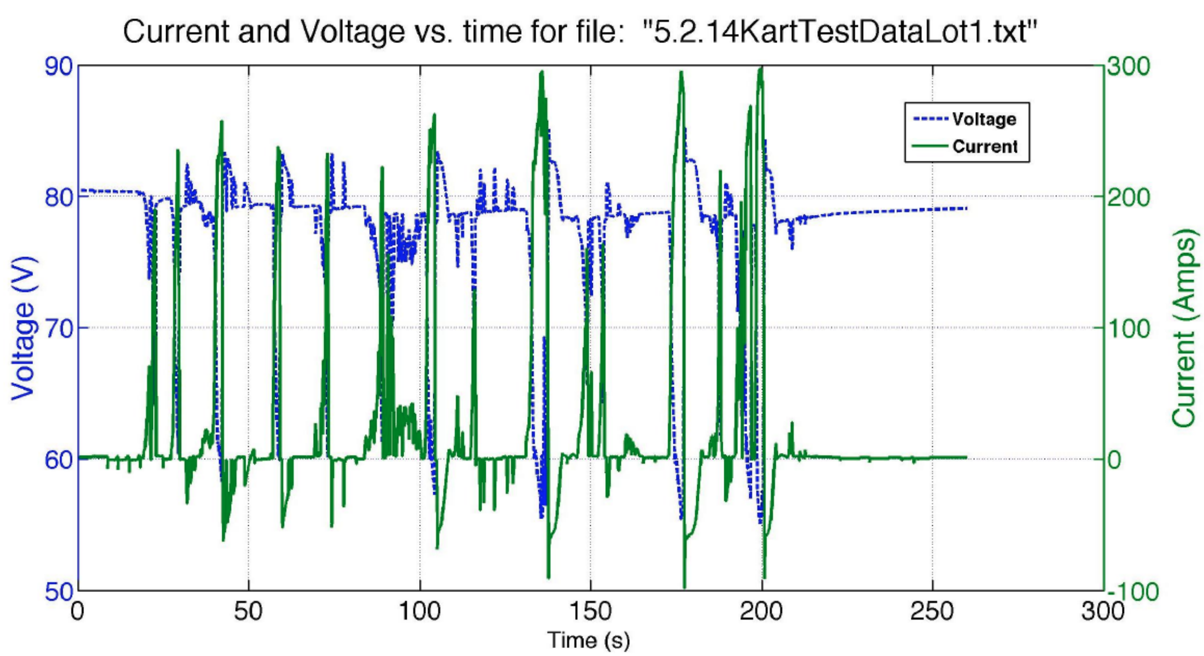

(i) Rotor

The INSTAR DC brushless rotor is a 4 pole permanent magnet rotor using 42 MGOe neodymium magnets. Each magnet was purchased off-the-shelf and manufactured with a curve to fit a Ø2.0” cylinder. A total of eight magnets are required to enclose the rotor and so each pole consists of two magnets of similar polarity arranged right next to each other (see Figure III-32). Each magnet is 1” tall and so the rotor consists of three magnet rings stacked in the same arrangement, 24 total.

Figure III-32 INSTAR Motor Rotor Pole Layout

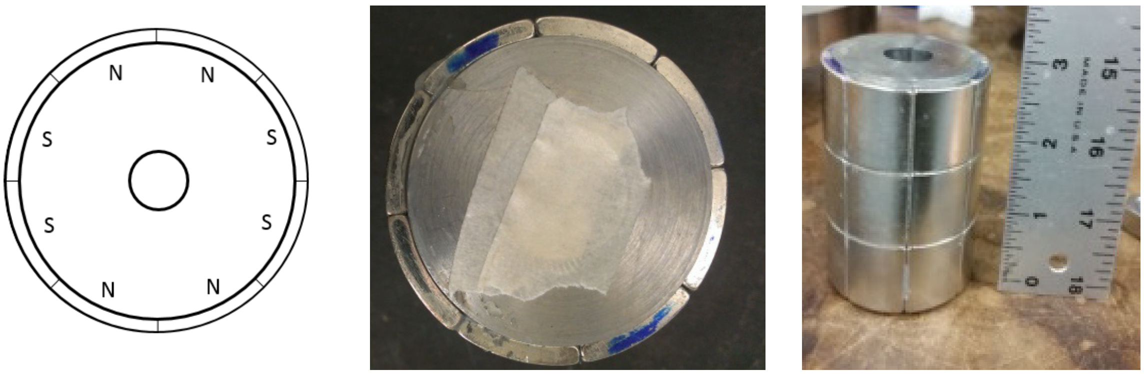

The center of the hub is tapered to match the taper on the flywheel shaft discussed in Section 3.02(a)(iv) (see Figure III-33 and Figure III-34). The length of the rotor allows for 0.100” of magnet to protrude above and below the stator for sensing by the Hall-Effect sensors located just above the stator. The magnets protrude from the bottom not for sensing, but to balance the magnetic forces from the magnets extending out the top of the stator. Extra material is also placed at the top of the rotor to allow the independent balancing shop to remove material without adversely affecting the magnetic saturation limits of the rotor.

Figure III-33 INSTAR Motor Rotor Hub Drawing

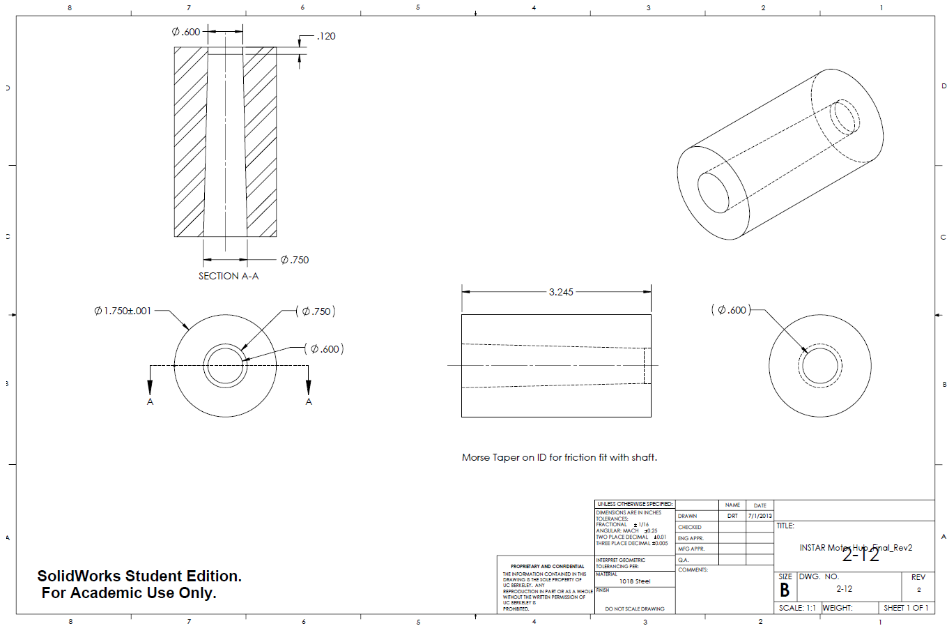

Figure III-34 Assembled INSTAR Rotor and Flywheel Shaft

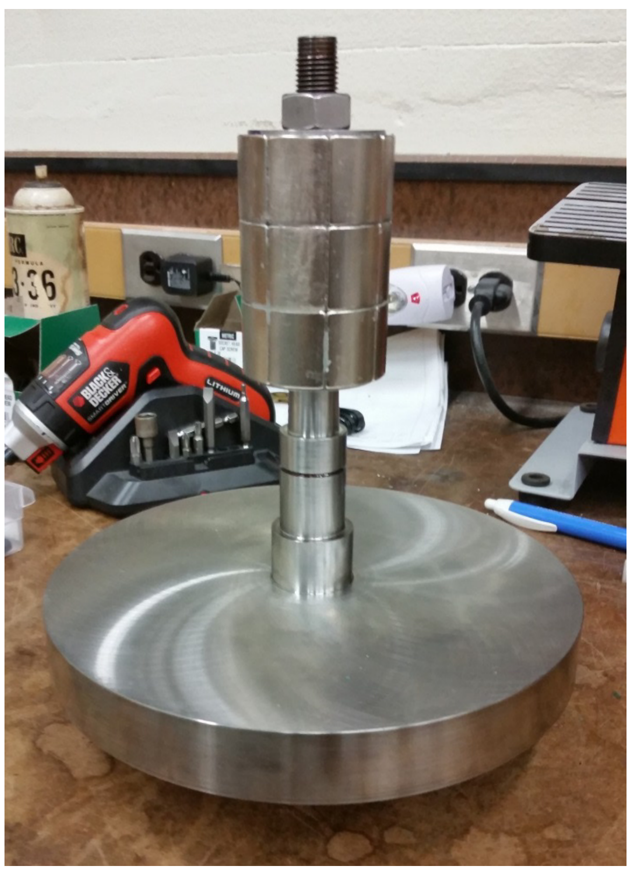

While simple to design and diagram the arrangement, building the rotor required special 3d-printed tooling (see Figure III-35) to keep the magnets pressed against the rotor while the 3M two-part epoxy cured overnight. Prior to applying the epoxy, both the rotor and magnet surfaces were roughened with sand paper to provide additional bonding surface area and cleaned with isopropyl alcohol.

Figure III-35 3D Printed Rotor Assembly Jig

Figure III-36 First Magnet Set with 3D Printed Jig

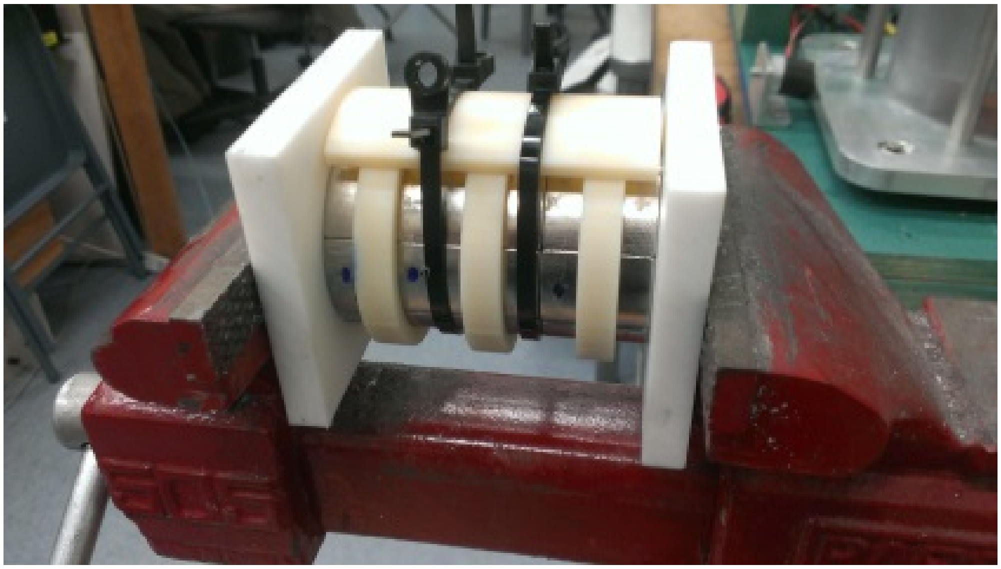

Figure III-37 First Magnet Set after Epoxy Curing

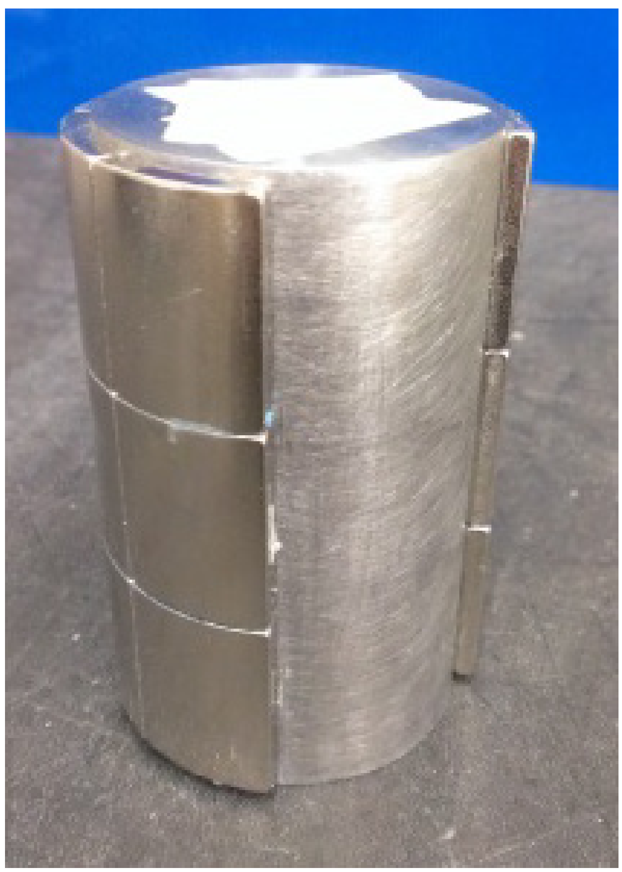

Figure III-38 Rotor Kevlar Wrap in Process

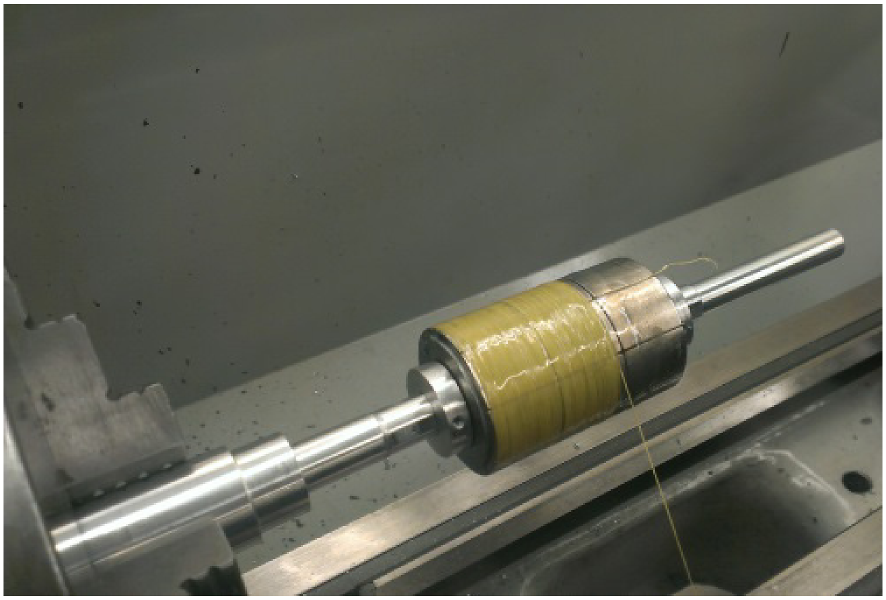

Figure III-39 Finished Rotor After Magnet Epoxy and Kevlar Wrap

Similar polarity magnets repel each other and this arrangement not only has magnets of the same polarity adjacent to each other tangentially, but also directly above and/or below them as well. This causes the magnets to not only separate axially, but also rotate to align with magnets of the opposite polarity. This necessitated bonding six magnets of each eight magnet ring one day (18 total), allowing them to cure (see Figure III-36), and then bonding the remaining two from each ring the following day (6 more total).

As the rotor will spin with the flywheel, the magnets must remain attached to the rotor even at 25,000 RPM. While the epoxy is potentially capable of holding the 35g magnets against the rotor despite the centripetal force flinging them off the outside of the rotor cylinder. The entire rotor assembly is coated in a low viscosity two part epoxy and wrapped by a single continuous Kevlar thread in order to ensure they remain attached at high speed (see Figure III-36 through Figure III-39). The Kevlar is rated to 14 pounds (6.3 kg) of tensile load, which at 25,000 RPM provides a factor of safety of over 40.

(ii) Stator

The INSTAR DC brushless motor stator has six teeth made out of stacked M19 silicon steel laminations. 0.007” thick laminations were chosen to minimize eddy current losses (see Figure III-40). The laminations were cut into squares from a single coiled sheet, adhered together using LOCTITE 3504, and then cut as a stack into shape using a wire EDM. The adhesive and wire EDM work was done by Oriental Motors in Japan. The INSTAR lab is very grateful to Fred Otsuka for his help with this. The gap between the stator and rotor is 0.020” (0.5mm), aligned after the motor and housing are attached.

Figure III-40 Motor Stator Lamination Drawing

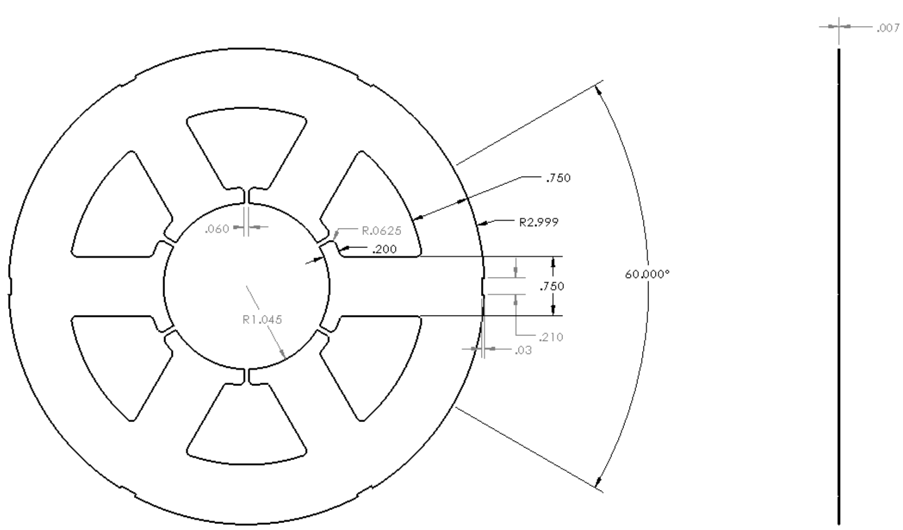

Dimensions in inches

Figure III-41 Motor Stator Manufacturing and Winding

The stack was then painted using an insulating paint to protect it from rust and to insulate each layer from each other by ensuring no conductive path existed between the stator OD and the machined aluminum motor housing ID. Each tooth was covered in a layer of Kapton tape to protect the winding coils from any sharp edges and for another layer of insulation to prevent electrical shorts inside the coils if the wire varnish is compromised.

Each tooth is wound with 8 turns with the equivalent of 8 gauge wire. As actual 8 gauge wire is too stiff to bend around each tooth, 24 gauge magnet wire was coiled and wound around each tooth in three parallel layers with each coil connected to the others at the ring terminals. The first layer consists of a braid of 10 24 gauge wires, wrapped around a single tooth 8 times.

Figure III-42 Winding Coil Braid

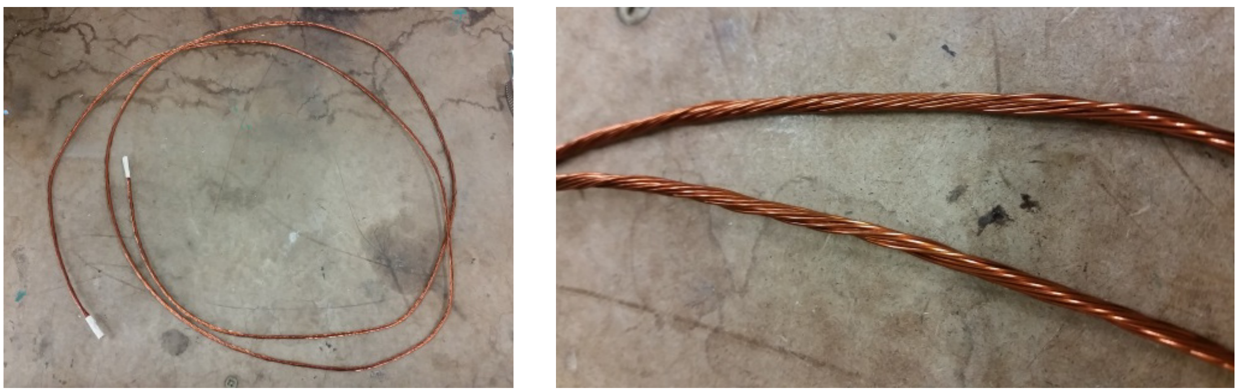

The next layer consists of 11 coiled 24 gauge wires, followed by a final layer of 13 coiled 24 gauge wires. The coils are then stripped at each end, crimped together at each end, and then soldered together at each end to create the parallel connections (see Figure III-41).

Opposite teeth are connected together to create a series Y winding (see Figure III-43). This configuration can be changed in the future without the need to physically rewind the motor. The INSTAR team is also investigating the possibility of using solid state relays to change the motor winding “on-the-fly” through software. This would allow for a dynamic motor constant capable to providing high voltage regenerative braking at low speed.

Figure III-43 INSTAR Motor Before Winding

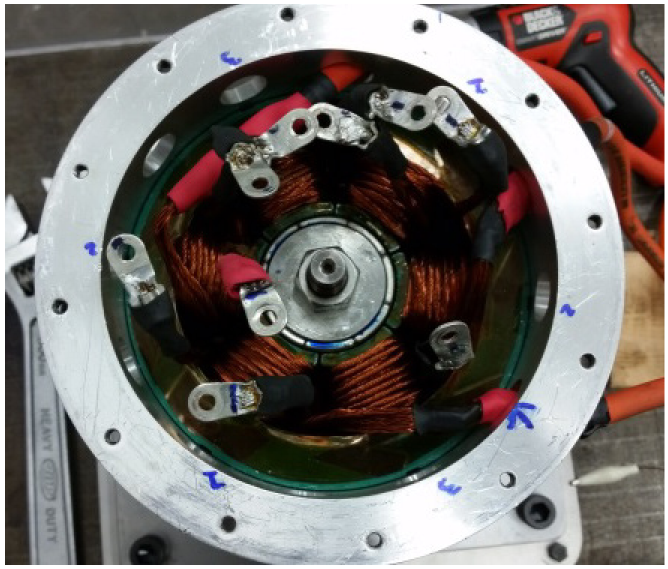

Figure III-44 INSTAR Motor After Winding

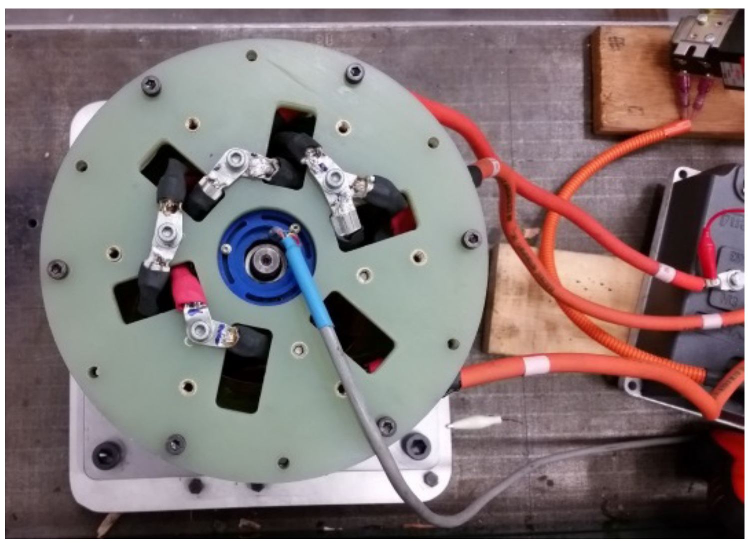

Three Melexis US2882 Hall-Effect sensors are placed 120° apart and directly over the gap in the stator teeth, the zero-crossing point. These feed into the Sevcon Motor controller, discussed in more detail blow, and are used as commutation encoders.

The assembled stator is slipped into the machined aluminum housing and then secured to the flywheel spindle housing with 12 M5 bolts distributed evenly about the circumference. There is enough slop in these bolts to allow the motor to be moved relative to the spindle shaft and the 0.020” gap can be distributed evenly using shim materials.

Figure III-45 Assembled Motor and Flywheel Housing

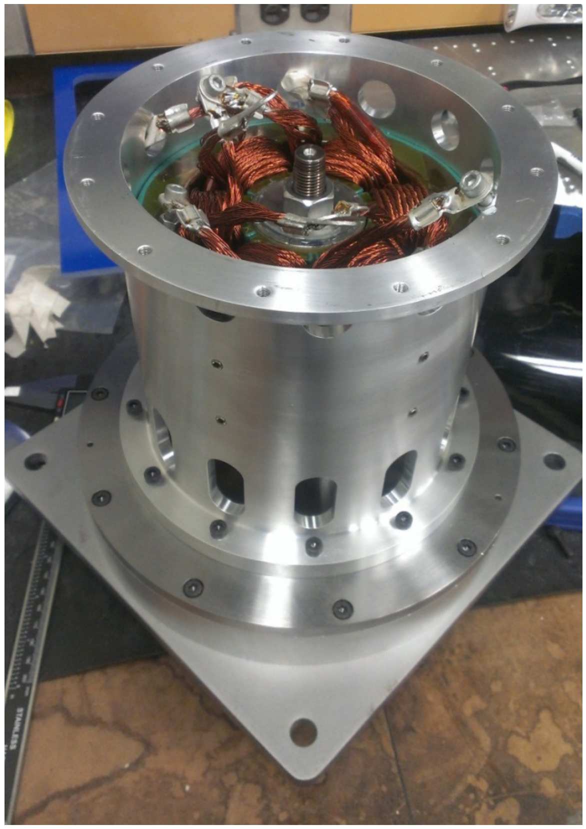

(iii) Motor Controller

The INSTAR flywheel energy storage system uses the same Sevcon Gen4 motor controller to power the flywheel's attached DC brushless motor as it does to power the two brushless DC Mars Motors traction motors. Characterizing the INSTAR motor was aided by Raul Aguilar at ElectricMotorSport in Oakland, CA. This involved tuning the internal Sevcon current control PID coefficients to ensure smooth operation and also installing the Hal-Effect sensors and determining the necessary angular correction to allow for both forwards and backwards operation at full speed.

Figure III-46 INSTAR Flywheel Energy Storage System in Ballistics Testing Chamber

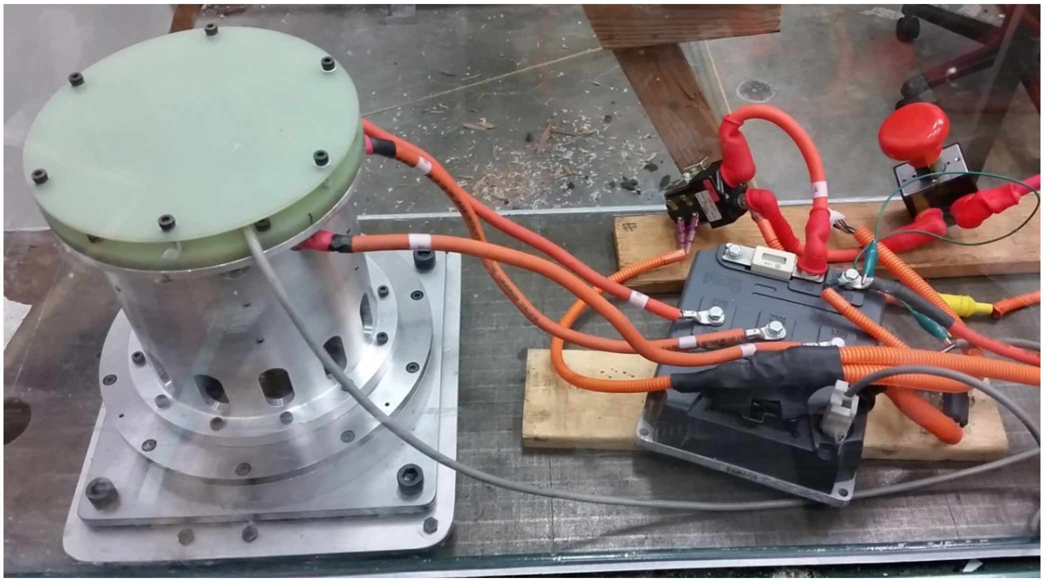

It was during the determination of these characterization constants that the excessive flywheel shaft run-out described in Section 3.02(a)(iv) was discovered. The flywheel was successfully accelerated to 18,000 RPM, demonstrating progress on discovering sufficient tuning coefficients, but was too imbalanced to handle this speed. The cantilevered rotor deflected and touched down on to the motor stator. This immediately cut through the rotor Kevlar and sheared the magnets from the rotor (see Figure III-47). The shredded Kevlar filled the gap and brought the rotor to a stop. The magnets stuck to the ID of the stator and no material was flung from the machine.

Figure III-47 INSTAR Motor After Touchdown Failure

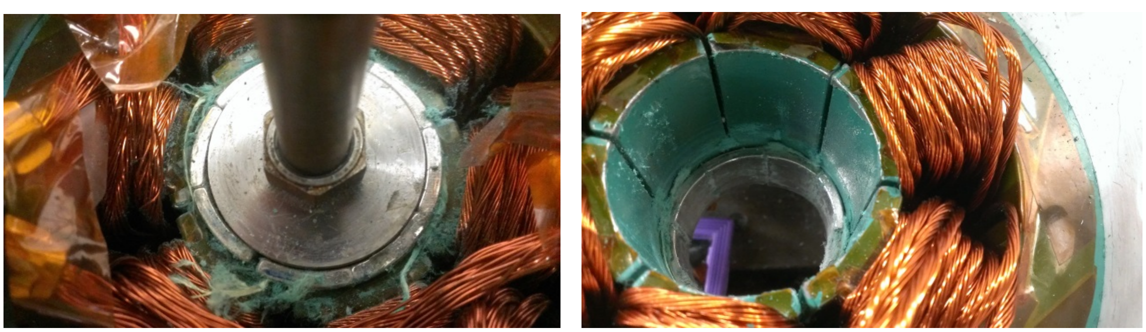

Section 3.03 Closed Loop Controller

One way of describing the main operating principle of the INSTAR system is to use the flywheel to siphon current away from the battery packs during braking. Naturally, a closed loop controller using the current sensor monitoring the current to the battery pack as feedback is a natural choice for an initial flywheel throttle controller when the operating principle is described in this manner. This sensor, with its location labeled in Figure III-48, reads only the net current flowing to the pack based on its location in the wiring of the kart.

Figure III-48 INSTAR Power Flow Diagram

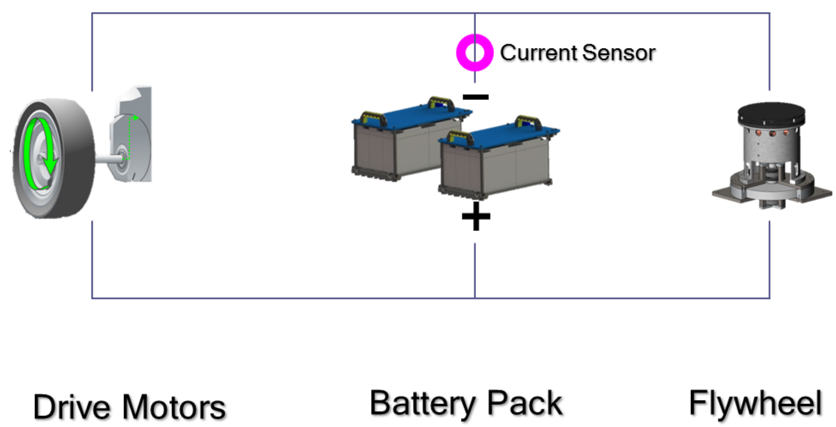

If the flywheel is consuming the exact amount of current that the traction motors are generating during regenerative braking then the battery pack current sensor reads zero amps. If the flywheel is providing the exact amount of current the motors are using to accelerate the vehicle, again, this current sensor reads zero amps. If the vehicle is stationary after a braking event and the flywheel is spinning, storing its absorbed energy, any current it generates during flywheel regenerative braking goes straight to the battery packs and this current sensor reads precisely this value. The main idea is that this simple setup allows for the current sensor to be used as the necessary feedback in a simple, closed loop controller.

This current sensor, more importantly, can be used to not just have the flywheel absorb all the regenerative braking current as just described, but it can be used to have the flywheel absorb a precisely controlled amount that is easily changed. This allows the battery pack to absorb its maximum safe charge current, which varies with both size and battery chemistry, and reduce the necessary size of the flywheel as it needs to store less energy. This is an ideal feature for a future controller as it has many positive benefits on the mechanical design and overall attractiveness of the system, including: lower costs, less mass, and smaller necessary volumes.

An example regenerative braking scenario, with a battery charge limit of 20 Amps (C/2) is shown in Figure III-49. In this scenario, the total current generated by the traction motors during regenerative braking is I_{total} and can be upwards of 100 Amps. Any braking event that generates 20 Amps or less should be completely absorbed by the battery pack. Any event larger than 20 Amps, or even any portion of an event larger than 20 Amps, should activate the flywheel throttle to have the flywheel motor accelerate and draw current away from the battery pack, using it instead to spin up the disk.

Figure III-49 INSTAR Closed Loop Power Flow Diagram

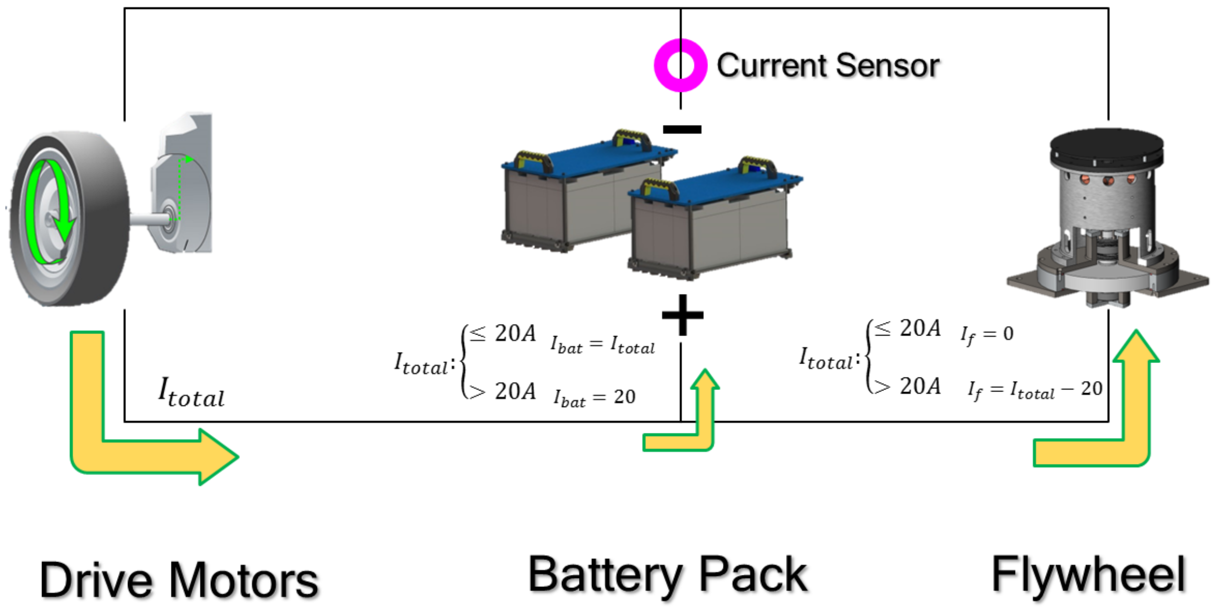

This scenario seems fitting for a simple proportional-integral (PI) controller, using the current sensor to track the controller process variable, $I_{Battery}$. The flywheel throttle is manipulated to have the flywheel motor siphon off any current beyond the 20 Amp set point. The error, here the difference between the current read by the current sensor and the 20 Amp set point, is used to calculate the throttle signal using the standard definition of a PI controller, shown in Equation III-9. This is summarized in Table III-4.

Table III-4 Closed Loop Controller Summary

Manipulated Variable	Flywheel Throttle Signal [0-2559]	Digital CAN signal
Process Variable	Battery Current ($I_{battery}$) [Amps]	Current Sensor
Set Point	20 [Amps]	Controllable
Error	20 - $I_{battery}$ [Amps]	Only when brake signal present

Equation III-9

$$Throttle_{flywheel} = K_p e(t) + K_i \int_0^t e(\tau) d\tau$$

This controller was implemented in LabView and tested on the go-kart test platform, using the setup described in more detail in Chapter V. This test used a zero current set point for initial testing and only calculated the error when the brake pedal read a non-zero signal so as not to confuse the PI controller with the large currents seen during acceleration. This is summarized in Table III-5. A full PID controller, using the differential term, did not seem feasible due to the high-frequency variation in the current sensor signal. While the signal to noise ratio is well above 10, the noise caused the differential term to change sign and destabilize the controller. Including this term was abandoned as it did not appear to be worth the effort.

Table III-5 INSTAR Closed Loop Test Summary

Manipulated Variable	Flywheel Throttle Signal [0-2559]	Digital CAN signal
Process Variable	Battery Current ($I_{battery}$) [Amps]	Current Sensor
Set Point	0 [Amps]	Controllable
Error	(0 - $I_{battery}$) [Amps]	Only when brake signal present

The current for this braking event without the INSTAR system (the control event), is shown in Figure III-50 with a view of both the entire event and a zoomed in picture of just the peak charging current. This control event provides context so the effects of the controller can easily be determined.

Figure III-50 System Current During a Control Braking Event

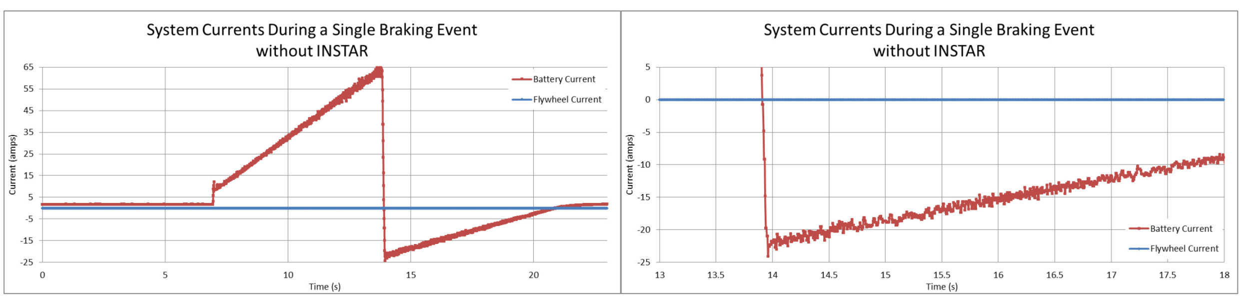

The same braking event, this time with the PI controller enabled and the flywheel allowed to accelerate to bring the current back towards the zero amp set point, is shown in Figure III-52. While the controller was overall able to successfully reduce the error by manipulating the flywheel throttle as planned, it was found during testing that the flywheel was too slow to react using this controller. As seen in Figure III-50 at $t \approx 14$ seconds, the current very quickly ramps up to its peak charging current value. This means that the PI error very quickly grows from nothing to its largest value. While this results in a large resultant flywheel throttle signal, the charging current peak fully develops before this throttle signal is both communicated to the flywheel motor controller and enacted by the flywheel motor controller. This time delay is commonly seen with reactive, feedback controllers. A typical (fictional) step-response for a PI controller is shown in Figure III-51 to reinforce this point. It is inherently necessary to wait for an error to develop in order to generate the controller response.

Figure III-51 Example PID Step Response

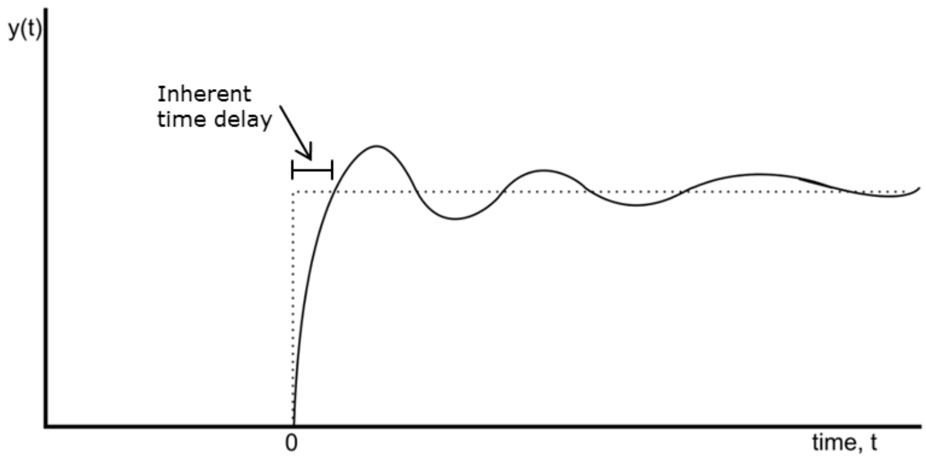

This time delay is essentially intolerable for the INSTAR system. One of the major goals of the system is to have the flywheel siphon current away from the battery pack so that it does not see large charging currents. Since those currents happen at the first initiation of the braking event, the flywheel must be able to react quickly, *before* this peak develops. As seen in Figure III-52, the time delay in the flywheel response allows the maximum value of the battery charge current to remain unaffected. While it stays at, or near, this value for a shorter amount of time, it is still an insufficient controller due to the importance of avoiding this peak battery charging current altogether.

Figure III-52 System Current During Single Braking Event with Closed Loop Controller

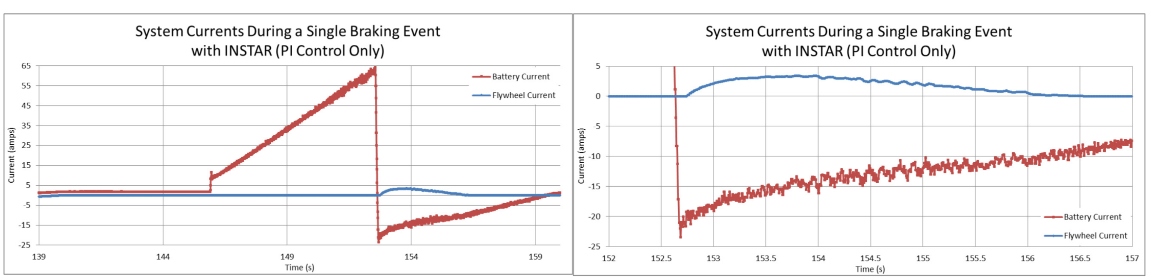

This behavior was seen across a wide range of values of K_p and K_i, even for those large enough to destabilize the system. Many tests were run with various values of $K_p$and K_i and a sample of these data sets is included in Appendix C. The data in Figure III-52 was merely chosen to represent the findings of this controller development process.

This seemingly unavoidable time delay was the motivation for developing the open loop controller described in the next section. It should be noted, however, that this closed loop controller showed promise for keeping the current at a desired level later in the braking event. It seems quite plausible that this controller is implemented as part of a larger, more complex controller that uses a different control method with better response at the initiation of the braking event.

Section 3.04 Open Loop Controller

The design goals of the open loop controller are as follows:

1. The controller must rely solely on information available before the braking event so that the flywheel motor control has enough time to react and absorb the peak regenerative braking charging current with the flywheel rather than with the battery pack

2. The controller should be robust and generalized, capable of maintaining accurate current control over a broad range of vehicle speeds, flywheel speeds, and braking torque requests.

3. The predicted regenerative braking current should accurately match the actual current that the flywheel will need to absorb during regenerative braking

4. The controller must provide an accurate flywheel throttle signal that absorbs precisely the amount of predicted current

It is paramount that it not be limited to the size of the INSTAR test go-kart or require information solely available on the INSTAR test go-kart, but that it can generalized and scaled to a broad range of vehicles in order to encourage its implementation. This section describes both the form of the open loop controller and the system model it is based on so that it can be better translated on to other systems and/or integrated into more complex controllers.

The open loop controller has initially been designed to zero out the charging current to the battery pack during regenerative braking and absorb the entirety of this energy with the flywheel. This is not ideal, nor is it a requirement for the open loop controller to function. The battery pack can, and should, absorb energy to minimize the required flywheel size and speed. It is possible to include this in the controller algorithm and should be included in future iterations. However, this scenario serves as a good starting point for the development of an

INSTAR controller capable of protecting the chemical battery pack from high charging currents. With this in mind, the governing equation for the initial open loop controller during regenerative braking is:

Equation III-10

$$I_{Vehicle,Regen} = I_{Flywheel,Absorbed}$$

During regenerative braking, both sides of the system - the current-generating vehicle traction motors and the current-absorbing flywheel motor - can simply be thought of as electric motors with attached inertial masses. The behavior for this type of simplified system is both well-understood and straightforward. This system model can be used to predict how much current will be generated by the wheels during a braking event and also what throttle signal the flywheel needs in order to absorb just that same amount. Due to its simplicity, the controller can be run in real-time on the go-kart cRIO processor, or any other comparable embedded processor, of which there are many.

(a) Current Generated during Regenerative Braking:

The controller uses two values – the brake pedal position and the wheel speed - to calculate how much current will be generate during regenerative braking. Both of these are read in real-time.

The brake pedal position is used since this signal eventually becomes the requested braking torque. It is available in all vehicles and, more importantly, it is available *before* the charging current develops and is sent to the battery pack. This is *the* major benefit of the open loop controller compared to the PI, closed loop controller that required the charging current to already be flowing before the flywheel throttle signal could be calculated, transmitted, and employed. Using the brake pedal signal means that the current calculated by this controller is a *prediction*, as the current has not been generated by the traction motors yet. This fulfills design goal #1 (prediction).

There is a major contribution to the overall current used/generated by the motor from the fact that the wheels are spinning. The applied torque is not being used to keep the wheels in place, where power would remain constant, but is used to accelerate them. This acceleration requires more power at higher speeds. Determining how much more current is required at higher speeds can be determined by modeling the system using conservation of energy and power.

Beginning with the kinetic energy of the wheels, where the wheel moment of inertia J includes the vehicle and driver inertial contributions:

Equation III-11

$$E = \frac{1}{2} J \cdot \omega^2$$

$$Power = \frac{dE}{dt} = J \cdot \omega \cdot \frac{d\omega}{dt} = J \cdot \omega \cdot \alpha$$

$$Torque = J \cdot \alpha$$

$$Power = \omega \cdot Torque$$

$$Power = I \cdot V$$

Equation III-12

$$\therefore \omega \cdot Torque = I \cdot V$$

Equation III-13

$$\therefore I = I_{rotational} = \frac{\omega \cdot Torque}{V}$$

Substituting $\qquad A = \frac{1}{V}$

Equation III-14

$$I_{rotational} = A \cdot (\omega \cdot Torque)$$

Equation III-11 shows that higher speeds result in the vehicle needing to absorb higher power levels. In regenerative braking $\propto \omega_{wheel}$, as the gear ratio must be taken into account, and higher vehicle speeds will result in higher regenerative braking current that the battery pack and/or flywheel will need to absorb. $I_{rotational}$ is inversely proportional to the voltage, which does vary over time. However, for the purposes of this initial implementation it was kept constant at the nominal 80V battery pack voltage as it is generally between 70 and 84 volts during testing.

In a DC brushless motor, the braking torque provided by the motor is linearly proportional to the current that will be generated using the torque constant of the motor ($K_t \ in \ \left[\frac{N \cdot m}{Amp}\right]$).

Equation III-15

$$I_{torque} = \frac{Torque\ Requested}{K_t}$$

Higher torque requests provided proportionally *less* current to the batteries during braking due to conductive losses. The higher current generated by the higher torques resulted in larger currents circulating in the motor windings. Since the dissipated power is proportional to the current, it is also proportional to the torque request.

$$P_{resistive} = I_{torque}^2 \cdot R$$

$$P_{resistive} = \left(\frac{Torque\ Requested}{K_t}\right)^2 \cdot R$$

This power is subtracted from the power that needs to be dissipated from the wheels during braking. The net result is that proportionally less current ends up charging the battery pack and this term becomes negative in the overall controller algorithm. While it is proportional to the square of the requested torque, this term is smaller than the contribution from $I_{rotational}$and a simple linear relationship still provided an accurate prediction of the overall current generation.

Equation III-16

$$\therefore I_{torque} = -B \cdot Torque\ Requested$$

The last contributor to the open loop controller's current generation prediction deals with the INSTAR motor efficiency. The motor controllers are a torque-based system, focused on controlling the current draw and current generation required to match the torque levels requested by the vehicle driver. The motor controllers are not directly concerned with how much current is drawn from the battery packs, but how much is actually flowing through the motor windings. The INSTAR controller, however, is directly concerned with how much current the motor controllers are pulling from the battery pack rather than flowing through the windings. The reason these two are not identical is because electric motors, like any other system, are not 100% efficient at converting energy from one form to another.

$Power_{electrical,in}$: $Power_{mechanical,out}$	during acceleration
$Power_{electrical,out}$: $Power_{mechanical,in}$	during regenerative braking

The DC brushless traction motors and DC brushless flywheel motor all exhibit motor efficiency that increases with speed. At low speeds, less energy is converted into useful energy, which is true in both energy flow direction. The efficiency during regenerative braking is seen in Figure III-53.

Figure III-53 INSTAR Motor Efficiency During Regenerative Braking

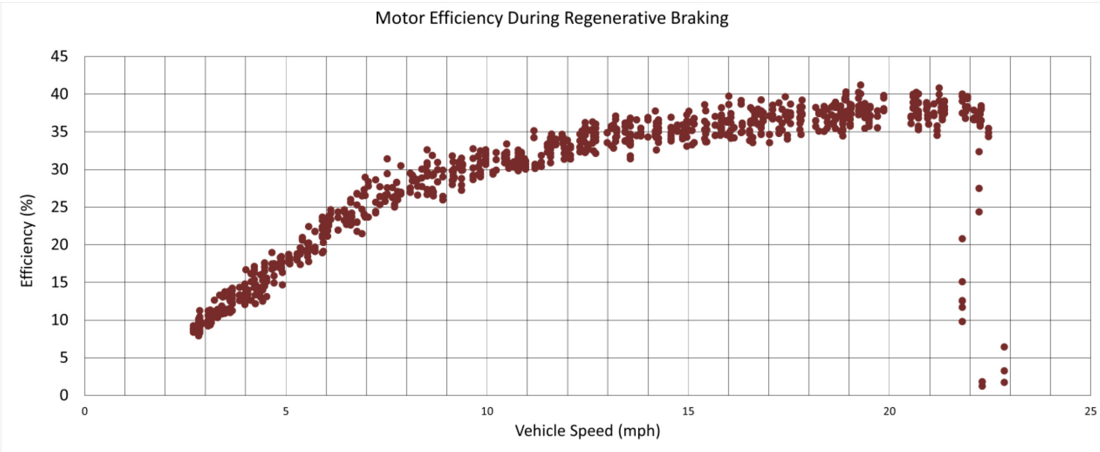

While motors are essentially energy conversion machines and are better analyzed using energy and power balances, this efficiency concept can still be thought of in terms of current. The motor needs to supply $[I_{rotational} + I_{torque}]$ *after* the efficiency loss is taken into account as it is this net current that provides the torque that the motor controller is supplying. The INSTAR open loop controller compensates for this efficiency loss by adding an additional term to include this dissipated current that the battery pack or motor still provided (depending on power flow direction), but was never turned into useful work to turn the wheels or charge the battery. This extra current contribution decreases with speed as the motor becomes more efficient and less is lost. During regenerative braking, this results in more current being available to recharge the battery so the sign on this term is positive.

Equation III-17

$$I_{efficiency\ loss} = C \cdot \omega_{wheel}$$

Combining each of these three discussed contributing factors results in Equation III-18.

Equation III-18

$$I_{vehicle,regen} = I_{rotational} + I_{torque} + I_{efficiency\ loss}$$

Equation III-19

$$I_{vehicle,regen} = A \cdot \left(Torque_{Brake,Requested} \cdot \omega_{wheel}\right) - B \cdot Torque_{Brake,Requested} + C \cdot \omega_{wheel}$$

In theory the battery voltage, torque constant, and speed-efficiency profile should be known and hence A, B, and C should be known. In practice, however, it was found that it was more useful to vary A and B in order to tune the overall controller algorithm to better match the measured current values. These values were tuned using a driving profile tested on the go-kart. The testing setup is discussed in more detail in Chapter V. The main point to emphasize here is that this driving profile was deliberately designed to ensure that the open loop controller performs well over a wide range of braking scenarios and fulfill design goal #2 (robustness).

Figure III-54 displays the vehicle speed and braking signal over the course of the test. Figure III-55 displays the actual current that the battery pack sees during this cycle when the flywheel is disconnected.

Figure III-54 Test Driving Profile

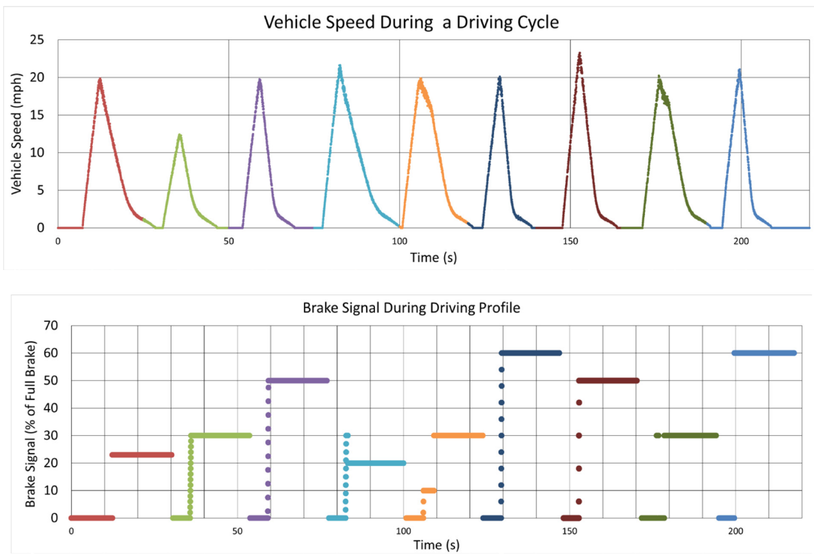

Figure III-55 Battery Current through Driving Profile

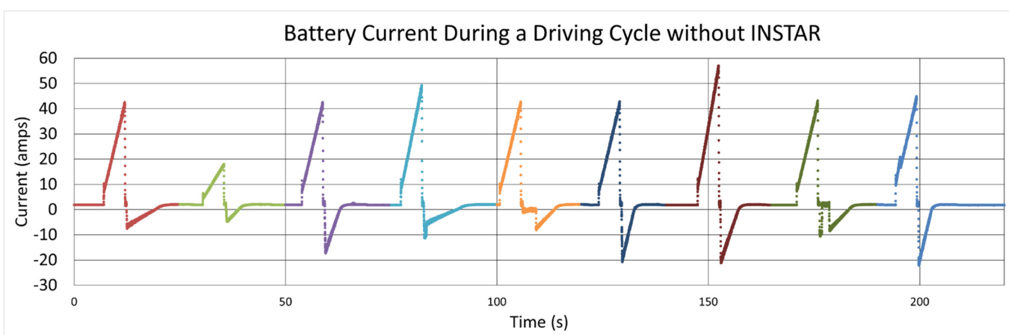

The open loop controller uses the same sensors that collect the data in Figure III-54 and, in real-time, forms its prediction on what current the battery pack will see. The actual current and the predicted current are plotted against each other in Figure III-56. From this graph it should be obvious that the prediction very closely matches the actual current and that it generalizes over all of the braking events quite well. No matter the initial speed nor magnitude of the braking event, the controller is able to generalize the braking event and form an accurate prediction of the regenerative braking current using just the brake signal and the wheel speed. This fulfills design goal #3 (regenerative braking current accuracy).

Figure III-56 Open Loop Predicted Battery Current vs Actual Battery Current

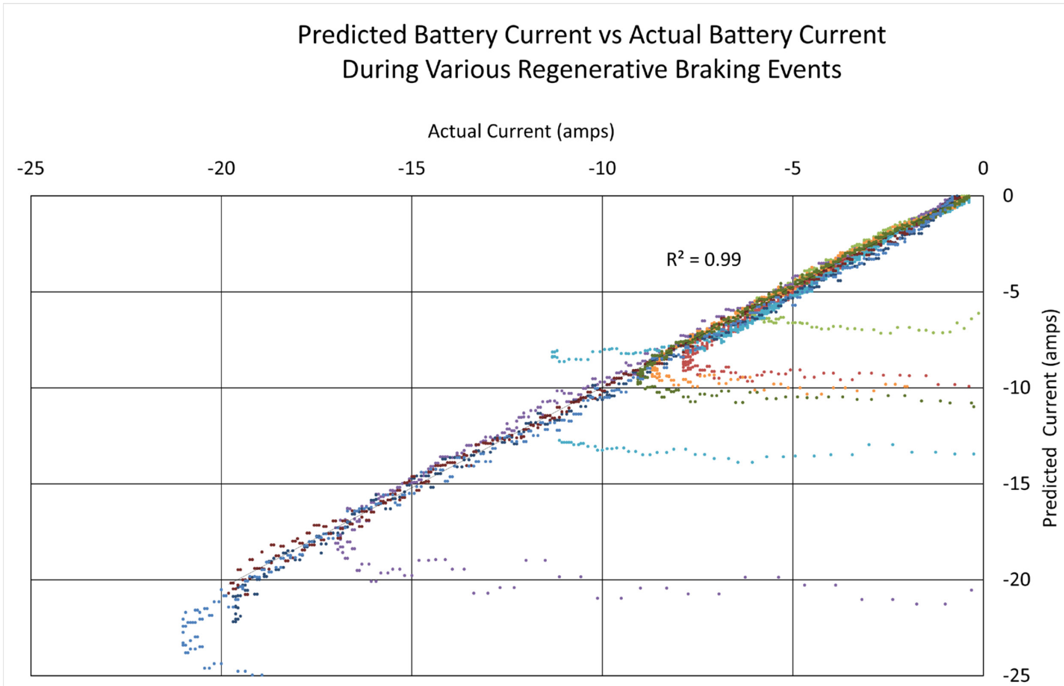

One thing to note is the presence of stray horizontal lines in Figure III-56. These are highlighted in Figure III-57 and are a result of the open loop controller being a prediction. As soon as the braking event is initiated, the open loop controller immediately calculates what current will be generated. However, since it is using the same signal that actually initiates the actual event, this prediction precedes the regenerative braking current. These horizontal lines are from the start of the braking event where the current quickly ramps up to the peak value. These same data points are highlighted in Figure III-58. While it appears that this in an inaccuracy of the open loop controller, and it technically is, this is also a benefit of the controller. It accurately predicts the *end* value of this ramp up, which is the most important value, and has this prediction before the current is actually generated. This allows the flywheel to start absorbing current and reduce the size of the peak charging current seen by the battery pack.

Figure III-57 Examples of Prediction Current Leading Actual Current During Braking

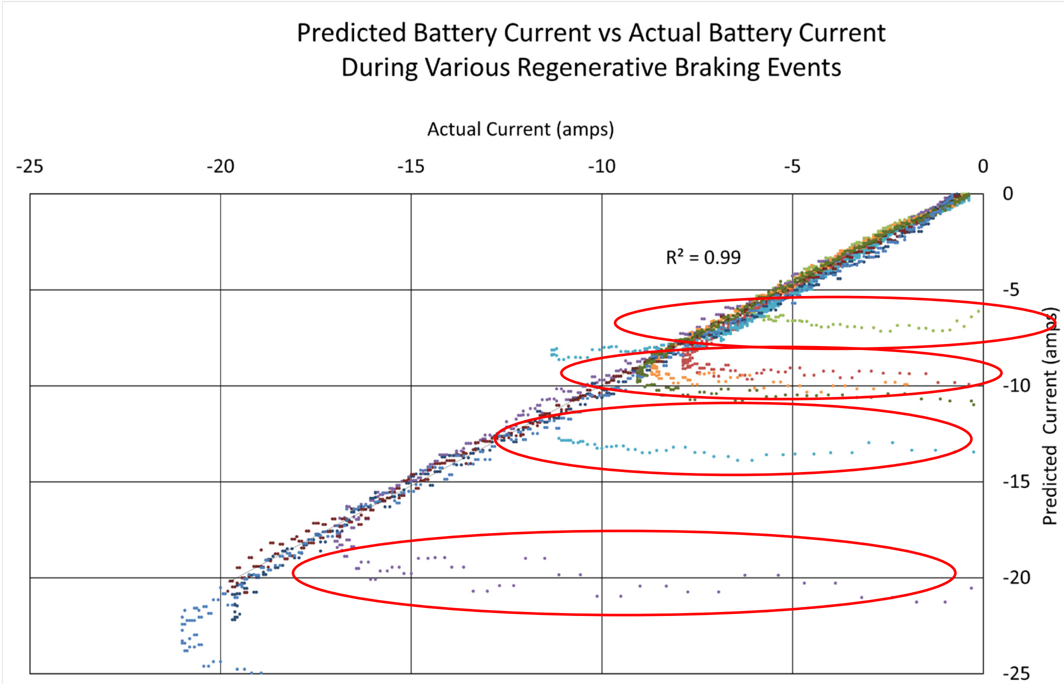

Figure III-58 Examples of Prediction Current Leading Actual Current over Driving Profile

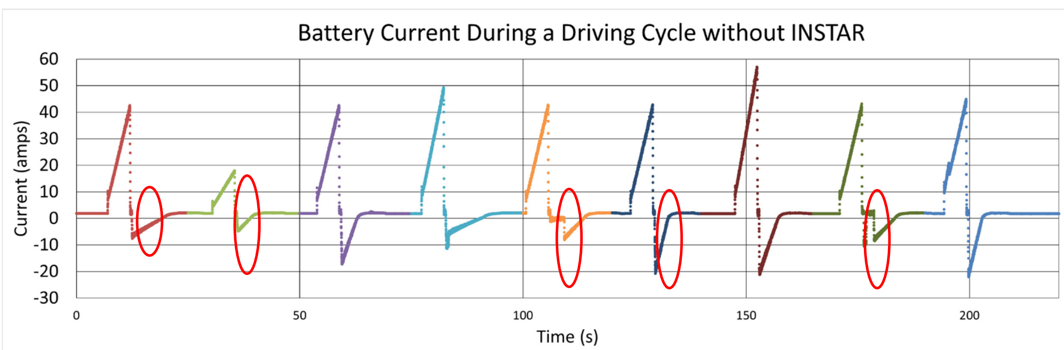

(b) Current Absorbed by the Flywheel:

Much like the accelerator pedals in traditional ICE vehicles, many electric motor controllers are configured to respond to torque commands. It is then necessary for the INSTAR controller to be able to translate the current that the flywheel is required to absorb (in amps) into a CAN throttle signal for the flywheel motor controller (in Newton-meters). This allows the INSTAR controller to essentially operate the motor controller as a current sink or current source. This feature is not only useful for the open loop controller, but can be used with any INSTAR controller that directly calculates the required flywheel absorption current and needs to have it implemented with an off-the-shelf motor controller operating in torque mode. This can potentially negate the need for a custom motor controller and bring down costs.

In order to do this the open loop controller needs to be able to correlate the throttle signal to the precise amount of current that will be used consumed by the motor. This ends up being similar to the current generation prediction during regenerative braking, but with a few key differences due to the reversal in the current flow direction during acceleration when compared to during regenerative braking. Much like in Equation III-18 there are again three main terms.

Equation III-20

$$I_{Flywheel,Absorbed} = I_{rotational} + I_{torque} + I_{efficiency\ loss}$$

Just as with current generation prediction, the $I_{rotational}$term is from the power dissipation during braking and again is linear with both the torque and wheel speed. In this situation, however, it is the acceleration torque rather than the braking torque.

Following the same derivation as for Equation III-14:

Equation III-21

$$I_{rotational} = D \cdot (\omega \cdot Torque)$$

The second contribution, I_{torque}, is from the current required to generate the acceleration torque. In a DC brushless motor, again, the torque provided by the motor is linearly proportional to the current used to generate the magnetic field in the windings that will be generated using the torque constant of the motor ($K_t\ in\ \left[\frac{N \cdot m}{Amp}\right]$).

$$I_{torque} = \frac{Torque\ Requested}{K_t}$$

Substituting $E = \frac{1}{K_t}$

$$I_{torque} = E \cdot Torque\ Requested$$

Just as in the calculation of I_{torque}in $I_{Vehicle,Regen}$ described in Equation III-16, higher torques resulted in higher power losses. The same is true here, except that these extra power losses now contribute to the amount of current that the flywheel siphons off from the battery pack during regenerative braking. While the current is still dissipated and not put to useful work, the sign has changed since it now *adds* to the current that the flywheel absorbs.

Equation III-22

$$\boldsymbol{I_{torque} = E \cdot Torque\ Requested}$$

There is again a current contribution factor from the efficiency of the motor. As Figure III-59 shows, the efficiency again is proportional to the speed and increases with the motor speed until it flattens out around 1200 RPM.

Figure III-59 INSTAR Motor Efficiency During Acceleration

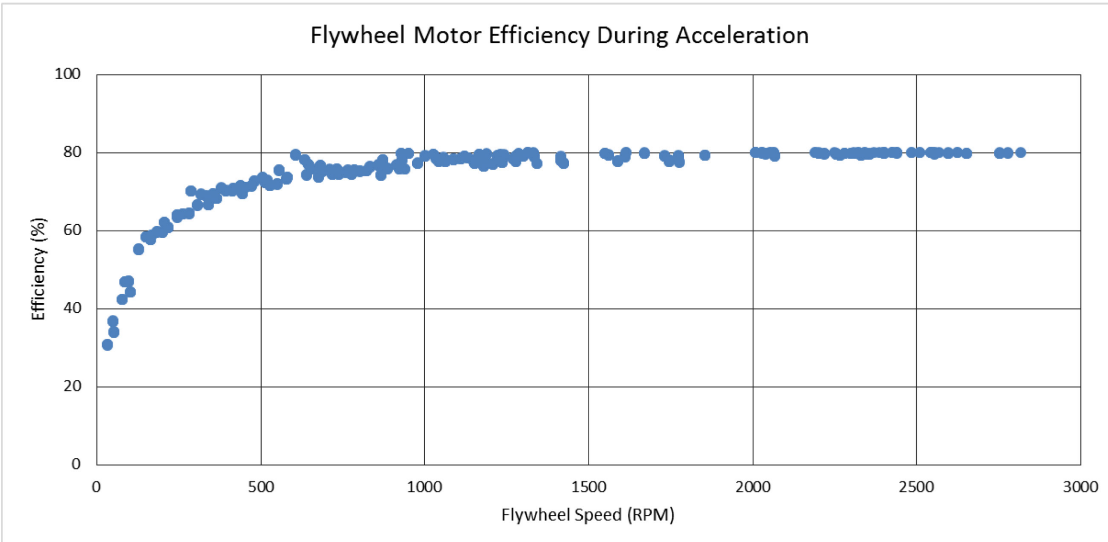

The flywheel is capable of reaching speeds upwards of 10,000 RPM and most braking events put it well beyond 1200 RPM. Therefore, the efficiency lost due to speed, while non-negligent, is constant. It can be taken into account in the other terms and this term does not need to be explicitly included as it does not vary like the other factors.

Combining the two relevant factors results in:

Equation III-23

$$I_{Flywheel,Absorbed} = I_{rotational} + I_{torque}$$

And substituting each part from Equation III-21, Equation III-22, and Equation III-23 results in:

Equation III-24

$$I_{Flywheel,Absorbed} = D \cdot (Torque_{flywheel} \cdot \omega_{flywheel}) + E \cdot Torque_{flywheel}$$

The testing and tuning of these coefficients are discussed in detail in Chapter V.

(c) Controller Algorithm:

Using the governing equation for this controller Equation III-10:

$$I_{Vehicle,Regen} = I_{Flywheel,Absorbed}$$

and combining the derived components from Equation III-19 and Equation III-24 results in the final form of the open loop controller system model:

Equation III-25

$$A \cdot (Torque_{Brake} \cdot \omega_{wheel}) - B \cdot Torque_{Brake} + C \cdot \omega_{wheel} = D \cdot (Torque_{flywheel} \cdot \omega_{flywheel}) + E \cdot Torque_{flywheel}$$

The open loop controller's overarching goal is determine the necessary flywheel throttle signal necessary to absorb the current generated by the vehicle traction motors during regenerative braking. Therefore, the $Torque_{flywheel}$ term in Equation III-25 simply needs to be isolated since this is the value we are looking to communicate to the flywheel motor controller.

Solving for $Torque_{flywheel}$:

$$A \cdot (Torque_{Brake} \cdot \omega_{wheel}) - B \cdot Torque_{Brake} + C \cdot \omega_{wheel} = Torque_{flywheel}[(D \cdot \omega_{flywheel}) + E]$$

Equation III-26

$$Torque_{flywheel} = \frac{A \cdot (Torque_{Brake} \cdot \omega_{wheel}) - B \cdot Torque_{Brake} + C \cdot \omega_{wheel}}{(D \cdot \omega_{flywheel}) + E}$$

It is convenient to add a constant term in front to scale all 5 coefficients at once, and therefore establish the final form of the open loop controller algorithm. This

Equation III-27

$$Flywheel\ Throttle = Torque_{flywheel} = F \cdot \left[\frac{A \cdot (Torque_{Brake} \cdot \omega_{wheel}) - B \cdot Torque_{Brake} + C \cdot \omega_{wheel}}{(D \cdot \omega_{flywheel}) + E}\right]$$

The testing of this finalized form is described in detail in Chapter V.

(d) Other Applications in Future Controllers

While the system model described in the Current Absorbed by the Flywheel section was designed to translate the current that the flywheel needs to absorb into a flywheel throttle signal, it has more potential uses. The most useful might be its ability to be used to predict the current consumed by the traction motors during acceleration. In this scenario the flywheel would be spinning, storing energy it absorbed during braking. This model can be used to determine how much current the traction motors will be consuming and the flywheel can be regeneratively braked to supply this amount of current, plus some extra to recharge the batteries if allowed. It can therefore potentially be used to reduce battery discharge peaks in addition to battery recharge peaks.

In this scenario the efficiency of the motors does not flatten out as quickly as with the flywheel motor and must be explicitly included. Since the efficiency increases with speed, as shown in Figure III-60, the current contribution term is negative as proportionally less current is used at higher speeds.

Figure III-60 Test Vehicle Motor Efficiency During Acceleration

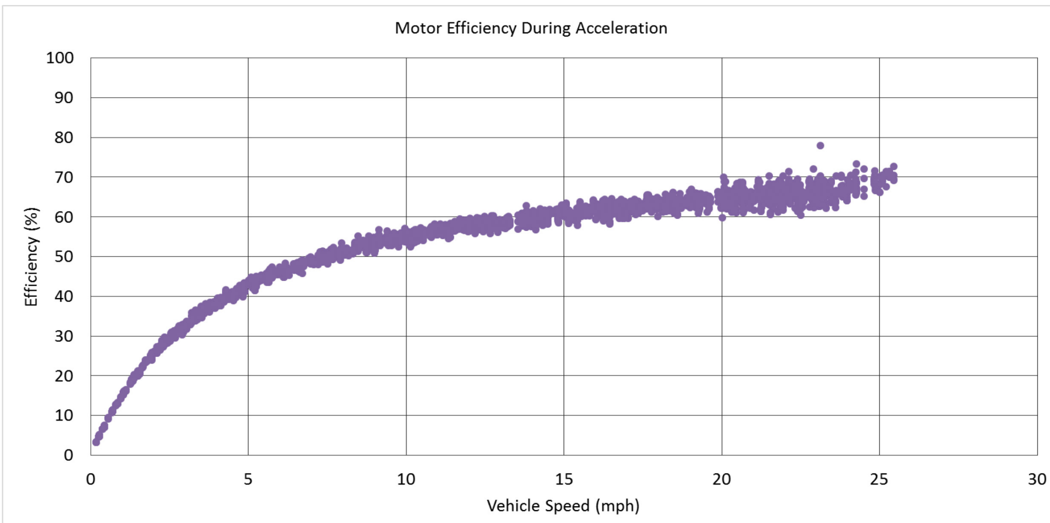

The final form of this system model is as follows:

Equation III-28

$$\boldsymbol{I_{vehicle,accel}} = \boldsymbol{I_{rotational}} + \boldsymbol{I_{torque}} + \boldsymbol{I_{efficiency\ loss}}$$

Equation III-29

$$I_{vehicle,accel} = D \cdot \left(Torque_{vehicle,accel} \cdot \omega_{wheel}\right) + E \cdot Torque_{vehicle,accell} - F \cdot \omega_{wheel}$$

The accuracy of the model for this type of application is demonstrated using the go-kart traction motors. The values for D, E, and F were tuned for the go-kart traction motors and their values are displayed in Table III-6.

Table III-6 Example Tunings for the Go-Kart

Controller Coefficient	Value
D	7.8
E	5
F	18

A driving profile was designed to demonstrate the generality of this model to a range of vehicle speeds and torques. The vehicle speed and throttle signals for this test are showing in Figure III-61. The resulting current data collected using the motor controllers is displayed in Figure III-62.

Figure III-61 Go-Kart Test Acceleration Driving Profile

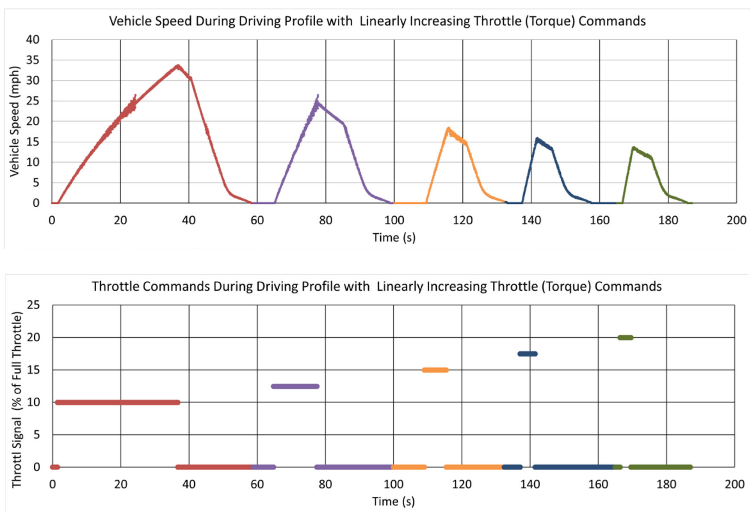

Figure III-62 Battery Current During Test Acceleration Driving Profile

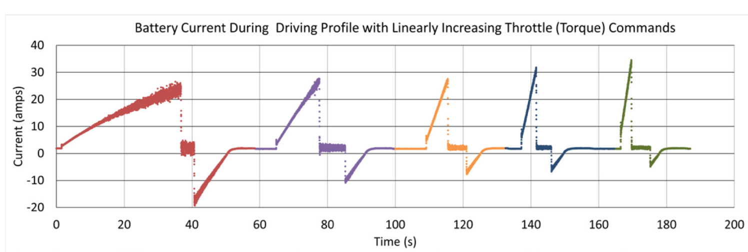

Figure III-63 shows the measured current, the same current data shown in Figure III-62, and the current predicted by the model plotted against each other. Note that there is still good agreement between this simple model and the recorded data. Again it is important to note that this model uses only the accelerator pedal position and the real-time wheel speed and the data is available before the actual current develops so that the flywheel has time to react.

Figure III-63 Open Loop Predicted Battery Current vs Actual Current During Acceleration

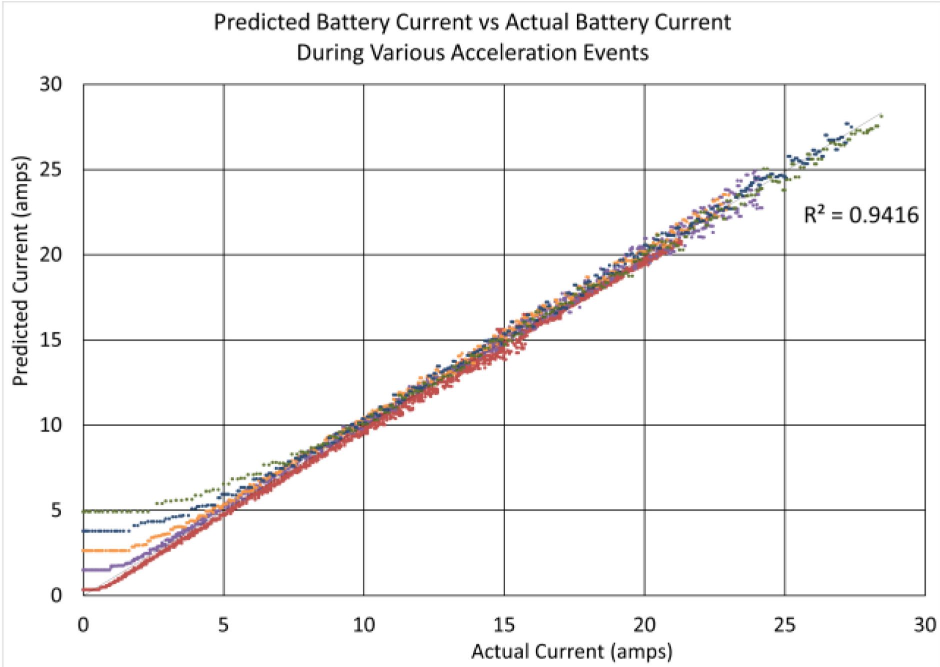

Chapter IV. Flywheel Energy Storage System Testing

Section 4.01 Parasitic Loss Experimental Setup

The INSTAR system has, from its inception, been designed to accept higher parasitic losses when compared to other modern flywheel energy storage systems while still maintaining its core system efficiency benefits. It does this mainly through the control system that is intended to use the flywheel to only store the *excess* regenerative braking energy the battery pack was previously unable to handle. This allows for both a small amount of energy to be stored in the flywheel and for it to be stored for only a few minutes maximum as it is immediately put back into the battery pack or sent to the drive motors to reaccelerate the vehicle. This allows the system to employ conventional, commodity spindle components which can increase the reliability of the system while reducing cost. Section 3.02(a) discussed the analysis behind the selection of these components. This section presents flywheel spin-down test results that can further help inform future spindle design choices.

The performance of the INSTAR flywheel spindle was gauged in relation to its round trip storage efficiency. The round trip efficiency of the flywheel energy storage system can be thought of as a minimization of the losses required to absorb, store, and reuse the energy put into the system. These losses consist of mechanical losses from friction in the ball bearings and PTFE lip seals, fluid drag (windage) losses from the spinning disk, electrical resistance losses in the motor coils, and core losses in the motor stator. There are also parasitic electrical power losses associated with the motor controller and any pumps required for pulling a vacuum and/or lubrication circulation.

The minimization, or complete elimination, of these losses must be weighed against their resultant financial and complexity costs. Some losses are quite small and would be prohibitively impractical to further reduce/eliminate. The motor hysteresis and eddy current losses were minimized by lamination material selection, lamination thickness selection, and motor pole count as described in Section 3.02(c). Further reduction in these losses through better materials or thinner laminations is possible, but unlikely due to higher cost. As it will be shown, there are better ways to further increase the efficiency. The flywheel energy storage system's Sevcon Gen4 DC motor controller is operating at 80V and require approximately 0.5 Amps (~40 Watts) for operation. The cost and time associated with developing a lower power, but similarly robust motor controller, are not in my opinion justified. Reducing the power consumption of this controller by 50% would only reduce the losses by 20W. Over a 30 second, 22 kJ flywheel energy storage event this results in a 3% efficiency loss. Again, as it will be shown, there are many better ways to increase the efficiency if necessary.

The first question that this spin-down test was designed to answer is about the necessity of the vacuum containment system. The analysis in Section 3.02(a) showed that a 10W vacuum pump's power draw would be outweighed by the power savings associated with lower windage losses. This did not, however, include the friction from the seals required to maintain that vacuum. The number of these seals, and hence the total seal friction drag, depends on the design of the flywheel spindle. It can be as little as one for a cantilevered flywheel or as many as 3, as it is in this prototype design. If the overall benefit from the vacuum system, including the seals, is not glaringly obvious it should be considered for elimination to further reduce the cost and complexity of the system.

The second question was on the possibility of using grease bearings rather than oil-lubricated ball bearings. Grease bearings do not require an oil recirculation system which eliminates the need for pumps and a reservoir, reducing cost, mass, and electrical power losses.

The losses in the flywheel system are empirically calculated by bringing the flywheel up to speed and letting it coast down to zero speed, logging the rotation rate over the entire deceleration event. As these were the first test performed on the prototype flywheel, it was placed inside a polycarbonate ballistics testing chamber. The 80V battery pack, the same one used on the go-kart test platform was placed on the ground outside the chamber. The potentiometer throttle was wired into the motor controller and located outside the chamber as well.

Figure IV-1 INSTAR Test Setup in Ballistics Test Chamber

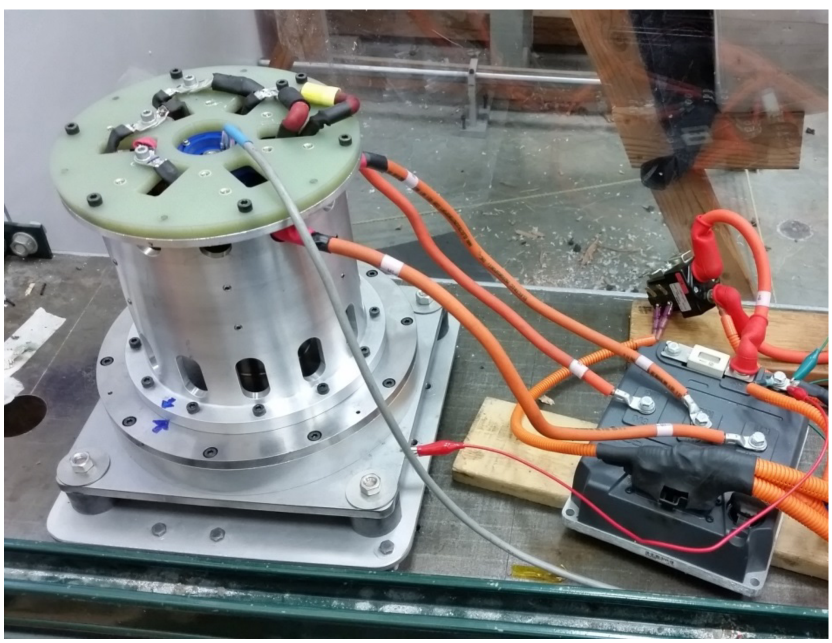

Figure IV-2 INSTAR Spindown Test Thermocouple Locations

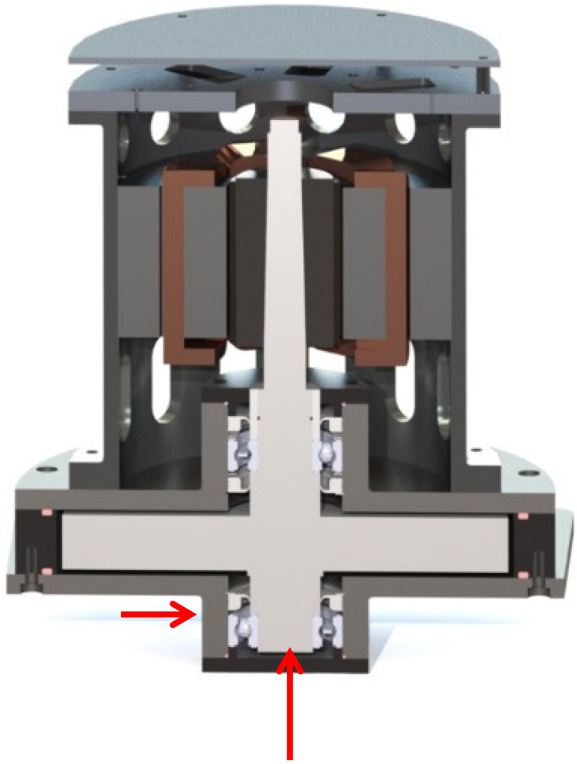

The flywheel was brought up to its initial maximum allowed speed of 11,000 RPM. It is capable of more, but was limited during initial testing for safety. The throttle was then instantaneously zeroed and the flywheel allowed to coast back down to zero speed. The motor controller was used to record both the time and flywheel speed during the test at 40 ms time intervals. Average power loss was calculated by dividing the energy stored in the disk at maximum speed (~22 kJ) by the time required to reach zero speed. Temperature measurements using a thermocouple of the case where the bottom bearing is located and of the shaft where the bottom bearing is located were taken before and after. Each test started with the flywheel at room temperature (22C). Each successive test allowed for a 24 hour resting period to allow the flywheel to thermally settle back to the controlled room temperature. This was also necessary as each test required disassembling and reassembling the flywheel in order to add and/or remove components.

Section 4.02 Parasitic Loss Experimental Test Results

Figure IV-3 Flywheel Spindown Bearing and Seal Comparison

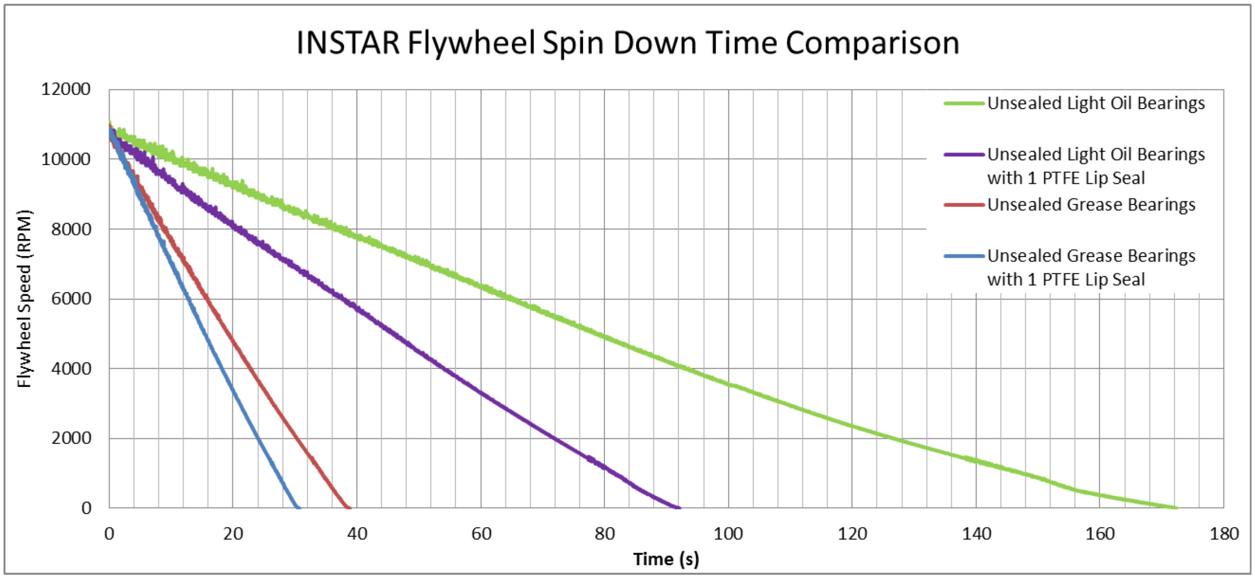

Table IV-1 Summary of Spindown Comparison

	Spindown Time (s)	Power Loss (W)	Difference (W)	ΔT Case C	ΔT Shaft C
2x Oil Bearing 0 PTFE Lip Seals	172	127	--------------	+1	+1
2x Oil Bearing 1 PTFE Lip Seals	92	237	+110	+3	+19
2x Sealed Grease Bearing 0 PTFE Lip Seals	39	563	+436	+19	+36
2x Sealed Grease Bearing 1 PTFE Lip Seals	31	712	+585	+18	+45

The first test using two grease bearings quickly showed that grease bearings are very unlikely to be successfully implemented into this type of system. Despite their lower maintenance requirements and lower cost, the high drag will overwhelm any potential benefit of the INSTAR system if it employs grease bearings. This is true even without seals. The friction from the grease will not only reduce the round-trip efficiency, but cause high temperature rise as well. A single spin-down event raised the shaft temperature by over 35 degrees Celsius (95 Fahrenheit).

A more interesting method of viewing this data is by looking at the stored energy over time rather than just at the speed over time. The stored energy in the flywheel follows a very straightforward equation, especially given the simple shape of the solid disk.

Equation IV-1

$$Energy_{flywheel} = \frac{1}{2}\, I\, \omega^2$$

Figure IV-4 Flywheel Energy During Spindown Test

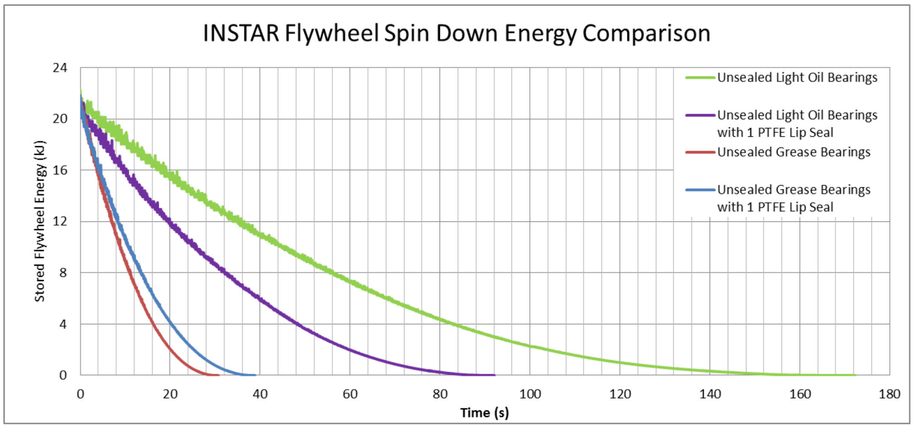

From this graph it is obvious that the average power loss average previously calculated is heavily skewed by the long tail of the graph. A more useful metric is defined for the time scale of an actual braking event. For the go-kart, a 1C charge rate is equivalent to 3.2 kW. A 22kJ storage event, like the one in this spin-down test, can safely be put back into the battery over 7 seconds at this rate. A more useful comparison of the parasitic losses is the average power loss during the first 5 seconds (see Table IV-2) or first 10 seconds (see Table IV-3).

Table IV-2 Energy Summary During Spindown Test over First 5 Seconds

	Spindown Time (s)	Energy lost first 5 seconds (kJ)	% of Initial Energy Lost	Power Loss first 5 seconds (W)	Difference (W)
2x Oil Bearing 0 PTFE Lip Seals	172	2.5	11.3	504	-----------
2x Oil Bearing 1 PTFE Lip Seals	92	2.8	12.8	553	+49
2x Sealed Grease Bearing 0 PTFE Lip Seals	39	6.5	29.8	1300	+797
2x Sealed Grease Bearing 1 PTFE Lip Seals	31	7.1	33.5	1429	+925

Table IV-3 Energy Summary During Spindown Test over First 10 Seconds

	Spindown Time (s)	Energy lost first 10 seconds (kJ)	% of Initial Energy Lost	Power Loss first 10 seconds (W)	Difference (W)
2x Oil Bearing 0 PTFE Lip Seals	172	4.2	18.9	420	-----------
2x Oil Bearing 1 PTFE Lip Seals	92	5.8	26.9	581	+161
2x Sealed Grease Bearing 0 PTFE Lip Seals	39	11.2	51.4	1,122	+702
2x Sealed Grease Bearing 1 PTFE Lip Seals	31	12.4	58.2	1,240	+820

Section 4.03 Analysis of Parasitic Loss Experimental Test Results

From this information it is again quite apparent that grease bearings have high parasitic drag losses. Within only 10 seconds over 50% of the stored energy has been lost. 30% has been lost in the first 5 seconds. This is unacceptable and does not take account how much would be lost accelerating the disk, which would only make the effect on the round trip efficiency even more drastic. From this experimental data it is safe to say that grease bearings cannot be considered for this application. While this information might seem obvious, as modern flywheels employ magnetic levitation, the INSTAR system uses flywheels in a different way than other flywheels energy storage systems. The INSTAR system only requires the flywheel to store energy for minutes at a time, maximum, while the others are designed to store energy for long periods of time [OAK RIDGE]. Despite this different application and different use methodology, grease bearings again prove to be better utilized in other applications, mostly low speed ones requiring less frequent maintenance.

This testing also does not show much promise for employing a vacuum system to reduce the windage losses. More testing will need to be performed to verify the theoretical data from Figure II-1, but at 50-150W per seal, there is likely only to be minimum added value compared to the complexity and cost of the system. If 150 watts are lost only to gain 150-200 watts then the cost and complexity aren't justified. The rest of the testing was performed *without* a vacuum in order to gauge the total system performance at ambient pressure. Implementing the system at ambient pressure would again increase the attractiveness of the system through lower cost and few moving parts that can require maintenance, like the vacuum pump.

From this data it is also clear that oil-lubricated ball bearing losses should be acceptable. While the ball bearings, of course, have parasitic losses that a magnetic levitation bearing can further reduce, the total system losses with oil-lubricated ball bearings only total 10-20% of the total stored energy over the braking period. This magnitude of loss is acceptable for this proof-of-concept system as it still allows the vast majority of the stored braking energy to be put back into the vehicle, either through the motor or through the battery pack. Deep groove 6205 radial ball bearings using a light spindle oil ISO grade 15 were used for the full INSTAR system tests that will follow in Chapter V..

These losses can be loosely extrapolated to give some insight into the possibility of using ball bearings for a system much larger than the test go-kart vehicle. A loaded delivery truck can weigh anywhere from 10,000-16,000 pounds. The lightest truck can be roughly analyzed to inform the feasibility of using ball bearings for an INSTAR-type system installed on this size vehicle. A larger truck, with its larger mass (and hence higher available energy and higher required stopping torque), would provide more favorable results. The lightest truck is analyzed in order to provide a more conservative value for this analysis.

A 10,000 pound [m = 4,500 kg] delivery truck travelling at 20 mph [v = 9 m/s] has ~180 kJ in kinetic energy.

$$Energy_{vehicle} = \frac{1}{2}\, m\, v^2 \;\approx\; 180\; kJ$$

The spindown testing was performed at 11,000 RPM. For a more direct comparison, this same rotation rate can be used to extrapolate the losses to a larger vehicle. Adding 1.5 inches to the radius (11 inch total diameter) and increasing the thickness to 2.5 inches (instead of 1 inch) provides the necessary energy storage for the entire delivery truck braking event at 11,000 RPM. This larger flywheel is five times more massive than the prototype go-kart flywheel and stores 195 kJ at 11,000 RPM. Assuming the entirety of these losses are bearing losses and that these losses scale linearly with larger flywheel mass, a conservative bearing loss is five times the loss as this test.

$$Power_{Loss} = 2.5\; kW$$

The power required to stop the vehicle, or with a hybrid vehicle the power available to charge the battery pack, depends on the length of time over which the vehicle comes to a stop.

Equation IV-2

$$Power_{Braking} = \frac{Energy_{vehicle}}{Time_{Braking}}$$

Typical hybrid vehicles produced in the past few years have around 350 V battery packs [NREL REF]. The power these can absorb depends on this voltage and the battery pack maximum, safe charging rate.

Equation IV-3

$$Power_{Battery\ Charge} = 350\ V \cdot I_{Max}$$

Over the course of the braking event the battery pack can safely absorb:

Equation IV-4

$$Energy_{Battery\ Charge} = Power_{Battery\ Charge} * Time_{Braking}$$

The flywheel energy storage system must then absorb the remainder of the braking energy at the remainder of the braking power if the entirety of the braking event is to be absorbed by the INSTAR system.

Equation IV-5

$$Power_{Flywheel\ Absorb} = Power_{Braking} - Power_{Battery\ Charge}$$

Equation IV-6

$$Energy_{Flywheel\ Storage} = Energy_{vehicle} - Energy_{Battery\ Charge} = Power_{Flywheel\ Absorb} * Time_{Braking}$$

Typical hybrid vehicle battery packs for small cars range from 5-7 Ah [NREL]. Companies currently researching high-power battery packs for commercial hybrid vehicles like a delivery truck are 8-10 Ah in capacity [A123 REF].

Table IV-4 Hypothetical Hybrid Vehicle Braking Scenarios

$Time_{Braking}$	$Power_{Braking}$	I_{Max}	**@10 Ah**	$Power_{Battery\ Charge}$ @ $350V$	$Energy_{Flywheel\ Storage}$
1.5 seconds	120 kW	10 A	1C	3.5 kW	175 kJ
		20 A	2C	7 kW	170 kJ
		40 A	4C	14 kW	160 kJ
3 seconds	60 kW	10 A	1C	3.5 kW	170 kJ
		20 A	2C	7 kW	160 kJ
		40 A	4C	14 kW	140 kJ
5 seconds	36 kW	10 A	1C	3.5 kW	162 kJ
		20 A	2C	7 kW	145 kJ
		40 A	4C	14 kW	110 kJ

If this this stored flywheel energy is put back into the traction motors to accelerate the vehicle back to 20 mph [9 m/s] over three seconds immediately after the braking event, it will need to output 60 kW. At 60 kW, any of these scenarios has the flywheel emptied in 2-3 seconds. A 3 second pause during the stop before accelerating results in the stored energy remaining in the flywheel for 5-6 seconds. 2.5 kW in losses for 6 seconds is 15 kJ in losses (8-11% of the stored flywheel energy). This level of losses seem quite acceptable, especially given the conservative method of calculation.

If the stored flywheel energy is put back into the batteries rather than the traction motors it can only be discharged from the flywheel at the same rate the batteries are allowed to charge at. Table IV-5 contains estimates on the energy losses expected for the different charge rates.

Table IV-5 Comparison of 2.5kW Flywheel Losses During Hypothetical Braking Events

I_{Max}	$Power_{Battery\ Charge}$ @ $350V$	$Time_{Braking}$	$Energy_{Flywheel\ Storage}$	$Time_{Discharge}$	$Energy_{Lost}$ @ 2.5 kW	% Lost
10 A	3.5 kW	5 sec	175 kJ	50 sec	125 kJ	71%
		3 sec	170 kJ	49 sec	122 kJ	72%
		1.5 sec	160 kJ	46 sec	115 kJ	72%
20 A	7 kW	5 sec	145 kJ	21 sec	53 kJ	36%
		3 sec	160 kJ	23 sec	57 kJ	36%
		1.5 sec	170 kJ	24 sec	60 kJ	35%
40 A	14 kW	5 sec	110 kJ	8 sec	20 kJ	18%
		3 sec	140 kJ	10 sec	25 kJ	18%
		1.5 sec	160 kJ	12 sec	30 kJ	19%

From this top-level analysis it is quite clear that the more work will need to be done to increase the energy storage capacity of the flywheel without adding much more parasitic losses. This is especially true for the 10 amp charge limit case, as this puts the least amount of stress on the battery pack. The system should be designed to be able to maintain both low battery charge rates and high efficiency. With losses around 2.5 kW, the two design goals appear to be mutually exclusive. A high charge rate of 40 amps captures the most energy, but puts higher stress on the battery pack. A low charge rate of 10 amps results in most stored energy being lost in the flywheel.

Reducing these parasitic bearing losses can be done directly through selection of lower friction bearings or through reducing the mass supported by the bearings, and hence the normal force/friction force on the ball bearings themselves. This can be done by increasing the energy *density* of the design - storing more energy in the flywheel without adding mass. The solid disk design of the prototype flywheel is mass inefficient, but simple to analyze and fabricate. A more complex, but energy dense design is quite feasible and is currently being investigated by other members of the INSTAR lab. A potential solution is the use of a design featuring a hub and spoke array to remove mass from the interior of the flywheel, where it is less efficient in increasing the moment of inertia. Table IV-6 contains estimates of the losses assuming the parasitic losses can be kept below 1 kW for the larger system.

Table IV-6 Comparison of 1kW Flywheel Losses During Hypothetical Braking Events

I_{Max}	$Power_{Battery\ Charge}$ @ $350V$	$Time_{Braking}$	$Energy_{Flywheel\ Storage}$	$Time_{Discharge}$	$Energy_{Lost}$ **@ 1 kW**	**% Lost**
10 A	3.5 kW	5 sec	175 kJ	50 sec	50 kJ	29%
		3 sec	170 kJ	49 sec	49 kJ	28%
		1.5 sec	160 kJ	46 sec	46 kJ	29%
20 A	7 kW	5 sec	145 kJ	21 sec	21 kJ	14%
		3 sec	160 kJ	23 sec	23 kJ	14%
		1.5 sec	170 kJ	24 sec	24 kJ	14%
40 A	14 kW	5 sec	110 kJ	8 sec	8 kJ	7%
		3 sec	140 kJ	10 sec	10 kJ	7%
		1.5 sec	160 kJ	12 sec	12 kJ	7%

While storing nine times more energy than the prototype, this calculation allows for only twice as many parasitic losses. Maintaining high energy efficiency at the 10 amp charge rate still appears quite ambitious. It is quite clear that the reduction of the parasitic drag losses will need to be a major focus of effort moving forward.

Section 4.04 Round Trip Efficiency Experimental Setup

The single best measure of the flywheel performance is the round trip energy storage efficiency - what percentage of the total energy that you put into the flywheel can you get back out as useful energy. The parasitic losses described in the earlier sections of this chapter are only one factor that affects the round trip efficiency. Just as important is the regenerative braking efficiency – how well the motor is able to convert the flywheel's stored rotational kinetic energy back into electricity that can be used to accelerate the vehicle through the traction motors or to recharge the battery pack at a safe rate.

This is done by bringing the flywheel up to 11,000 RPM and then regeneratively braking the flywheel motor to decelerate the disk and charge the battery pack. The energy used to accelerate the flywheel disk ($Energy_{In}$) is compared to the energy this specific flywheel disk has when rotating at 11,000 RPM. This is defined as the efficiency up ($Efficiency_{Up}$) and is calculated by Equation IV-7. Since there are always losses, the energy consumed is always larger than the calculated stored energy and $Efficiency_{Up} < 1$.

Equation IV-7

$$Efficiency_{Up} = \frac{Energy_{Flywheel\ @\ 11{,}000\ RPM}}{Energy_{consumed\ During\ Flywheel\ Acceleration}} = \frac{\frac{1}{2} I \cdot \omega^2}{Energy_{Consumed}} = \frac{23\ kJ}{Energy_{Consumed}}$$

The energy used to accelerate the disk is also compared to the energy generated that recharges the battery pack. This is defined as the round trip efficiency ($Efficiency_{Round\ Trip}$) and is calculated by Equation IV-8:

Equation IV-8

$$Efficiency_{Round\ Trip} = \frac{Energy_{out}}{Energy_{in}} = \frac{Energy_{Battery\ Charge}}{Energy_{Consumed\ During\ Flywheel\ Acceleration}}$$

This test was performed inside a polycarbonate safety enclosure with the flywheel attached to one of the 20 Ah 80V $LiFePo_4$ battery packs, placed outside the enclosure. It is the same setup as seen in Figure IV-1. The test consisted of four consecutive, identical cycles. Positive current is energy flowing from the battery pack into the flywheel motor (battery discharge). Negative current is energy flowing from the flywheel motor to the battery pack (battery charge). The energy measured during these tests are calculated by integrating the instantaneous power, as measured by the motor controller every 30 ms.

Equation IV-9

$$Energy = \sum Power_{battery} * \Delta t = \sum I_{battery} * V_{battery} * \Delta t$$

Section 4.05 Round Trip Efficiency Experimental Test Results

The resulting flywheel speed profile is shown in Figure IV-5. The flywheel starts at zero speed for each test, reaches 11,000 RPM in eight seconds, and is then decelerated back down to zero speed 14 seconds later.

Figure IV-5 Flywheel Speed During Round Trip Efficiency Testing

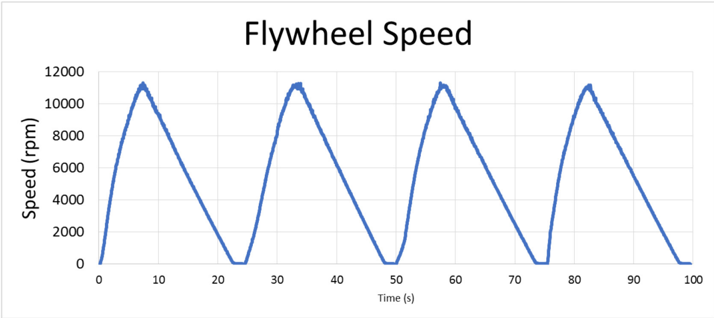

This speed profile results in an average power of 2.9 kW during acceleration and 1.6 kW during deceleration. The resulting flywheel current profile is shown in Figure IV-6. The flywheel consumes a maximum of 85 amps, which is reached at peak flywheel speed. This will be further discussed in 0.

Figure IV-6 Battery Current During Flywheel Round Trip Efficiency Testing

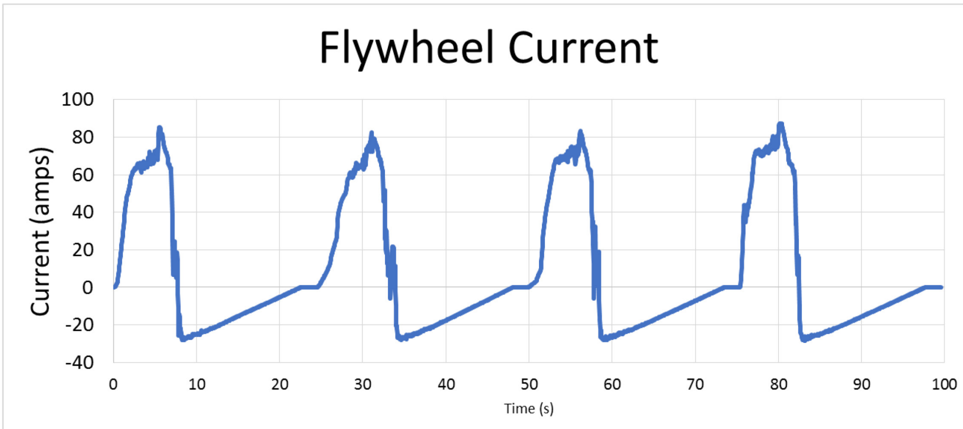

The total energy actually used to accelerate the flywheel, the energy recaptured during regenerative braking and used to recharge the battery, and the calculated efficiencies for each peak are all collected into Table IV-7.

Table IV-7 Peak-by-Peak Round Trip Efficiency Testing

	Peak 1	Peak 2	Peak 3	Peak 4
$Energy_{Flywheel\ @\ 11,000\ RPM}$	23.0 kJ	23.0 kJ	23.0 kJ	23.0 kJ
$Energy_{Consumed}$	26.1 kJ	25.9 kJ	27.5 kJ	27.6 kJ
$Energy_{Battery\ Charge}$	18.4 kJ	17.7 kJ	18.9 kJ	18.9 kJ
$Efficiency_{Up}$	88.3%	89.0%	83.7%	83.4%
$Efficiency_{Round\ Trip}$	70.7%	68.5%	68.7%	68.3%

Section 4.06 Analysis of Round Trip Efficiency Experimental Test Results

There are three main observations from this test data:

1. The $Efficiency_{Up}$ across all four peaks is sufficient for the initial implementation of the
   full INSTAR system, but has moderate variability.

2. The $Efficiency_{Round\ Trip}$, driven by a consistent energy recapture across all four
   peaks, is also sufficient for the initial implementation of the full INSTAR system, as is.

3. The current control in the Sevcon motor control needs better tuning to smooth out the
   current profile. This affects the variability of $Efficiency_{Up}$ and the magnitude of both $Efficiency_{Up}$ and $Efficiency_{Round\ Trip}$.

This custom-built INSTAR prototype DC brushless motor roughly matches the documented 90% efficiency of the off-the-shelf traction motors purchased from Mars Motors. This is sufficient for the proof of concept implementation of the INSTAR system and could be improved, if necessary, through widely available motors with higher efficiencies. The efficiency, however, suffers from a non-optimal current controller. The current control on the Sevcon Gen 4 motor controller is hard-limited to keep the flywheel rotation rate at, or below, 11,000 RPM. At this 11,000 RPM max speed the current controller "fights" itself and spends an excessive amount of current keeping the speed right at 11,000 RPM. This effect is highlighted in Figure IV-7. It is caused by the motor controller's internal PID current controller and internal PID speed controller destabilizing each other when bumping up against the hard-limited max speed.

Figure IV-7 Motor Controller Instability During Round Trip Efficiency Testing

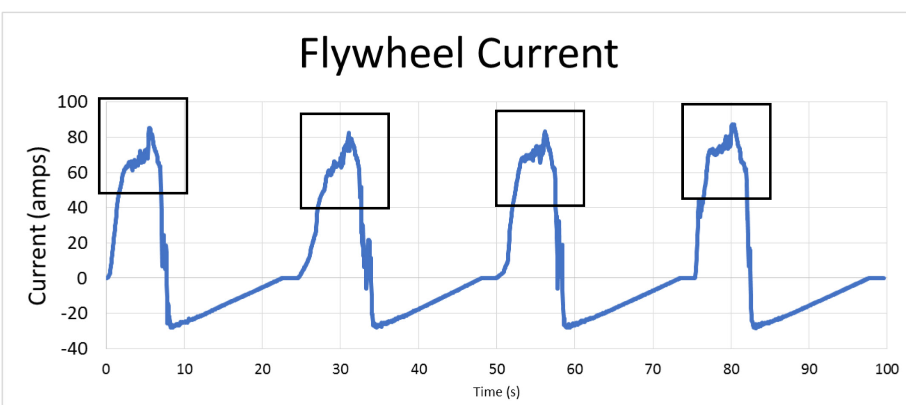

This results in extra, non-useful current being consumed by the motor and driving up the $Energy_{Consumed}$. With a larger amount of energy consumed, this drives down both the $Efficiency_{Up}$ and the $Efficiency_{Round\ Trip}$. More time spent tuning the motor controller can reduce this effect. It should be emphasized that during normal INSTAR operation, however, this can be avoided by placing the hard speed limit above the flywheel operating range. This way the internal speed controller is never used as the flywheel stays below the hard limit. The current controller can then be left undisturbed and provide sufficient reliability as it does with the regenerative braking, where the speed controller never interferes with it.

Chapter V. Full-System Testing

Section 5.01 Experimental Setup

The INSTAR system has been designed to improve the regenerative braking energy capture capabilities of hybrid and electric vehicles. Hence, the testing and tuning revolves mainly around putting the system through a series of braking events and observing two things: how much energy is captured during the event and where/when the energy was stored during the event. The second component is especially important if the chemical batteries are required to never see charging currents above a certain threshold.

The main instrumentation for this testing consists of four distributed current sensors: one for each drive motor, one for the flywheel, and one for the battery pack. The current from the drive motors and flywheel is measured using their respective Sevcon Gen4 motor controllers and reported via CAN. The system battery pack consists of two 40Ah battery packs in parallel, and the current sensor for the pack was measured at their common connection point. This current sensor is a Temura L03S200D15, a Hall effect-based non-invasive current sensor, capable of measuring up to 200 amps, with a 5 µs response time and 1% accuracy. The system voltage is measured using a voltage divider directly reading the battery pack voltage. All sensors are read by the National Instruments cRIO-9076 first through the FPGA and then logged at 5 ms intervals by the real-time processor.

Figure V-1 INSTAR Go-Kart Power Flow Diagram with Current Sensor Locations

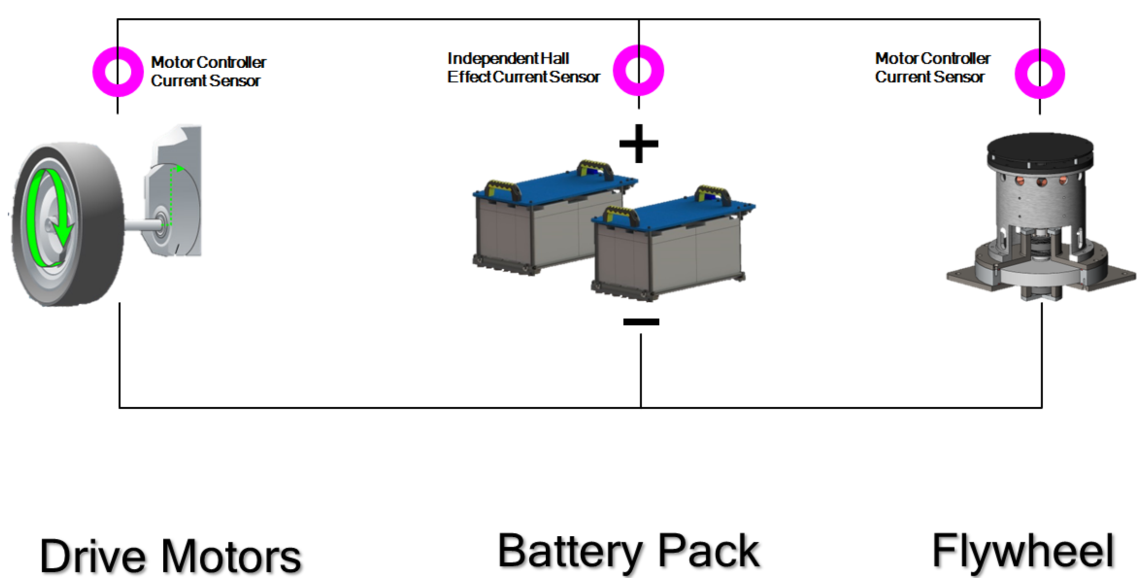

Figure V-2 Example Single Braking Event Vehicle Speed

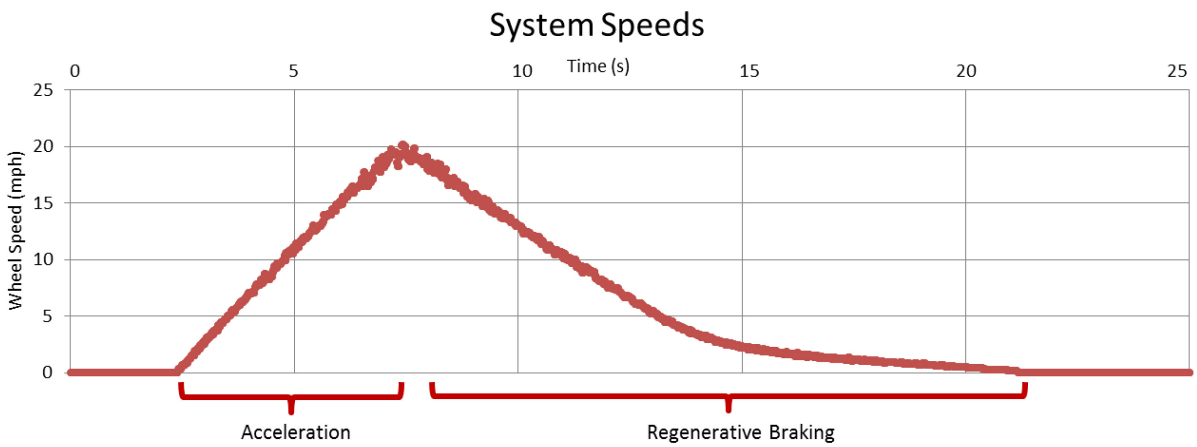

A single braking event includes accelerating the vehicle up to a desired speed, coasting for a determined amount of time, and then braking with a controlled, and potentially variable, braking torque. A typical velocity profile for one of these events is seen in Figure V-2. Rather than requiring a driver to accurately repeat the same experiment for tuning and testing, the vehicle had two 35 inch diameter, 1 inch thick steel disks installed in place of the rear wheels so that the testing could be performed in the lab. The disks replaced the inertia of the vehicle and driver and allowed the motors and battery packs to be put under the same load in the lab and while driving around, as described earlier in Chapter III.

Figure V-3 INSTAR Testing on Test Vehicle with Inertial Load Disks

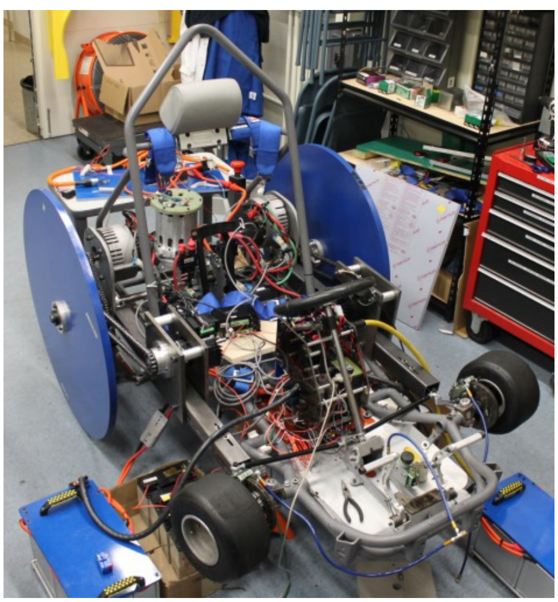

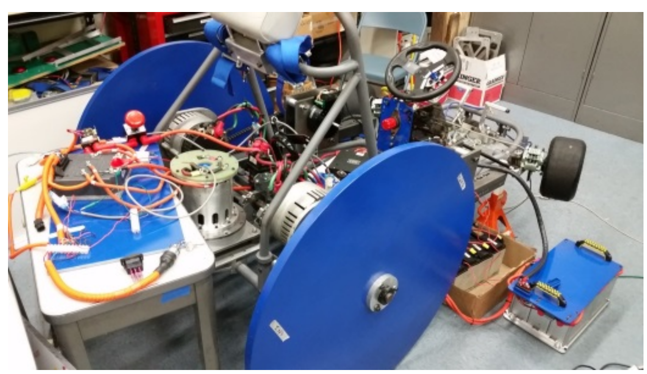

Control Event:

The system was tested with and without the flywheel in order to be able to directly compare its impact on the power flow and energy recovery. Each test included a control event, defined as a braking event without the presence of the flywheel, which allowed the chemical batteries to see the entirety of the regenerative braking charging current. The batteries are capable of absorbing these levels of current, but should not in order to preserve their lifetime capacity [Choi]. Temperature rise due to these high charging currents is both a safety and lifetime concern as well, but the tests were intentionally split across multiple hours and multiple days to ensure that the temperature stayed at a safe level.

A typical example of the current seen by the battery pack during a braking test without the flywheel, a control event, is shown in Figure V-4. It has several notable features:

a) At all speeds, including zero speed when the vehicle is stationary, there is a 2 amp current draw required to power the electronics and is seen by the non-zero offset at time = 0.
b) When the vehicle starts there is an essentially instantaneous jump in current required to overcome the stiction in the system and get the disks moving.
c) The vehicle accelerates with constant torque, and hence a linearly increasing wheel speed, which requires more current to maintain at higher speeds as the power increases linearly with wheel speed.
d) The accelerator pedal is released and the vehicle begins to coast. The current draw returns to zero amp as no torque is being applied, but the vehicle is still at its peak velocity due to its inertia. This would be seen in a real driving scenario when the driver removes their foot from the accelerator pedal and moves it to the brake pedal before initiating the braking event.
e) The braking event initiated by the application of the brake pedal. The current quickly, but not immediately, reaches its full and requested value over the course of 25ms to 300ms depending on the braking application rate.
f) The peak current seen by the batteries quickly follows the braking request. Avoiding the current at this peak is the focus of much of this work, as this peak is responsible for the largest charging currents seen during regenerative braking.
g) A constant braking torque slows the vehicle and the charging current drops as the vehicle slows down.
h) The braking event is over, the vehicle is below 5 mph, no regenerative braking torque is applied, and the batteries are no longer being charged.

Figure V-4 System Currents During a Single Braking Event without INSTAR

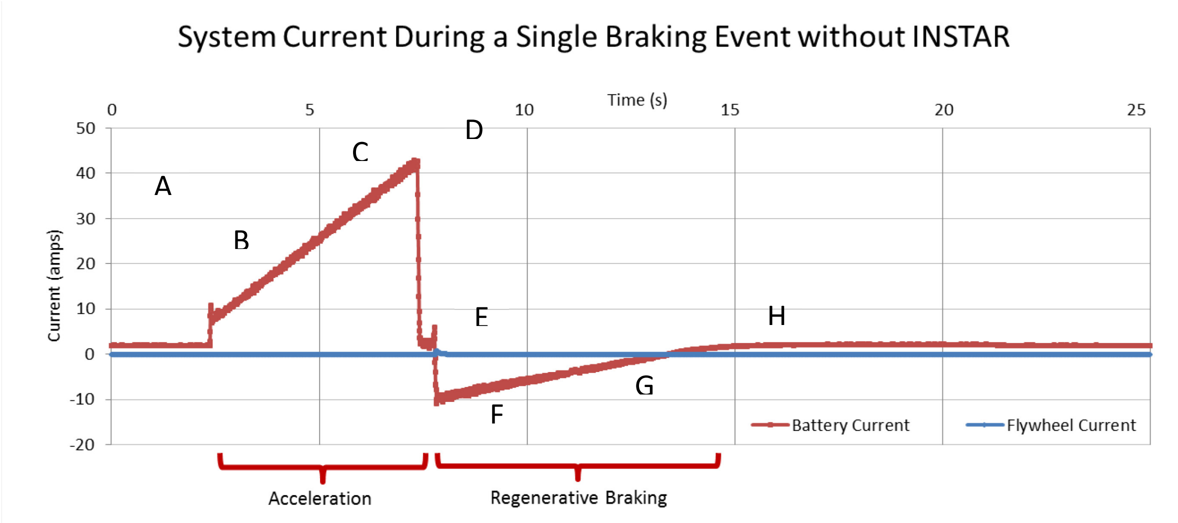

Figure V-5 Vehicle Speed During Single Braking Event

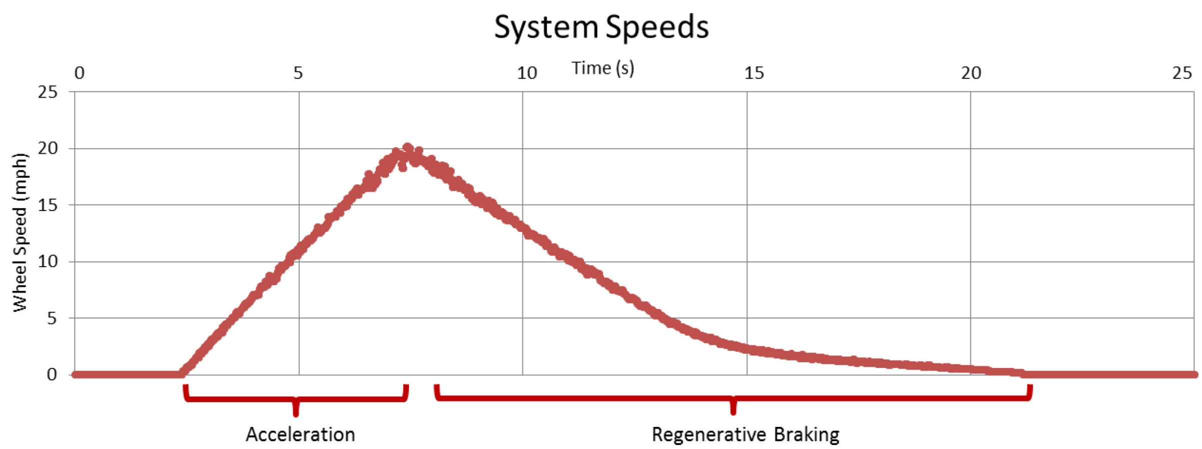

Section 5.02 Open Loop Tuning

The open loop controller was quickly found to be able to react fast enough to avoid sending the large, initial current spike to the battery pack, unlike the closed loop controller. The open loop controller has the ability to react fast enough because it can react earlier in the braking event than the closed loop PI controller as it is based off the brake pedal signal, the same signal that initiates the braking event, and not the current sensor. The open loop controller provides, as was previously shown, an accurate estimate of the current that the system will see during regenerative braking *before* that current is delivered by the traction motors, rather than after it has developed as in the case of the closed loop PI controller. This allowed for the large current spike seen at the beginning of the braking event to be captured by the flywheel rather than the batteries.

The majority of the testing was therefore dedicated to exploring this controller in order to better understand its effect on the system power flow, what affects its performance, and how it can be potentially combined into a future, more robust and optimized controller.

There were found to be four main tuning variables that affected the performance of the open loop controller. Better performance was defined as the controller's ability to limit the maximum current sent to the batteries and the total energy captured by the system during regenerative braking, taking the flywheel losses into account. These four factors are:

- The braking torque request rate
- The flywheel motor controller's torque application rate
- The open loop controller coefficients, and hence the resulting flywheel throttle in response to the observed instantaneous wheel speed braking torque request
- The flywheel's initial speed at the initiation of a braking event

Braking Torque Request Rate

As the open loop controller was chosen for its ability to quickly react to the initiation of a braking event it is important to understand what determines how the braking events are initiated and what kind of response the controller really needs to have. In a human-driven vehicle, in contrast to a computer-controlled vehicle, the most reliable way to detect a braking event is through the brake pedal signal. In a hybrid or electric vehicle this signal commands the motor controllers to first initiate regenerative braking, if possible, and secondly to apply the mechanical brakes, if necessary.

The motor controllers respond to this braking signal by allowing for current to flow to the batteries and recharge them, and as a result, a braking torque is applied to the traction motors and then to the driven wheels. How quickly this current develops depends on how much braking torque is requested, and how quickly the braking torque signal develops. In a vehicle this braking torque signal is provided by the driver's foot depressing the brake pedal. Clearly this does not happen instantaneously, nor is it reliably predictable or consistent. How quickly the driver depresses the brake pedal depends entirely on their driving style, the driving situation, and the road conditions. It is unlikely, and most likely unnecessary, to develop a controller that optimizes the flywheel response for 100% of all possible braking events. Instead the controller can be designed for the events most commonly seen during normal operation, in order to eliminate unnecessary controller complexity while still retaining the vast majority of the benefits.

The INSTAR system was put through a series of braking events with the same final braking torque, but linearly ramped up to over a range of times: 50 ms to 300ms in 50 ms increments, plus instantaneously for comparison. The braking signal time profile is shown in Figure V-6.

Figure V-6 Braking Profile With Varied Brake Application Rates

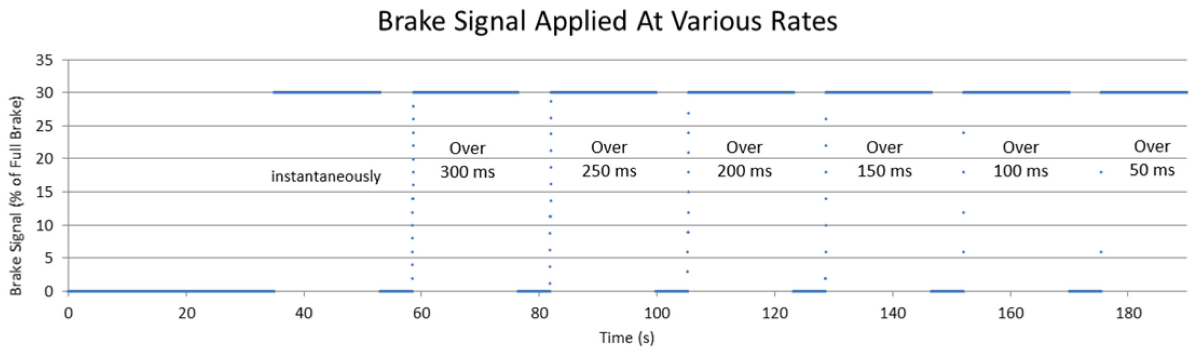

The system current without the flywheel, a series of control events for this test, is shown in Figure V-7.

Figure V-7 Battery Current with Varied Braking Application Rates without INSTAR

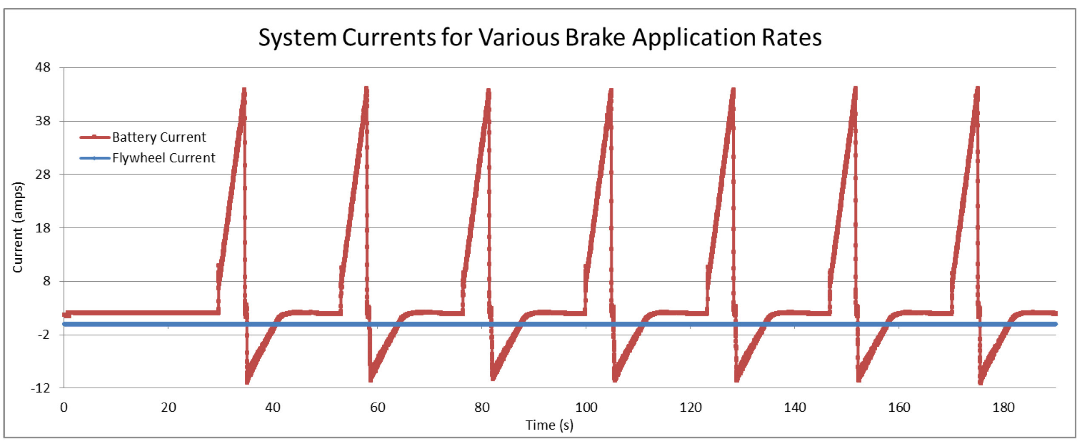

The system current with the flywheel operating, including the braking profile for ease of reference, is shown in Figure V-8. A zoomed in picture of each battery charging peak is shown in Figure V-9. A control event is shown at the far right for comparison.

Figure V-8 System Currents with Varied Braking Application Rates with INSTAR

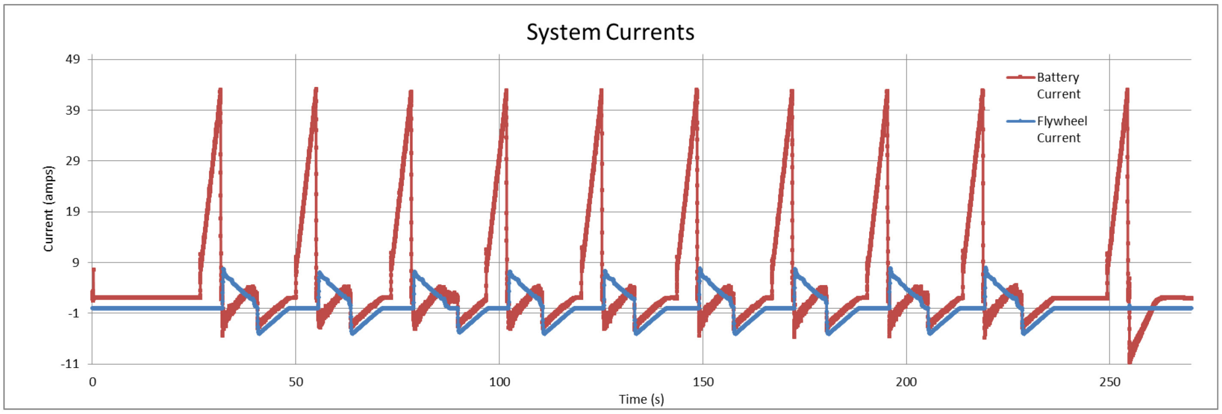

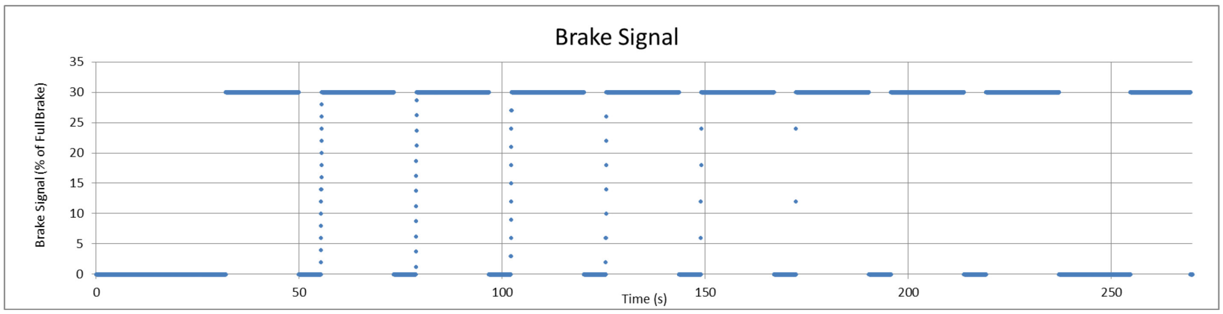

Figure V-9 Peak Battery Current For Varied Braking Torque Application Rates

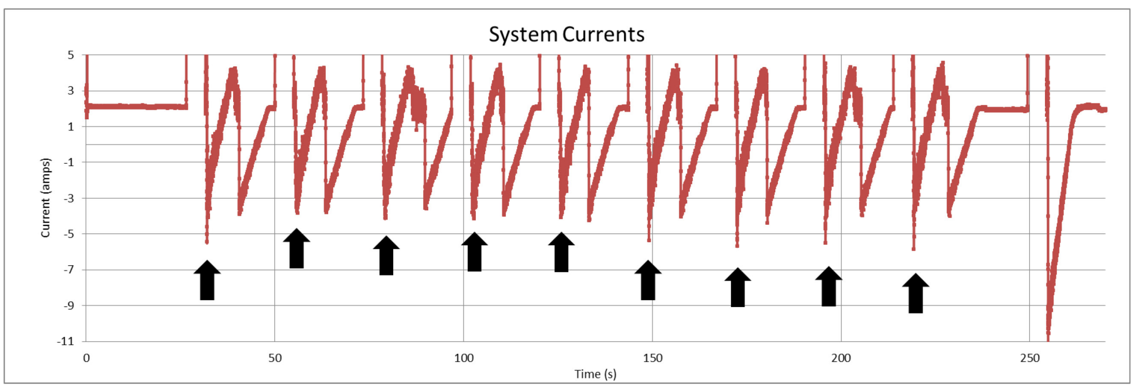

From these graphs it is readily apparent that faster braking torque application rates, unsurprisingly, require faster flywheel reactions in order for the peak regenerative braking current to be absorbed by the flywheel instead of the battery pack. More interestingly is that the flywheel is able to limit the current seen by the battery pack even if the brake is applied instantaneously (the first arrow), which is not physically possible for a human driver. The best results are achieved if the braking signal is applied over 300ms, and would likely improve further if ramped up to the final value over a longer period of time, but similarly good results are achieved over 150ms. More testing will need to be done to see the distribution of braking torque application rates demanded by a driver in real-world situations, but these preliminary results show good promise at rates that can reasonably be expected.

Flywheel Torque Application Rate

The flywheel, like any physical system, has a non-instantaneous response time due to the necessary time required for the system CAN messages to be both relayed and read, motor controller commands to be computed and initiated, and the system's inductance and inertia to be overcome. On the INSTAR prototype this was found to be about 100ms. The communication time overhead was found to be effectively fixed for our prototype system, but can be minimized in a production implementation. With this in mind, the controller was designed to work around this inherent delay in order to show it is not prohibitively long. Once the motor controller has the requested throttle signal it employs its own internal PID controller to provide the current to the stator windings. The coefficients on this controller, with its own rise time, overshoot, and settling time, are controlled by what Sevcon has named the "Torque Application Rate." This variable effectively trades faster rise time for larger overshoot, a classic trade-off when dealing with a PID controller. It controls how quickly the current is sent to the stator, and hence how quickly the flywheel reacts to the given signal.

This variable allows the INSTAR system's open loop controller to have a faster response time, which is useful for quickly absorbing the current during the large current spike seen during the first second of a regenerative braking event when the power demand is highest with the flywheel - not the battery. The control event is shown in Figure V-10and 5 subsequent tests with the same braking signal, but linearly decreasing torque application rates ranging from $\frac{150\%}{second}$ to $\frac{50\%}{second}$ are shown in Figure V-11.

Figure V-10 Control Braking Event

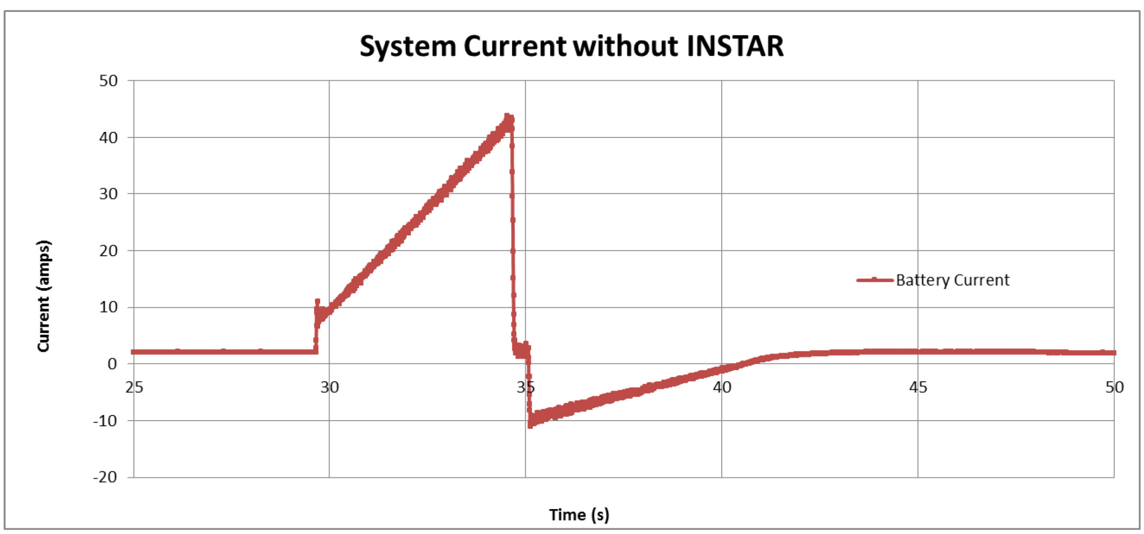

Figure V-11 System Current During Test with Varied Flywheel Torque Application Rates

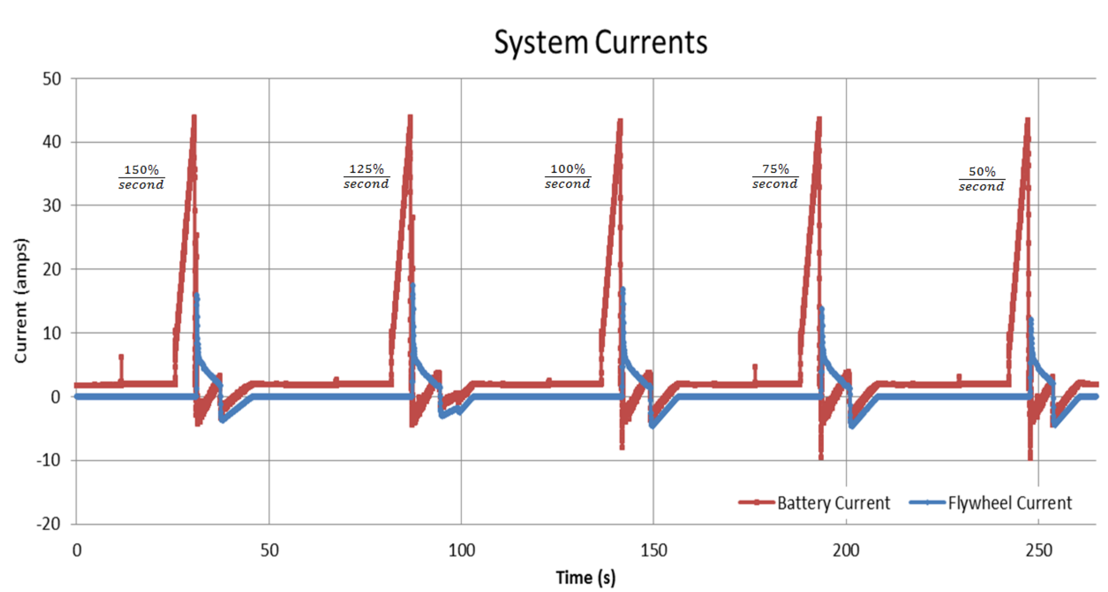

This figure demonstrates that higher torque application rates, implemented by the flywheel motor controller, allow the flywheel to react fast enough to absorb the high current so that the battery does not. Lower torque application rates react too slowly to keep the battery from seeing the large current spike, however brief that spike is. However, upon closer inspection there are trade-offs between the fast reaction time and absorbed current overshoot. Each of these peaks can be examined individually to see this more clearly.

Figure V-12 Flywheel Current Overshoot with Varied Torque Application Rates

a)

b)

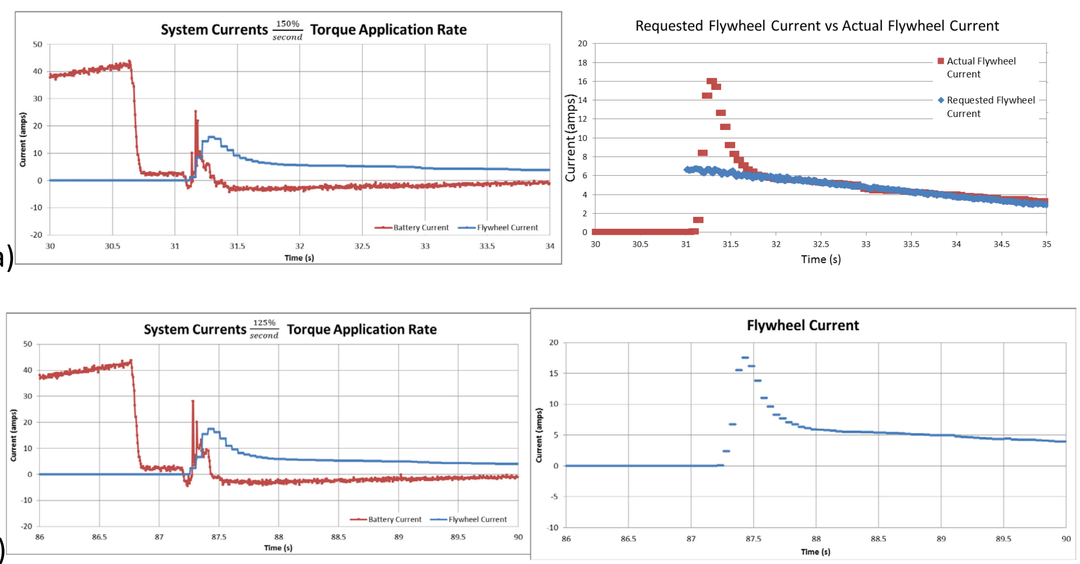

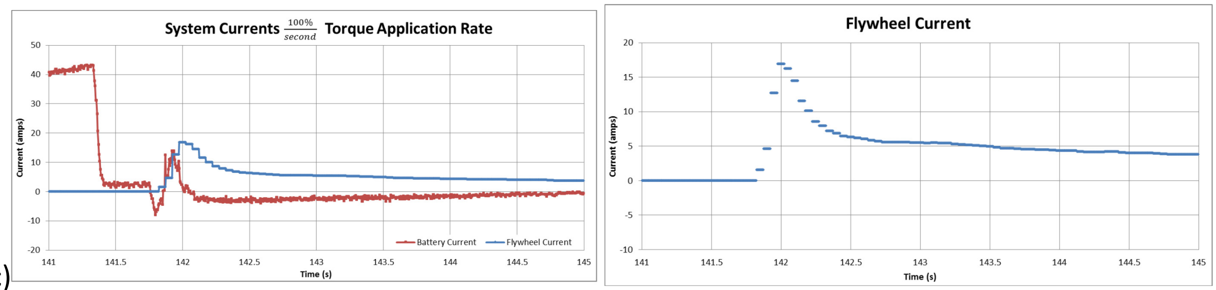

c)

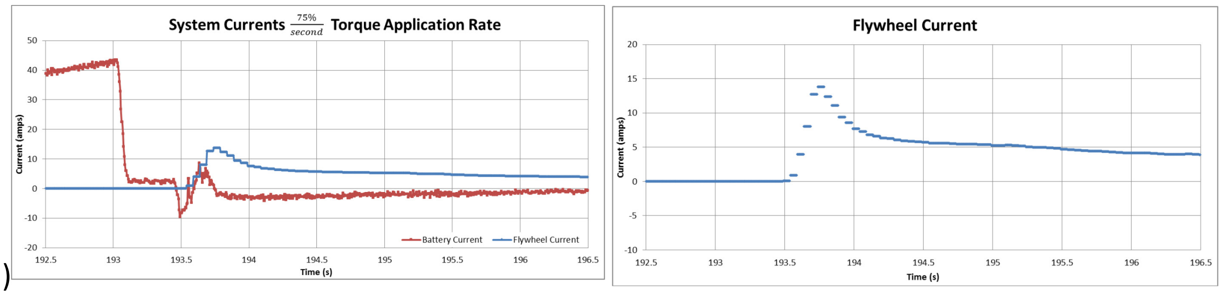

d)

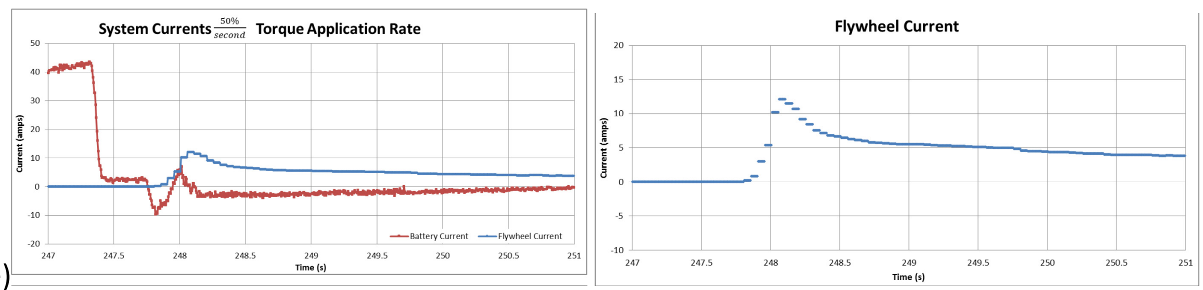

e)

Figure V-12a is labeled with both the requested current and the actual current. This figure clearly demonstrates that the motor controller current responds with a very classic controller overshoot. This flywheel absorption current, at least in this example, overshoots so far as to push the battery current positive, meaning that current is being drawn *from the batteries* to spin up the flywheel during braking. This is clearly an unwanted effect as any energy going into the flywheel from the batteries must be discounted by the flywheel's roundtrip efficiency. Ideally, only the current that the battery cannot absorb during braking should be absorbed by the flywheel, and any extra simply reduces the benefit of the INSTAR system. This overshoot, as expected, decreases as the torque application rate is decreased.

However, as can be seen in Figure V-12c and Figure V-12d, if the torque application rate is too low then the peak regenerative braking current seen by the batteries is allowed to develop before the flywheel can spin up and absorb it. These values demonstrate a much lower overshoot and just barely cause the flywheel to push the battery current positive, getting closer to the desired result of net-zero battery current during braking, but the peak still develops. There is clearly a trade-off with this implementation of the open-loop controller between the peak current to the batteries and total system efficiency. It should be noted that the torque application rate is also a controllable value, and can be changed in real-time via CAN. Future implementations may be able to include a dynamic torque application rate that has a high initial value to reduce the rise time, quickly followed by a lower torque application rate before the system can overshoot.

Coefficient Tuning

$$\text{Flywheel Throttle Signal} = F\left[\frac{\mathrm{A}(\mathrm{T_B}\cdot\omega_\mathrm{v}) - \mathrm{BT_B} + \mathrm{C}\omega_\mathrm{v}}{(\mathrm{D}\omega_\mathrm{f} + \mathrm{E})}\right]$$

The open loop controller's flywheel throttle signal calculation algorithm consists of three main parts: the numerator inside the brackets to calculate the predicted current generated by the traction motors based on the braking torque request and the real-time wheel speed during regenerative braking, the denominator inside the brackets to translate this current prediction into a flywheel throttle signal using the real-time flywheel, and a constant to scale the resulting signal. The numerator coefficients A, B and C were previously determined and discussed in the design of the open loop controller in Chapter III.

The denominator$(\mathrm{D}\omega_\mathrm{f} + \mathrm{E})$ and scaling factor F are coefficients that can be tuned in order to provide a larger, and/or faster, response in the current that is absorbed by the flywheel during regenerative braking. The relative magnitude of D compared to E has a significant effect on how quickly the flywheel responds, especially at zero speed ($\omega_\mathrm{f} = 0$) and low speed ($\omega_\mathrm{f} < 300\ RPM$). This is especially important since the flywheel is ideally at zero sped when a braking event is initiated. As the flywheel spins up from $\omega_\mathrm{f} = 0$, the denominator grows in magnitude and the overall flywheel throttle signal decreases, as it is inversely proportional to the denominator. The relative size of the initial value E, compared to the contribution from $\mathrm{D}\omega_\mathrm{f}$ determines how quickly the flywheel throttle signal decreases as the flywheel spins up from low ω_f to high ω_f. A small D:E ratio provides a flat flywheel response over its speed range as the contribution of E to the total denominator magnitude will dwarf the contribution of $\mathrm{D}\omega_\mathrm{f}$, at least until high speed. A small D:E ratio provides a very strong overall response at $\omega_\mathrm{f} = 0$ as the denominator is small, yet quickly grows as the flywheel spins up. This can be useful for providing a large initial flywheel throttle response in order to absorb the peak regenerative braking current that quickly diminishes in order to allow a secondary controller to contribute after the peak has been absorbed and current levels are below a safe battery charging threshold. Figure V-13 graphically explains this idea, where the D:E ratio moves the overall throttle signal to different areas of the inverse curve, graphically. A larger, although still less than 1, D:E ratio provides a steep drop off. Smaller and smaller ratios provide more moderate inverse drop offs and the smallest ratios provide a flatter, linear relationship.

Figure V-13 Throttle Response Shaping

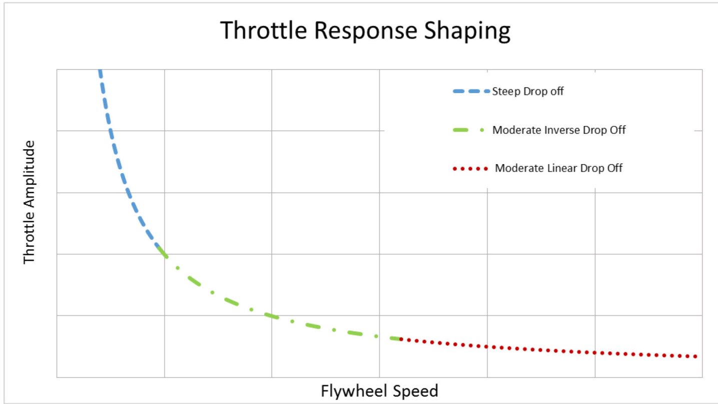

The scaling factor FF is comparatively straightforward; it linearly scales the overall signal magnitude once it has been shaped by the relative size of the other coefficients: A, B, C, D, and E.

Flywheel Initial Speed at the Braking Event Initiation

During testing it was found that the flywheel is able to absorb current much more quickly if it has non-zero speed at the initiation of a braking event, when the current absorption needs are largest and are generated in less than 100 ms after the braking signal is generated at the pedal. Figure V-14 shows the current seen by the battery pack during the same repeated braking event. The first peak is a control peak, without the INSTAR system, and the only difference in the following peaks is the initial flywheel speed at the beginning of the event, seen in Figure V-15. More research will have to be done to determine to causes of this, although it is suspected that it is due to the motor controller’s internal current control algorithm rather than due to something mechanical like stiction. Regardless, this shows promise for significantly reducing the flywheel’s reaction time, which is critical for absorbing the current peak generated at the initiation of a braking event. More research should be done to gauge the feasibility of designing a controller around this phenomenon and its effects on the system energy efficiency. A potential controller could keep the flywheel spinning continuously at a minimum speed necessary to reap the reaction time benefits, but the energy required to do so would be parasitic. It could, however be justified if braking events happen frequently, as in a delivery or garbage truck. The prototype flywheel only requires 1 amp (~100 watts) to maintain 500 RPM. There is also the potential to predict a braking event and “pre-charge” the flywheel to 500 RPM only before a braking event. A 100% accurate system would be difficult to implement, but false-positives could be tolerated if the batteries are sensitive to the peak charging currents and eliminating those peaks justifies the false-positive parasitic losses.

Figure V-14 System Current with Non-Zero Initial Flywheel Speeds

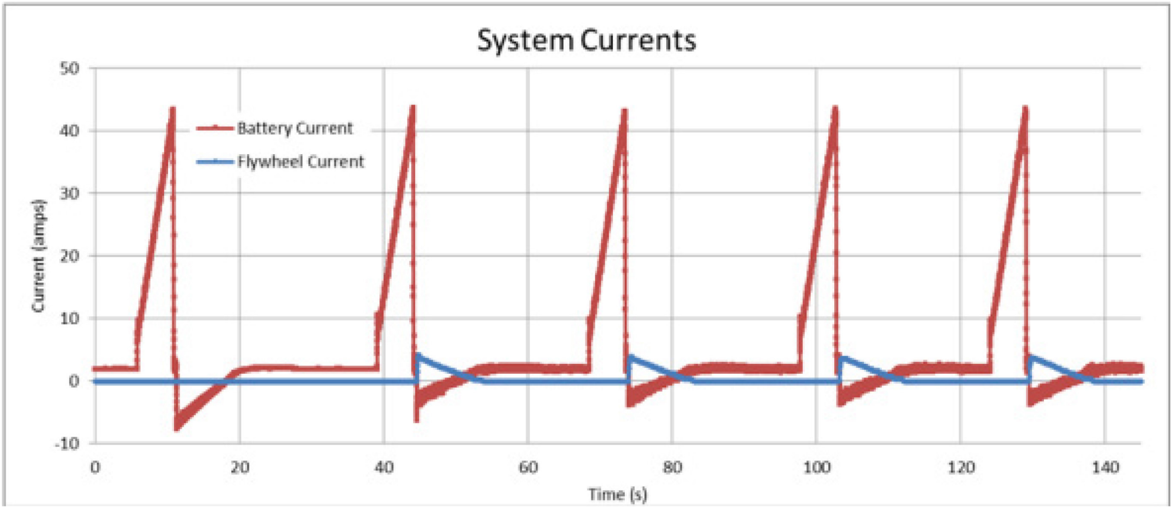

Figure V-15 Flywheel Speeds During Non-Zero Initial Speed Testing

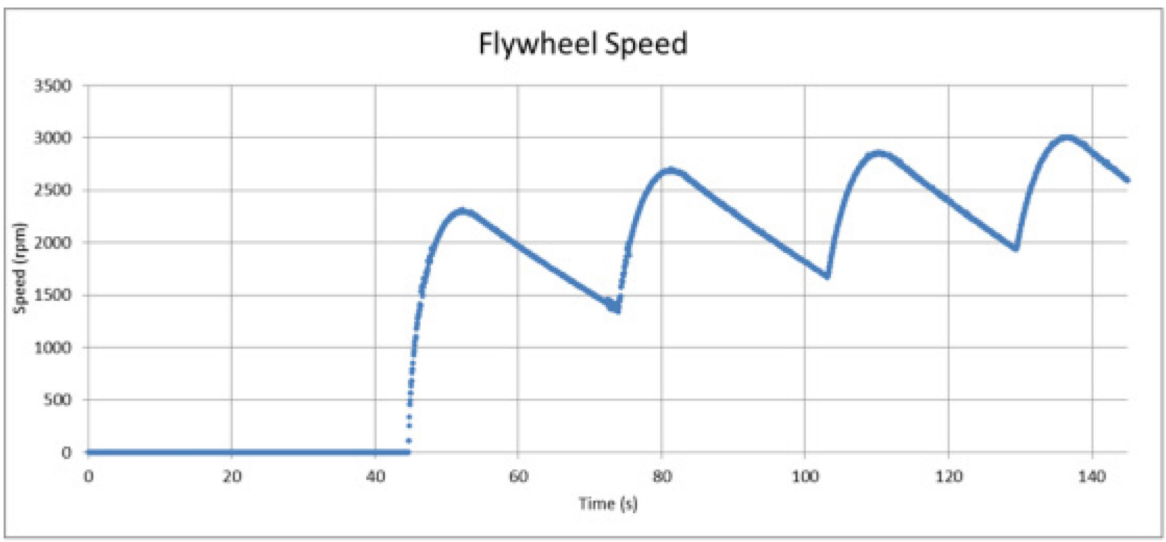

Section 5.03 Experimental Test Results

(a) Open Loop Controller Testing – Single Event

The four variables most useful for tuning the open loop controller discussed in the previous section are:

- The braking torque request rate
- The flywheel motor controller's torque application rate
- The open loop controller coefficients, and hence the resulting flywheel throttle in response to the observed instantaneous wheel speed braking torque request
- The flywheel speed at the initiation of a braking event

An example tuning for the go-kart electric vehicle testing platform, shown in Table V-1, was put through a series of tests to determine the energy and power flow in the system to gauge its performance. The flywheel initial speed was set to zero ($\omega_{f,t=0} = 0$) for all these tests as the work to implement non-zero flywheel initial speeds ($\omega_{f,t=0} > 0$) into the open loop algorithm is left to the continuing members of the INSTAR lab.

Table V-1 Open Loop Controller Testing Coefficients

Braking Torque Request Rate	Instant
Flywheel Torque Application Rate	$\frac{150\%}{second}$
$\omega_{f,t=0}$	0 RPM
Open Loop Controller Coefficients	
A	0.4
B	0.4
C	-0.12
D	0.4
E	2.7
F	2.1

Figure V-16 shows the vehicle speed and battery current during the control event, with the INSTAR system disabled. Figure V-17 shows the vehicle speed and resulting flywheel speed during the test with the INSTAR system enabled. Figure V-18 shows the associated flywheel current and battery current.

Figure V-16 Vehicle Speed and Battery Current During Control Event

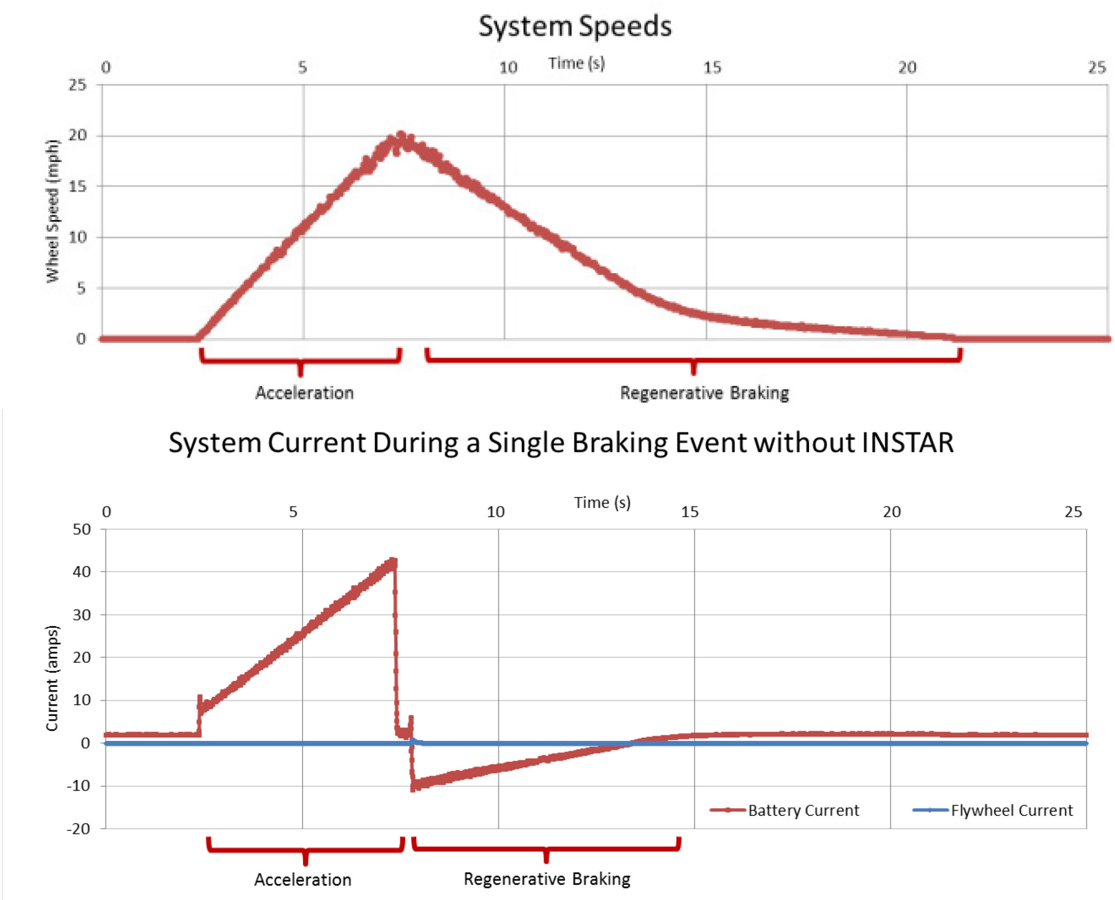

Figure V-17 System Speeds During Single Braking Event Test

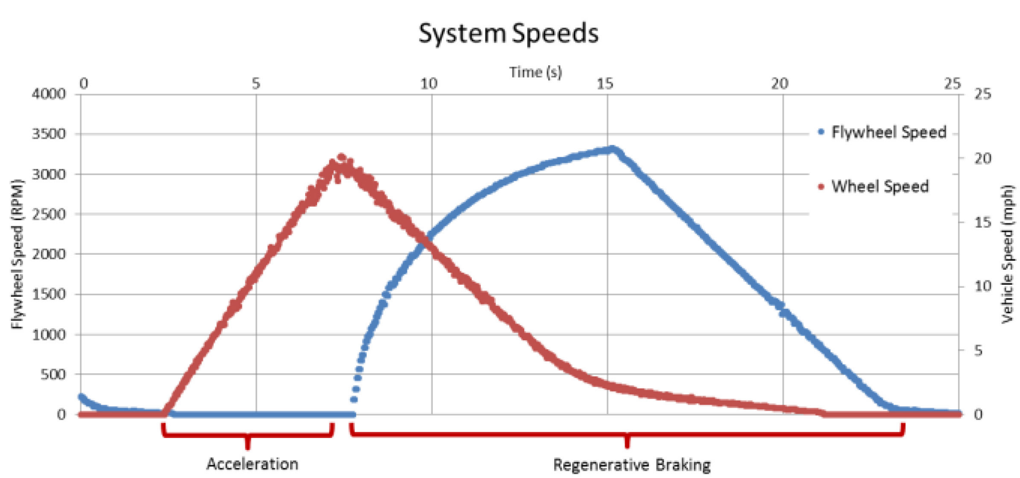

Figure V-18 System Currents During Single Braking Event Open Loop Controller Testing

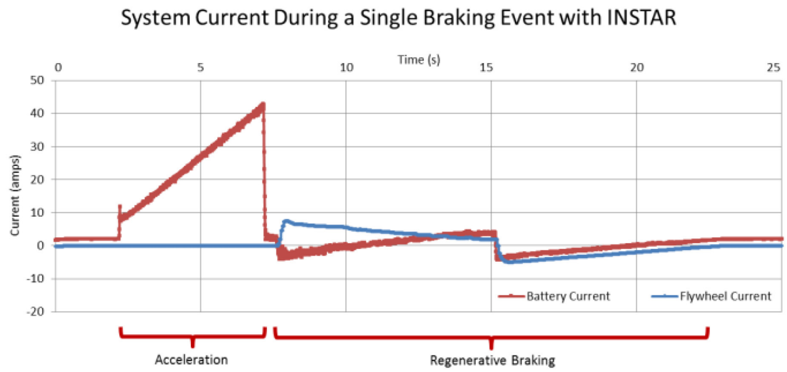

Analysis of this single braking event demonstrates that the open loop controller exhibits two main, desired features. It reacts fast enough to reduce the current seen by the battery pack and is able to correctly shape the current absorbed by the flywheel into a linearly decreasing profile, following the vehicle speed. It also exhibits an excessive flywheel current at low vehicle speed, pulling the battery current positive when it should be zero. This means that the flywheel throttle signal at high speed (ω_f) is too high and is accelerating the flywheel with energy from the battery when it should have ceased accelerating when the regenerative braking current hit zero. This is a result of the open loop controller's algorithm denominator coefficients D and E, discussed in Chapter III, being improperly tuned. The controller tuning exhibits good low speed reaction time, but at high speed it does not reduce the throttle signal to low enough levels. This causes the flywheel motor controller to continue to accelerate the flywheel and pull the entire system current positive, essentially wasting energy.

The energy used during the control event is shown in Figure V-19. The energy used during the same braking event, but with the INSTAR system enabled is shown in Figure V-20. The quadratic rise in energy at the beginning of each test is due to the linear increase in vehicle speed and in both tests this energy peaks when the vehicle begins to coast at $t = 7.5$ seconds. For ease of comparison it was designed that the energy used to reach the peak vehicle speed be the same for both tests for comparison, and this indeed holds true.

However, the two test results are, by design, quite different during braking. The first thing to note is that the two systems (with and without the flywheel) capture the braking energy over two significantly different time spans. The major problem facing a battery-only system is that the system attempts to capture all the kinetic energy of the vehicle during the time it takes the vehicle to come to a stop, which for modern vehicles is quite short, on the order of 1-3 seconds for many events. This results in a high charging power, which is energy per unit time, and is graphically represented as the slope of the line in Figure V-19 and Figure V-20. The INSTAR system decouples the energy capture time from the braking event time, allowing it to be absorbed by the batteries over a much longer time, and hence at comparatively lower power levels. Figure V-20 clearly demonstrates this through its longer and more gradual regenerative braking region.

Figure V-19 Cumulative Energy Consumed During Braking Event - Control

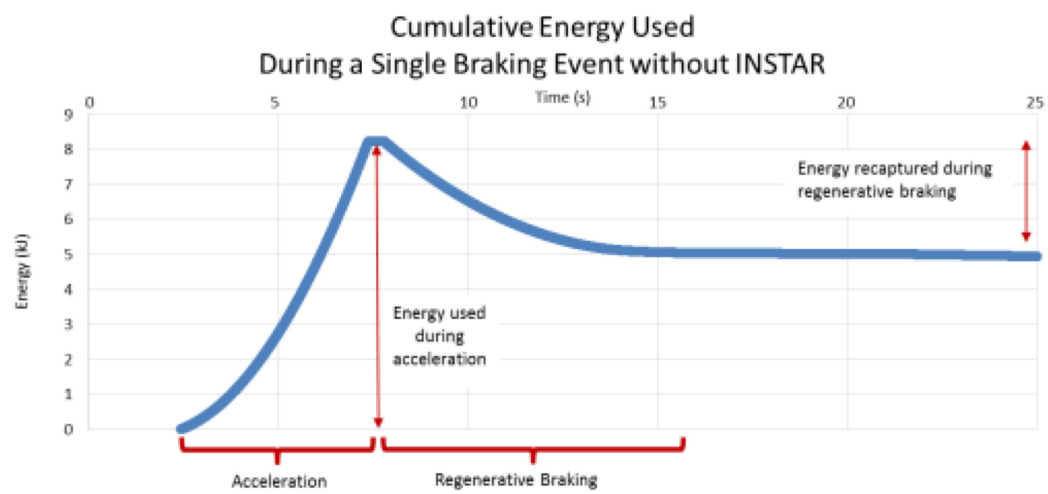

Figure V-20 Cumulative Energy Consumed During Braking Event - INSTAR

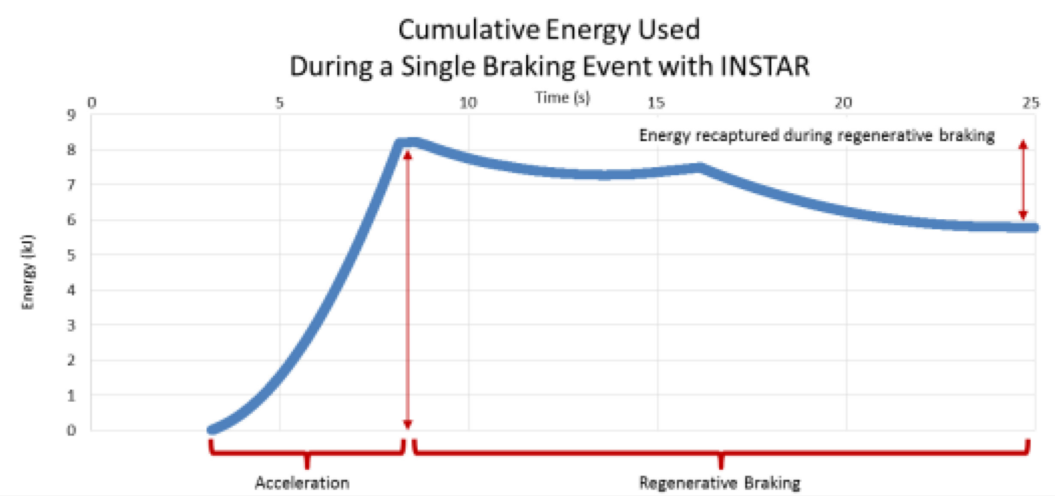

The second thing to note is that the regenerative braking with the INSTAR system can be visually separated into two convex regions. The first region occurs during active vehicle braking, when the flywheel is accelerating to absorb the current normally seen by the battery. The second region occurs when the flywheel starts regeneratively braking, feeding its stored energy back to the batteries at its pre-determined, low battery stress, level. Figure V-21 shows the where this transition occurs on the two graphs.

Figure V-21 Cumulative Energy Consumed with Respective Vehicle Speed

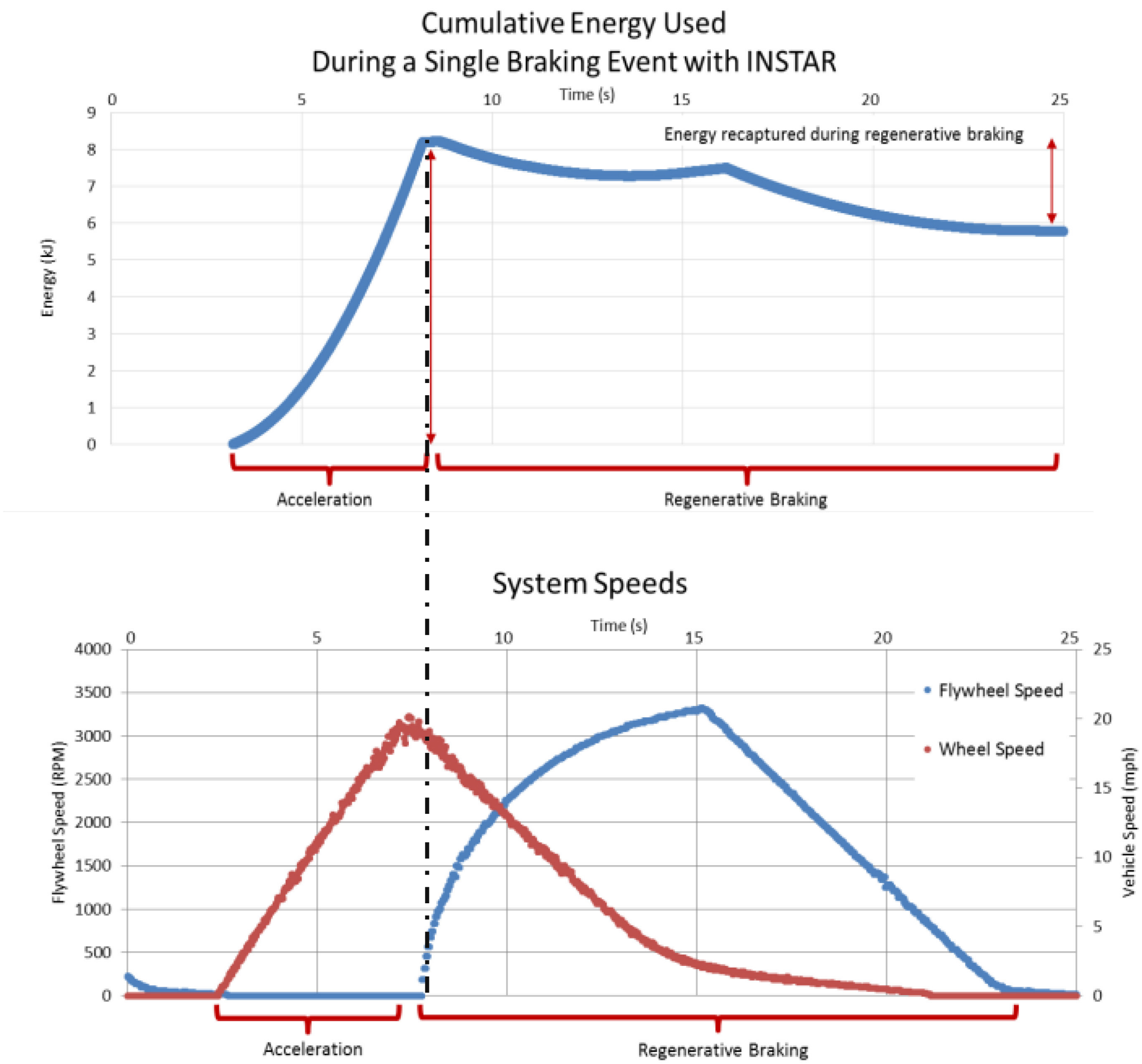

Ideally, this curve would be monotonically decreasing during regenerative braking as energy should only be flowing into the battery. However, as described earlier, the open loop controller tuning for this test has an undesired overshoot at high flywheel speeds, which caused energy to be pulled from the battery pack to spin up the flywheel. This energy is clearly seen in Figure V-20 and Figure V-21 as the rise in energy spent by the batteries right before the flywheel begins feeding its stored energy back to the battery pack.

The last, and main, thing to see from these charts is the total energy used over the entirety of the test. This shows how much of the energy expended during acceleration can be recaptured and hence how efficient the braking system is overall. Table V-2compares the energy and current values for these two tests.

Table V-2 Summary of Energy Consumed – Single Event

	Energy Consumed During Acceleration (kJ)	**Energy Recaptured (kJ)**	**Peak Charging Current (Amps)**	**Net Energy Used (kJ)**	**Overall Braking Efficiency**
Control	8.2	3.2	23.7	5.0	39%
INSTAR	8.2	2.4	11.7	5.8	29%

The control event was able to capture more energy than the INSTAR system test, but at higher current and power as seen in Figure V-19. While the battery pack is safely able to handle *this* level of charging current, higher levels of current, seen during braking events with higher torque and/or higher initial speed, should not be absorbed by the pack. This will be discussed further in Section 5.04.

(b) Open Loop Controller Testing – Driving Profile

A more rigorous test that includes multiple, varied braking events was designed to better understand the behavior and performance of the INSTAR open loop controller. This test includes braking events with varied:

- initial vehicle speeds at the braking event initiation [mph]
- requested braking torques [Nm]
- braking torque request rates [Nm/s]
- instantaneously (events 1 and 9)
- up to 300 ms (event 2)
- non-constant braking torques with varied braking torque change rates [Nm]
- Strong initial torque request quickly followed by a lower request (event 4)
- Low initial torque request quickly followed by a larger request (event 5)
- Strong initial torque request, quickly followed by a brief period of zero torque request, quickly followed by the same initial torque request (event 8)

The braking signal generated for this test is shown in Figure V-22 and the vehicle speed over the course of the test is shown in Figure V-23. The exact profile, with each brake and throttle signal given in 10ms increments, is included in Appendix D.

Figure V-22 Braking Signal During Test Driving Profile

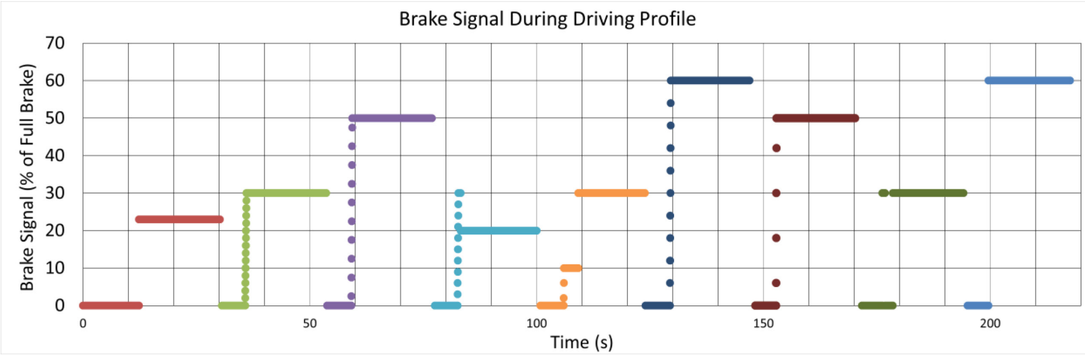

Figure V-23 Vehicle Speed During Test Driving Profile

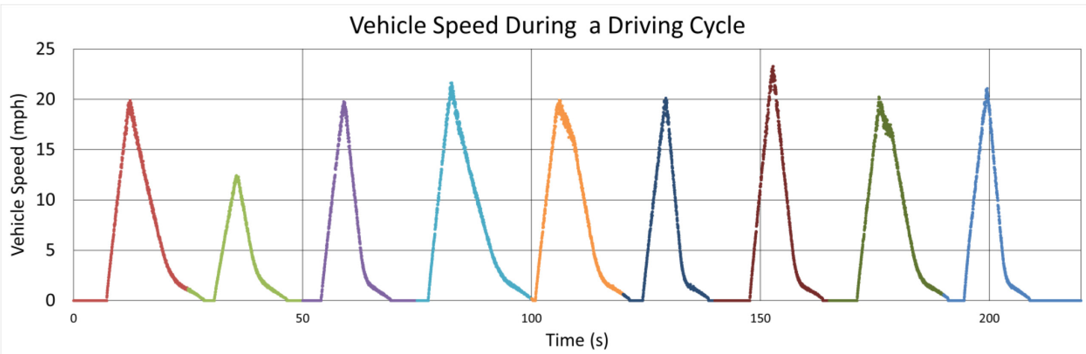

This test driving profile results in the following control current profile. Without the INSTAR system, the battery pack sees peak currents around 20 amps. The largest current peaks are seen from events 6, 7, and 9. These events combine both larger initial speed and/or larger braking torques.

Figure V-24 Battery Current During Test Driving Cycle

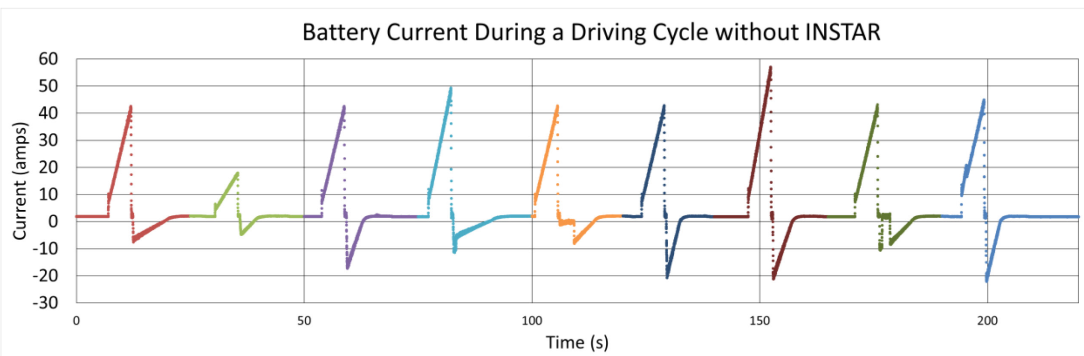

(c) Open Loop Controller Testing – Driving Profile Test Results

As described earlier in Chapter III, the open loop controller is able to accurately predict the current generated in each of these events. The controller then takes this prediction and translates it into a flywheel throttle signal using the same settings as the single braking event test, described earlier in Table V-3. These settings are repeated here for convenience.

$$\text{Flywheel Throttle Signal} = F\left[\frac{\mathrm{A}(\mathrm{T_B}\cdot\omega_\mathrm{v}) - \mathrm{BT_B} + \mathrm{C}\omega_\mathrm{v}}{(\mathrm{D}\omega_\mathrm{f} + \mathrm{E})}\right]$$

Table V-3 Open Loop Controller Tuning During Testing

Braking Torque Request Rate	Varied (see Figure V-22)
Flywheel Torque Application Rate	$\frac{150\%}{second}$
$\omega_{f,t=0}$	0 RPM
Open Loop Controller Coefficients	
A	0.4
B	0.4
C	-0.12
D	0.4
E	2.7
F	2.1

The comparative battery current profile for this driving cycle is shown in Figure V-25. It shows the battery current from the control event shown above in Figure V-24 and the resulting battery current with the INSTAR system enabled. It clearly shows that the INSTAR system is able to keep the battery charge current at a lower level than the control cycle. It is able to react fast enough to absorb some of the peak charge current and avoid having the battery pack see the full brunt of the regenerative braking charge current. The other major thing to note is that the flywheel absorption current overshoot seen in the single braking event testing described earlier, and for the same reasons, is more noticeable here with larger braking events.

Figure V-25 Comparative Battery Current During Driving Profile

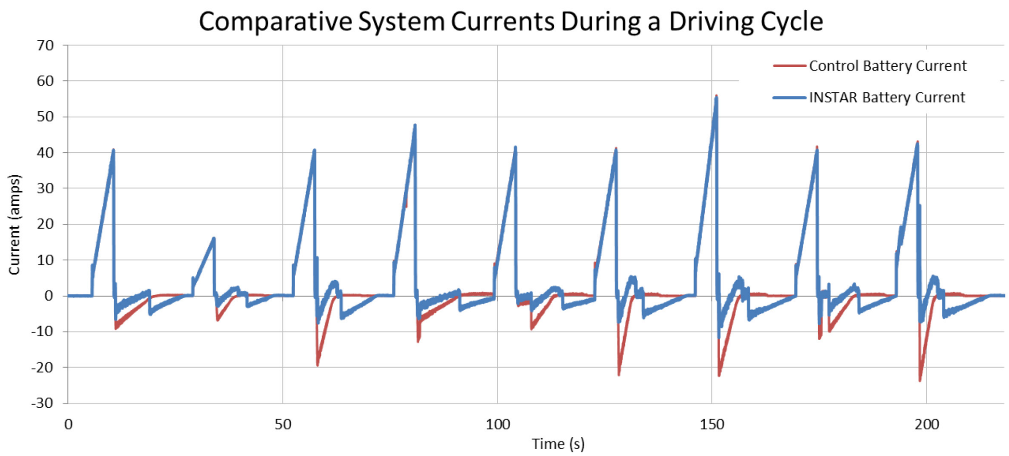

This high flywheel-speed current absorption overshoot can also be seen when the INSTAR battery current data series is isolated and split into its components. Figure V-26 shows the current flowing into and out of the flywheel overlaid on to the battery current. This battery current can be thought of as the sum of the control event current shown in Figure V-24 and the flywheel current shown in Figure V-26.

Figure V-26 INSTAR System Current During Driving Profile

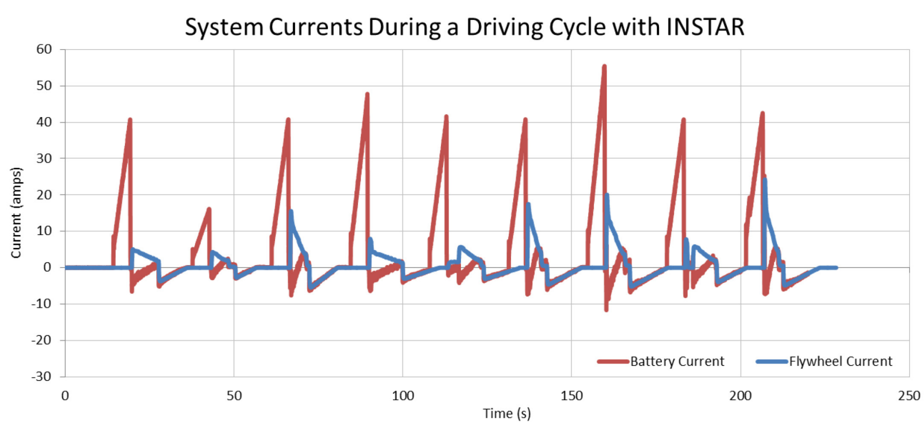

This overshoot, just as in the single braking event testing, leads to unnecessary energy flowing from the battery pack into the flywheel. The net result of this is below optimal energy efficiency, which is the goal of the INSTAR system addition. It is important to understand how this current control inefficiency affects the overall system efficiency. Figure V-27 integrates the power flow into and out of the battery to understand how much energy is used during acceleration and how much energy is captured during regenerative braking. Just as in the single event testing, the acceleration energy is identical for both the control and INSTAR tests, so the only difference lies in how much energy is recaptured during braking, and at what instantaneous power levels it is captured at.

Figure V-27 Comparative Energy Consumption During Driving Profile

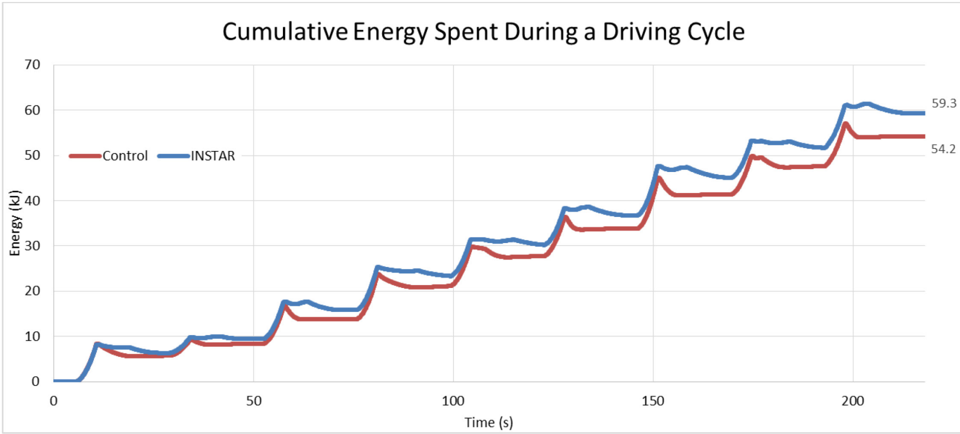

From this figure it is clear that the control event uses less energy over the course of the driving cycle, and this should come as no surprise. This test assumes that the batteries can handle even the largest charging currents, and hence provides them with the maximum available regenerative braking current. In comparison, the flywheel uses 9.4% *more* energy, but at lower peak currents. The major results of this test are provided in Table V-4.

Table V-4 Summary of Driving Profile Comparative Energy Consumption

	Energy Consumed Over Cycle (kJ)	**Peak Charging Current (Amps)**	**Net Difference (kJ)**
Control	54.2	23.7	--
INSTAR	59.3	11.7	+4.9 (9.4%)

Section 5.04 Analysis of Experimental Test Results

Rather than only comparing the INSTAR results with the control test results, it is telling to see how the INSTAR system compares to a system with a lower, limited battery charge current. This is more similar to the situation in current hybrid vehicles where the regenerative braking is limited [NREL REF]. This limiting can be done for thermal or lifetime capacity management [NREL REF], but either way the result is a protected battery pack that leaves potentially recaptured energy on the table, so to speak. The flywheel system can then be compared to a capped battery current situation for a more accurate comparison between the status quo and a vehicle implemented with the INSTAR system. This comparison scenario is first demonstrated for a single braking event, as described earlier in Section 5.01.

Figure V-28 compares the battery current during the control test, the INSTAR-enabled test, and a theoretically capped test. The capped event uses the same data set as the control event, but *artificially* limits it to the max charging current seen with the INSTAR system for purely comparative purposes. Figure V-29 shows the cumulative energy used during these tests.

Figure V-28 Comparative Battery Current – Single Event

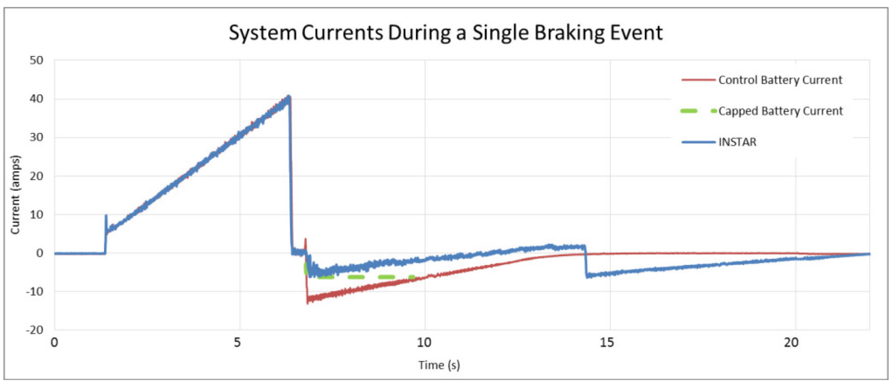

Figure V-29 Comparative Energy Consumption - Single Event

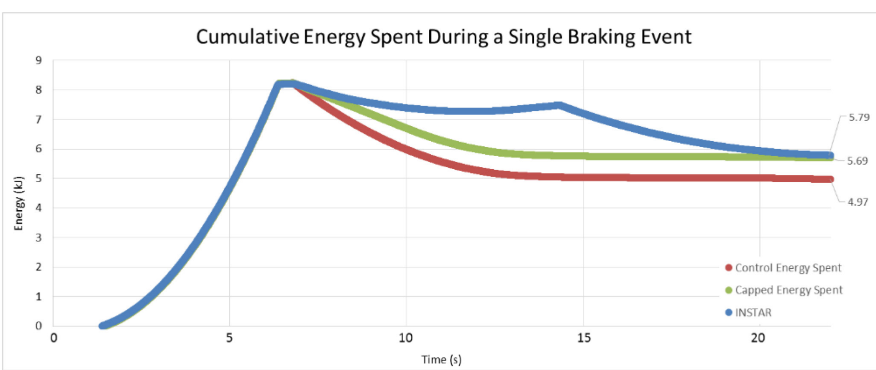

Despite the open loop controller having overshoot at the tail end of the test, shown in Figure V-28Figure V-30 and Figure V-29 and highlighted in Figure V-30 and Figure V-31, the capped test and the INSTAR test end up with essentially identical cumulative energy use. Even with the flywheel pulling energy from the battery, only to be put right back into the battery, the INSTAR test regenerates roughly the same amount for this test. Table V-5 summarizes this information.

Figure V-30 Open Loop Controller Current Overshoot

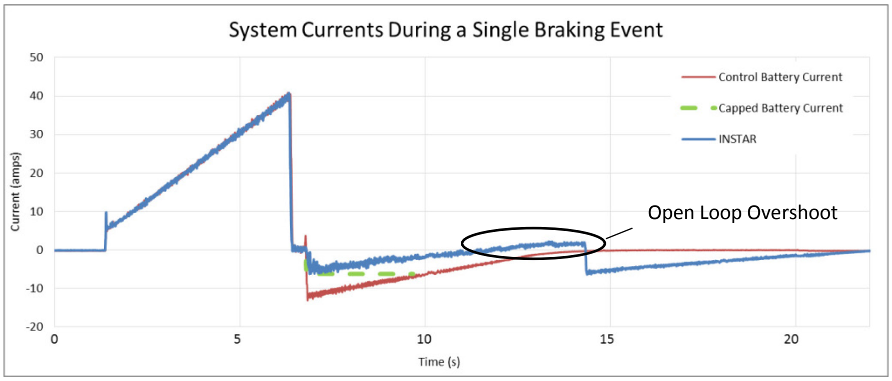

Figure V-31 Energy Consumption Effect of Open Loop Controller Overshoot

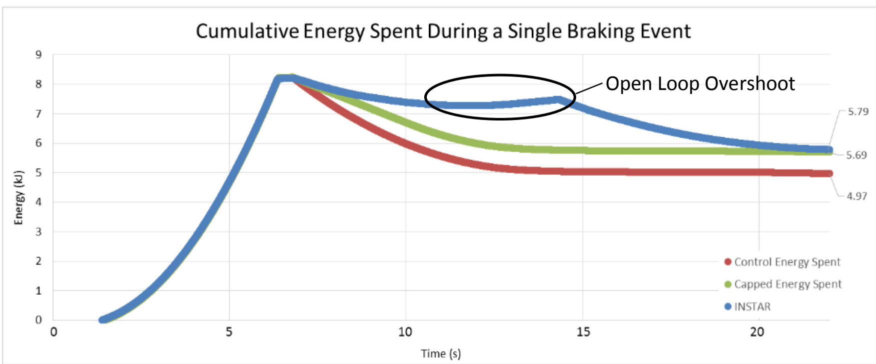

Table V-5 Summary Comparison – Single Event

	Energy Consumed During Acceleration (kJ)	Energy Recaptured (kJ)	Peak Charging Current (Amps)	Net Energy Used (kJ)	Overall Braking Efficiency
Control	8.2	3.2	13.8	5.0	39%
INSTAR	8.2	2.4	6.2	5.8	29%
Capped	8.2	2.5	6.2	5.7	30%

The same type of comparison was done for the same driving cycle described in Chapter V. This allows for the differences between the three scenarios: control, capped, and INSTAR, to become more exaggerated over the roughly 4 minute test. Again the capped current is limited to the maximum charge current seen during the INSTAR test. This 11.8 amp current was only briefly reached at the beginning of the 7th braking event, but was chosen to be informational on the current performance of the INSTAR system and not to attempt to exaggerate its usefulness. Other capped values can certainly be examined and the raw data files necessary for such examinations are included in Appendix B.

Figure V-32 and Figure V-33 contain the test results from this driving cycle test. Here the effects of the open loop controller overshoot are much more pronounced and again the control event uses the least amount of energy, but also puts the most stress on the battery pack. The capped event puts less stress on the pack, and hence uses more total energy over the course of the test, but less than the INSTAR test. Table V-6 summarizes the information from these two figures.

Figure V-32 Comparative Battery Current- Driving Profile

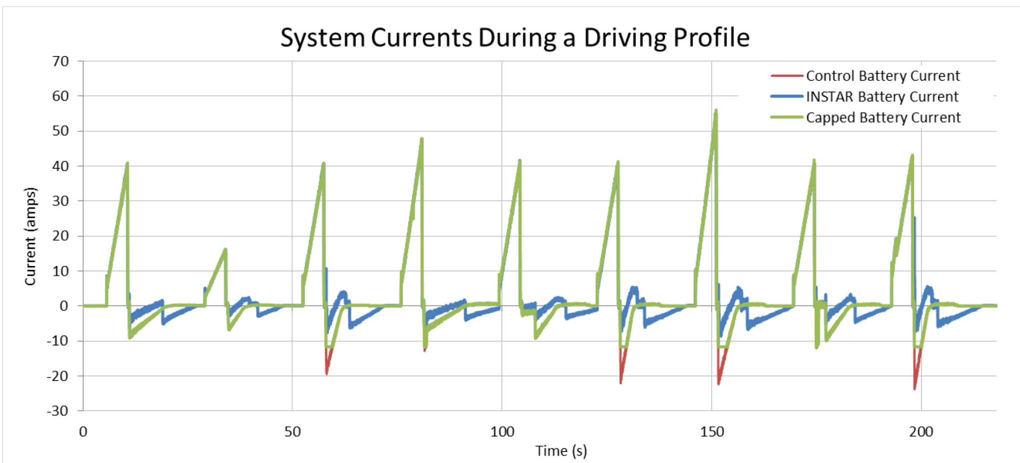

Figure V-33 Comparative Energy Consumption- Driving Profile

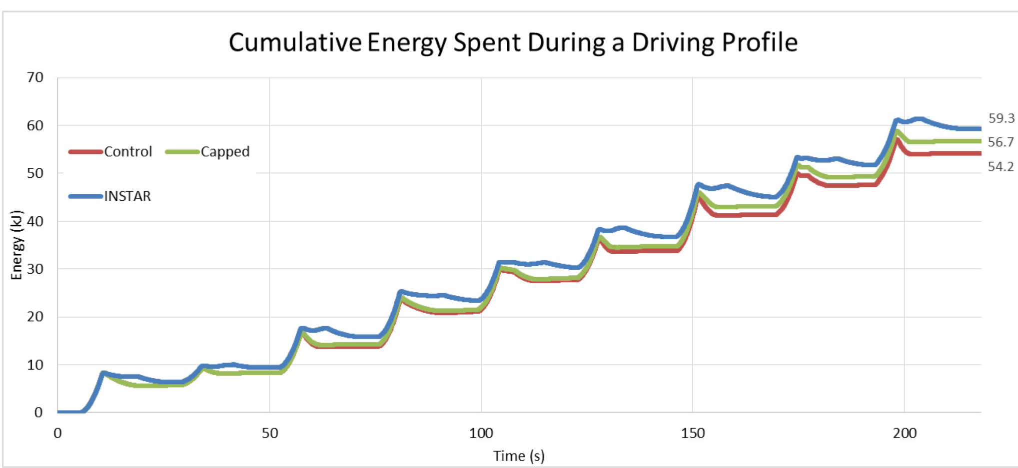

Table V-6 Summary Comparison – Driving Profile

	Peak Charging Current (Amps)	Net Energy Used (kJ)	Difference
Control	23.8	54.2	--
INSTAR	11.7	56.7	4.6%
Capped	11.7	59.3	9.4%

Despite the total energy consumed over the course of these tests being larger with the INSTAR system, the test results from this initial implementation of the INSTAR system are promising for one main reason - the system, with just the open loop controller, is able to react quickly enough to avoid using the battery pack to absorb the largest charging currents seen at the initiation of the braking event. This is accomplished through the open loop controller's reliance on the exact same braking signal that initiates the regenerative braking current. However, the overshoot of the flywheel current absorption at the tail end of the braking event as a result of the controller settings that are capable of this quick response is far from ideal. It results in unnecessary energy being pulled from the batteries to accelerate the flywheel. This energy will, of course, be put back into the drive motors or the batteries so it is not completely, but it is subject to the inefficiencies of the flywheel system in both directions, in and out. It is far better to never have this energy leave the battery pack in the first place.

Section 5.05 Potential Improvements

I believe the INSTAR controller can easily be improved to eliminate this overshoot entirely. It must be emphasized that this is merely the *initial* INSTAR controller. The open loop controller can be implemented as the feed-forward component of a more complex feedback controller. A combination of the quickly responding open loop controller with a flexible, tunable feedback-based controller can not only eliminate the overshoot, but can bring the overall response closer to the ideal response that allows the maximum amount of safe charging current to the battery and only absorbs the excess with the flywheel. Again, this allows for the flywheel size and/or speed to be minimized for higher energy density and/or lower cost.

The test data collected on the prototype go-kart test platform can be used to give an idea of how the system can perform with an improved controller. Rather than comparing the control event and capped event to the current implementation of the INSTAR system, they can be compared to a feasible *future* controller. The following analysis is done on *potential* improvements, and it should not be confused for actual results. These graphs, however, are meant to convey very possible future test results without much added development effort. It is meant to motivate continued interest in this work and discuss its potential for improvement. Current, and future, INSTAR lab members will continue working towards achieving these (and better) future results.

Potential gains can be analyzed by looking at one specific braking event, and Figure V-34highlights one of the relatively large braking events from the driving cycle discussed in Chapter V and summarized in Table V-7 that will be used. Feasible, future results are compared to the control event, two capped events with different maximum allowed battery charging currents, and the existing INSTAR implementation.

Figure V-34 Comparison Event in Context

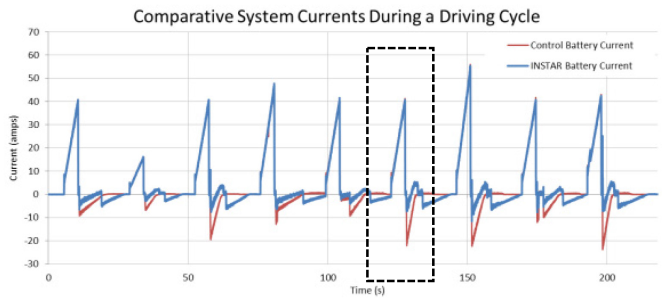

Table V-7 Summary of Comparison Event

Vehicle Speed at Brake Initiation	20 MPH (8.9 mm/s)
Brake Application Rate	0-Full in 200 ms
Brake Signal Magnitude	60% of Full Brake
Max Charging Current Seen	22.1 amps without INSTAR

The control and INSTAR test are taken from raw data collected with the go-kart during the 6th braking event of this driving cycle. The capped tests are, again, an artificially modified subset of the control event, with the charge current capped at the maximum charge current of 5 amps (C/8) and 11.6A (C/3.4). The battery current in all four scenarios are shown together in Figure V-35.

Figure V-35 Battery Current Comparison – Single Event

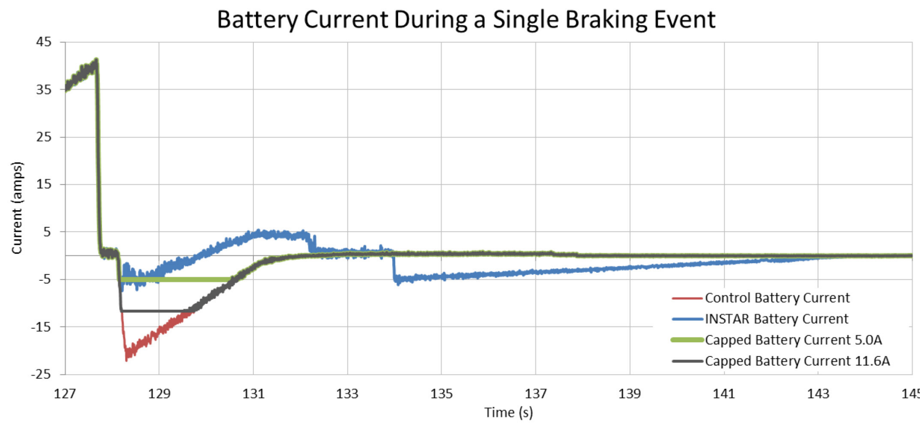

The INSTAR test is able to bring the max charging current well below the levels seen during the control event, 6.1 amps (C/6.5) for the INSTAR test and 22.1 amps (C/1.8) for the control test. The overshoot is again clearly seen as well. The more interesting part of this analysis is seen when comparing the energy recaptured over the course of this event. All four scenarios are again plotted together and are shown in Figure V-36. Both Figure V-35 and Figure V-36 are summarized in Table V-8.

Figure V-36 Energy Consumption Comparison –Single Event

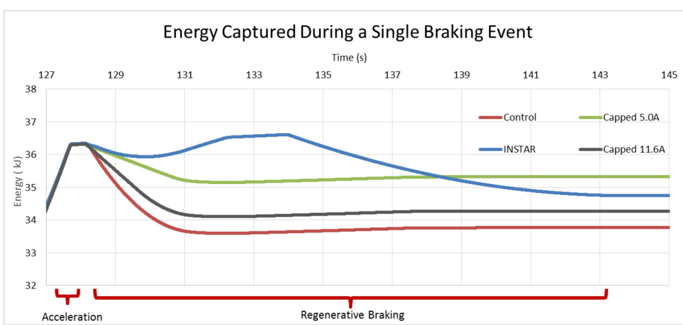

Table V-8 Summary Comparison – Single Event

	Energy Used Before Acceleration* (kJ)	Energy at Brake Event Initiation (kJ)	Energy After Brake Event (kJ)	Energy Used to Accelerate (kJ)	Energy Recaptured (kJ)	Peak Charging Current (Amps)	Net Energy Used (kJ)	Overall Braking Efficiency
Control*	27.7	36.3	33.8	8.6	2.6	22.1	6.0	29.9%
Capped†	27.7	36.3	35.3	8.6	1.0	5.0	7.6	11.5%
Capped†	27.7	36.3	34.3	8.6	2.0	11.6	6.6	23.7%
INSTAR*	28.2	36.3	34.7	8.1	1.6	6.1	6.5	19.6%

*at time t=122.725s not shown on graph, but included in Appendix B.

The control event again recaptures the largest amount of energy as it merely puts as large of a charging current necessary on the battery to fulfill the braking torque request, regardless of the battery pack health effects. The INSTAR test is sandwiched by the two capped tests, both in energy recaptured and maximum battery pack charging current. The INSTAR test recaptures less energy than the 11.6 amp test, but more than the 5 amp test. The INSTAR test itself has a maximum battery charging current of 6.1 amps. While it may seem that progressively higher charging currents allow for progressively more energy to be captured, the removal of the overshoot on the INSTAR test, seen as the 2nd upward slope and plateau in Figure V-36, has the ability to buck this trend and show that more energy can be recaptured, and at lower charging currents if the controlled can be properly tuned.

Improving the INSTAR controller such that the overshoot is eliminated would result in a current profile as shown in Figure V-37. In this scenario the flywheel stops accelerating and absorbing energy when the battery current reaches zero current. This would eliminate the positively sloped portion of Figure V-36 as well, instead having it be a horizontal line until the battery can handle the recharge current that the flywheel is waiting to supply. This is shown in Figure V-38.

Figure V-37 Battery Current Comparison – with Improvement

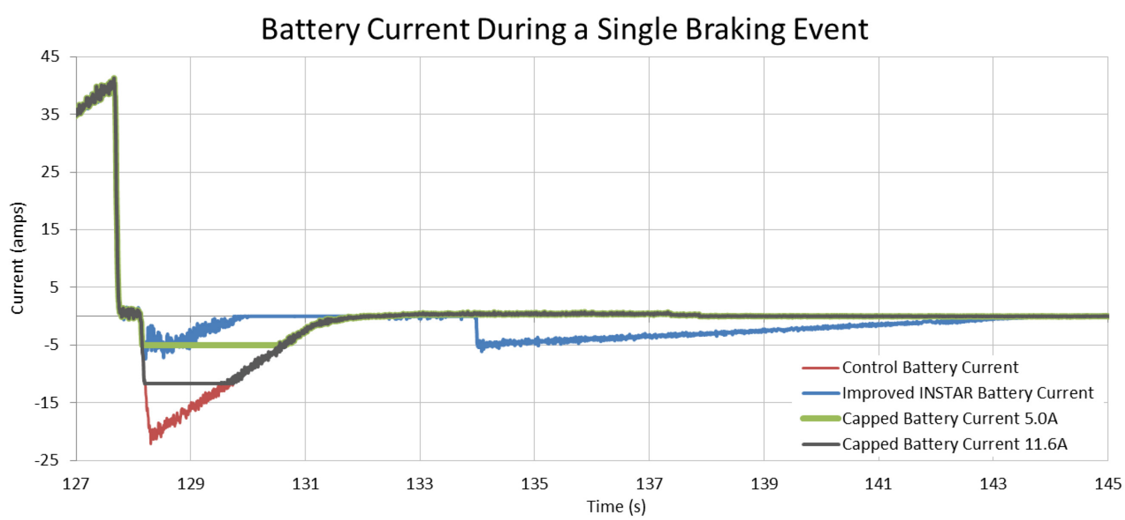

Figure V-38 Energy Consumption Comparison – with Improvement

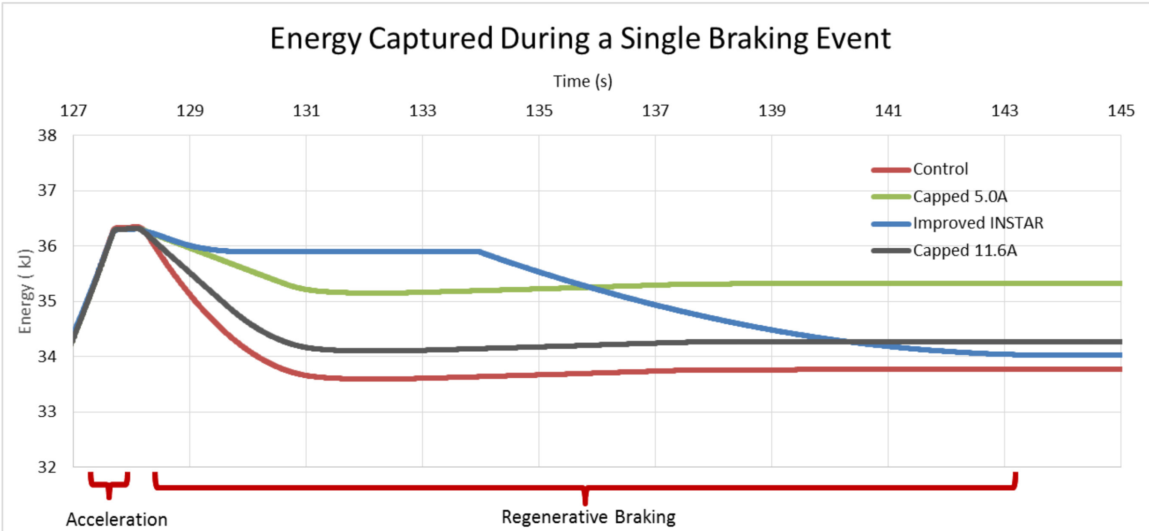

The ending energy values of Figure V-38 must be modified to account for the energy that the flywheel absorbed during the overshoot, and hence that is why those values aren't labeled on the graph. This is done by integrating the power during the overshoot to calculate how much was absorbed, then discounting 70% of this energy and adding it back to the final total. It still ends below both capped tests. The 70% discount is for a typical regenerative braking efficiency found during flywheel testing and described in Chapter IV. These modified values are listed in Table V-9 which summarizes and compares all five scenarios, both real* and artificial†, for this single event.

Table V-9 Summary of Energy Consumption Comparison

	Energy Used Before Acceleration (kJ)	**Energy at Brake Event Initiation (kJ)**	**Energy After Brake Event (kJ)**	**Energy Used to Accelerate (kJ)**	**Energy Recaptured (kJ)**	**Peak Charging Current (Amps)**	**Net Energy Used (kJ)**	**Overall Braking Efficiency**
Control*	27.7	36.3	33.8	8.6	2.6	22.1	6.0	29.9%
Capped†	27.7	36.3	35.3	8.6	1.0	5.0	7.6	11.5%
Capped†	27.7	36.3	34.3	8.6	2.0	11.7	6.6	23.7%
INSTAR*	28.2	36.3	34.7	8.1	1.6	6.1	6.5	19.6%
INSTAR Improved†	28.2	36.3	34.2	8.1	2.1	6.1	5.9	26.4%

Chapter VI. Conclusion

From these results it should be clear that the system holds a lot of promise for improving the regenerative braking of hybrid vehicles where battery charging currents are a concern. With feasible improvements the INSTAR system can capture more energy, and at lower charging currents, than an existing system with capped regenerative braking capabilities.

The design, based on cost-effective materials, commodity components, and an off-the-shelf motor controller, also shows much promise. While the necessity of a vacuum system needs to be further investigated, especially on a larger system, the remainder of the components held up well to testing and analysis.

References

[1] D. Greene, "Reducing Greenhouse Gas Emissions from U.S. Transportation," Pew Center on Global Climate Change, 2011.

[2] Environmental Protection Agency, "Inventory of U.S. Greenhouse Gas Emissions and Sinks: 1990-2013," EPA, Washington, DC, 2015.

[3] International Energy Agency, "CO2 Emissions from Combustion Fuel," EIA, Paris, 2012.

[4] J. Miller, Propulsion System for Hybrid Vehicles, London: Institution of Engineering and Technology, 2011.

[5] S. S. Choi and H. S. Lim, "Factors that affect cycle-life and possible degradation mechanisms of a Li-ion cell based on LiCoO2," *Journal of Power Sources,* vol. 111, no. 1, pp. 130-136, 2002.

[6] G. Ning and B. Haran, "Capacity fade study of lithium-ion batteries cycled at high discharge rates," *Journal of Power Sources,* vol. 117, no. 1-2, pp. 160-169, 2003.

[7] J. Shim, "Electrochemical analysis for cycle performance and capacity fading of a lithium-ion battery cycled at elevated temperature," *Journal of Power Sources,* vol. 112, no. 1, pp. 222-230, 2002.

[8] K. Kelly and A. Rajogopalan, "Benchmarking of OEM Hybrid Electric Vehicles at NREL," NREL, Golden, 2001.

[9] S. Holm and H. Polinder, "A comparison of energy storage technologies as energy buffer in renewable energy sources wtih respect to power capability," in *IEEE Young Researchers Symp. Elect. Power Eng.*, 2002.

[10] R. Folkson, Alternative Fuels and Advanced Vehicle Technologies for Improved Environmental Performance, Cambridge: Woodhead, 2014.

[11] D. Kok, Design Optimisation of a flywheel hybrid vehicle, PhD Dissertation, Eindhoven: Technical University Eindhoven, 1999.

[12] J. Hansen and D. O'Kain, "An Assessment of Flywheel High Power Energy Storage Technology for Hybrid Vehicles," Oak Ridge National Laboratory, Oak Ridge, TN, 2011.

[13] Hearn, C, M. Flynn, M. Lewis and R. Thompson, "Low cost flywheel energy storage for a fuel cell powered transit bus," in *IEEE Vehicular Power and Propulsion Conference*, Arlington, Texas, 2007.

[14] M. Ortuzar, J. Moreno and J. Dixon, "Ultracapacitor-based auxiliary energy storage system for an electric vehicle: implementation and evaluation," *Industrial Electronics, IEEE Transactions on,* vol. 54, no. 4, pp. 2147-2156, 2007.

[15] R. Shupbach and J. Balda, "Design methodology of a combined battery-ultracapacitor energy storage unit for vehicle power management," in *Power Electronics Specialist Conference*, Acapulco, 2003.

[16] T. Deppen and A. Alleyne, "Optimal Energy Use in a Light Weight Hydraulic Hybrid Passenger Vehicle," *J. Dyn. Sys., Meas., Control,* vol. 134, no. 4, 2012.

[17] D. Talancon, Computational System Performance Model of the INSTAR System, Berkeley: University of California, 2011.

[18] G. Genta, Kinetic energy storage: theory and practice of advanced flywheel systems, London: Butterworths, 1985.

[19] D. Lathrop, J. Fineberg and H. Swinney, "Transition to shear-driven turbulence in Couette-Taylor flow," *Physics Review A,* vol. 48, no. 10, pp. 6390-6405, 1992.

[20] M. Baer, "Aerodynamic heating of high-speed flywheels in low-density environments," DoE - Sandia Laboratories, Albaquerque, 1978.

[21] B. Murphy, D. Bresie and J. Beno, "Bearing loads in a vehicular flywheel battery," in *Electric and Hybrid Vehicle Design Studies, Proceedings of the 1997 International Congress and Exposition*, Detroit, 1997.

[22] A. McDonald, "Simplified Gyrodynamics of Road Vehicles with High-Energy Flywheels," in *1980 Flywheel Technology Symposium, US DoE*, 1980.

[23] J. Strubhar, R. Thompson, T. Pak, J. Zierer, J. Beno and R. Hayes, "Lightweight containment for high-energy rotating machines," *Magnetics, Transactions on,* vol. 39, no. 1, pp. 378-383, 2003.

[24] U.S. House of Representatives, "The Partnership for a New Generation of Vehicles (PNGV): Assessment of Program Goals, Activites, and Priorities, Hearings Before the Subcommittee on Energy and Environment of the Committee on Science," U.S. House of Representatives, Washington, DC, 1996.

[25] A. S-096-2004, *Space Systems - Flywheel Rotor Assemblies,* American Institute of Aeronautics and Astronautics, 2004.

[26] National Research Council, "Review of the Research Program of the Partnership for a New Generation of Vehicles: Fourth Report by the Standing Committee to Review the Research Programs of the Partnership for a New Generation of Vehicles," National Academy Press, Washington, D.C., 1998.

Appendix

Data files attached:

A Spreadsheet of Flywheel Sizes and Rotation Rates Considered

B Raw Data of Driving Profile Testing with Cumulative Energy Calculations

C Raw Data of Single Braking Events with Various PI Controller Tunings

D Driving Profile Accelerator and Braking Commands